University of Southampton
Faculty of Physical and Applied Sciences
School of Physics & Astronomy

Quantitative Analysis of Multi-Monochromatic Observations of Rapid Small Scale Aurora

Daniel Keith Whiter

Submitted for the degree of
Doctor of Philosophy

March 2011

UNIVERSITY OF SOUTHAMPTON

Abstract

Faculty of Physical and Applied Sciences
School of Physics & Astronomy

Doctor of Philosophy

Quantitative Analysis of Multi-Monochromatic Observations of Rapid Small Scale Aurora

by Daniel Keith Whiter

This thesis presents analyses of flickering aurora observed using the state-of-the-art Auroral Structure and Kinetics (ASK) multi-monochromatic ground-based auroral imager. Flickering aurora is observed as rapid (typically 2–20 Hz) oscillations in auroral luminosity. There are several competing theories for the generation mechanism of flickering aurora, although all use electromagnetic ion cyclotron (EMIC) waves. The work presented in this thesis has shown that precipitating electrons producing flickering aurora are accelerated by Landau damping of the EMIC wave, and that the wave parallel phase velocity is the primary factor limiting the electron precipitation energy. In addition, evidence is presented supporting the theory that very small structures in flickering aurora are caused by interference between multiple EMIC waves. A combined electron transport and ion chemistry model (the Southampton Ionospheric Model) has been used in this work to allow quantitative estimates of the energy of precipitating electrons responsible for aurora observed with ASK.

This thesis also presents a novel technique for intercalibrating optical and particle measurements of the aurora made by instruments onboard the Reimei satellite using the Southampton Ionospheric Model. This allows estimates of the flux of precipitating electrons at high energies above the detection limit of the Electron Spectrum Analyzer (ESA) particle detector. Optical images of the aurora obtained using the Multispectral Auroral Camera (MAC) instrument are also calibrated, allowing quantitative estimates of the auroral brightness without contamination from background light and auroral light reflected from the Earth. The technique has many possible applications in auroral studies using the Reimei satellite.

Contents

List of Figures

List of Tables

Declaration of Authorship

I, Daniel Keith Whiter, declare that this thesis entitled

Quantitative Analysis of Multi-Monochromatic Observations of Rapid Small Scale Aurora

and the work presented in this thesis are both my own, and have been generated by me as the result of my own original research. I confirm that:

- this work was done wholly while in candidature for a research degree at this University;
- no part of this thesis has previously been submitted for a degree or any other qualification;
- where I have consulted the published work of others, this is always clearly attributed;
- where I have quoted from the work of others, the source is always given. With the exception of such quotations, this thesis is entirely my own work;
- I have acknowledged all main sources of help;
- where the thesis is based on work done by myself jointly with others, I have made clear exactly what was done by others and what I have contributed myself;
- work presented in chapter 5 has been published in:
  Whiter, D. K., B. S. Lanchester, B. Gustavsson, N. Ivchenko, J. M. Sullivan, and H. Dahlgren, Small-scale structures in flickering aurora, Geophys. Res. Lett., 35, L23103, doi:10.1029/2008GL036134, 2008
- work presented in chapter 6 has been published in:
  Whiter, D. K., B. S. Lanchester, B. Gustavsson, N. Ivchenko, and H. Dahlgren, Using multispectral optical observations to identify the acceleration mechanism responsible for flickering aurora, J. Geophys. Res., 115, A12315, doi:10.1029/2010JA015805, 2010

D. K. Whiter, May 25, 2011

Acknowledgements

There are many people to whom I owe thanks. Most importantly I would like to thank Betty Lanchester, who has been immensely supportive throughout my university career. If I had not been lucky enough to have Betty as my undergraduate tutor I would not be in the enviable position I am today. She has always been ready to spend time discussing any problems or theories, and has given me so many wonderful opportunities.

Nickolay Ivchenko has taught me a lot about instrumentation, campaign, and the value of thinking very careful about how to go about observing. He showed me that an awful lot more can be accomplished in 5 minutes than I ever thought possible, provided things are done with thought and a good sense of humour. Nickolay also gave me the opportunity to spend several months in Stockholm, for which I am very grateful.

Björn Gustavsson is an incredible source of ideas of things to try, and is always ready to discuss crazy thoughts and theories. My only regret is that I haven't had time to try everything, though I am looking forward to lots of collaboration in the future. He also showed me that when it comes to trying something in science, the thing being "fun" is quite a necessity, you know.

I am very grateful to Takeshi Sakanoi for providing Reimei data, and for always responding to emails and questions with enthusiasm and support. I am also grateful to Harald Frey and the members of his ISSI team who let me join their meetings, which led to the work I have done with Reimei.

Hanna Dahlgren has been a great friend and support throughout my PhD, and has given me so many wonderful memories. She showed me how fantastic Sweden (and Scandinavia) is, and really made me feel partly Swedish. Spending time on campaign, at conferences, and in Stockholm has been by far the most fun bit of my PhD, in no small part thanks to Hanna.

I would like to thank all of my office mates over the past few years, who have

always made the office so pleasant, been ready to discuss anything, and have kept up my tea quota. Jo, Olli, Mina, Brendan, Sam and Björn also kept me sane on campaign and made it a most enjoyable time, despite the long hours and hard work.

Lizzie, thank you so much for all of your encouragement and belief in me, and for taking such an interest in what I do. Also thank you for putting up with me while I have been writing this thesis, and for poking me to get it finished! You have helped me in so many ways, and have made me feel so happy.

Finally I would like to thank my parents, for all their love and support, and for making me into a scientist at a very early age.

List of Abbreviations

A list of abbreviations used in this thesis is given below, together with their page of first use.

ACF autocorrelation function 56

ASK Auroral Structure and Kinetics 21

R_E Earth radii 31

EISCAT European Incoherent SCATter Scientific Association 39

EMIC electromagnetic ion cyclotron wave 31

EMCCD electron multiplying charge-coupled device 40

ESA Electron Spectrum Analyzer instrument onboard Reimei 53

ESR European Incoherent SCATter (EISCAT) Svalbard Radar 40

FAB field-aligned burst of electrons 35

FPGA field-programmable gate array 47

FFT fast Fourier transform 70

GPS Global Positioning System 47

HiTIES High-Throughput Imaging Echelle Spectrograph 40

IEDD inhomogeneous energy density driven wave 134

IGRF-10 10th generation International Geomagnetic Reference Field, terrestrial magnetic field model 32

IMF interplanetary magnetic field 23

ISA Ion Spectrum Analyzer instrument onboard Reimei 53

ISR incoherent scatter radar 55

ISSI International Space Sciences Institute, Bern, Switzerland 111

KTH Royal Institute of Technology, Stockholm, Sweden 39

LTO-2 Linear Tape-Open generation 2 magnetic tape 46

MAC Multi-spectral Auroral Camera instrument onboard Reimei 53

MLT magnetic local time 70

MSISE-90 Mass Spectrometer Incoherent Scatter thermospheric model, 1990 (*Hedin*, 1991) 28

NI National Instruments 47

PCB printed circuit board 47

PNG Portable Network Graphics 48

PPS pulse per second 47

PRNU photo response non-uniformity 51

PSD power spectral density 70

RAID Redundant Array of Independent Disks 45

SAO Smithsonian Astrophysical Observatory 53

SIF Spectrographic Imaging Facility 39

UHF ultra high frequency 54

UT universal time 70

VHF very high frequency 54

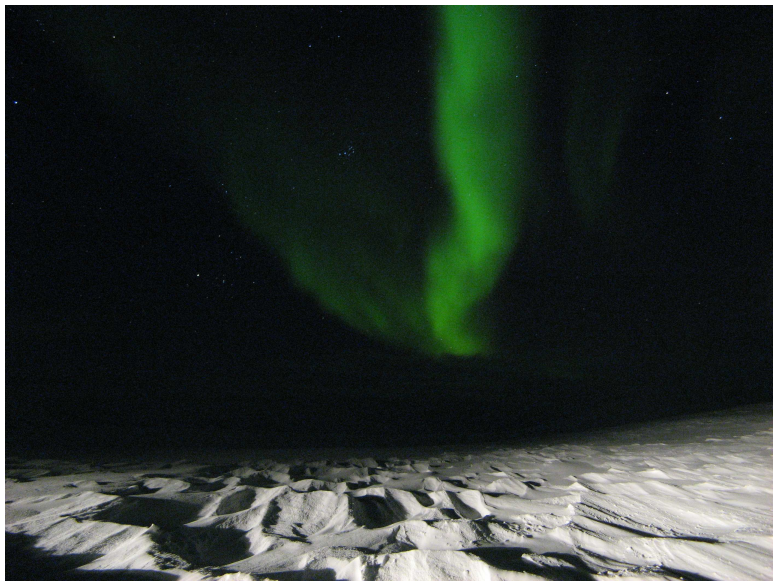

The possession of knowledge does not kill the sense of wonder and mystery. There is always more mystery.

Anaïs Nin

Chapter 1

Introduction

The subject of this thesis is the aurora, or "northern lights". This phenomenon is both stunningly beautiful and scientifically interesting, and has enthralled many people over many years in many different ways. It is a sight which is often regarded with great respect, sometimes in an almost spiritual way.

The aurora allows direct observation of complex processes occurring in a natural plasma, making it very valuable to science. The work presented here mainly concerns flickering aurora, which is seen as rapid oscillations in auroral luminosity.

Data from a variety of instruments have been used in this thesis. The Auroral Structure and Kinetics (ASK) instrument is a multi-monochromatic ground-based optical imager, and has provided data for the majority of the work presented here. The Japanese Reimei satellite, carrying both optical imagers and particle detectors, has also provided a significant amount of data for this work. The analysis of observational data has been heavily supported by the Southampton Ionospheric Model.

Chapter 2 gives a brief overview of the theoretical background and concepts relevant to this thesis, together with a summary of current theory regarding flickering aurora. Chapter 3 describes the instrumentation used to provide data used in this work. The author has been heavily involved in the technical development of the ASK instrument, which is described in more detail than the other instruments. Chapter 4 describes the Southampton Ionospheric Model which is used for work presented in chapters 6 and 7. Two studies into flickering aurora are presented in chapters 5 and 6: Chapter 5 presents a study into the spatial properties of flickering aurora and chapter 6 presents a study using images recorded in different emissions to estimate the energy of precipitating electrons responsible for

flickering aurora. The results of these studies can be explained by only one of the current theories for the generation of flickering aurora. A full discussion is provided in the two flickering aurora chapters. Chapter 7 presents an alternative use for the Southampton Ionospheric Model as part of a technique to intercalibrate optical and particle measurements of the aurora made by the Reimei satellite. In this Reimei study the model is used to simulate actual auroral events. Chapter 8 concludes the thesis and suggests several ideas for future work continuing the studies presented in chapters 5, 6 and 7.

Chapter 2

Theoretical Background

This chapter gives a brief overview of topics relevant to the work presented in this thesis. The sources used for general background information presented here are: *Kivelson and Russell* (1995); *Paschmann et al.* (2003); *Stasiewicz et al.* (2000).

2.1 Particle transport from the Sun to the Earth

The source of the aurora lies with the Sun. A continuous stream of charged particles flows out from the Sun, and is transported to the Earth through interplanetary space as part of the solar wind. The charged particles are "frozen in" with the interplanetary magnetic field (IMF). The magnetic field lines extending out from the Sun become wound up into a spiral due to solar rotation. The IMF cone angle (angle between the IMF and the Sun-Earth line) changes from radial close to the Sun to almost toroidal far from the Sun at the edge of the heliosphere. At the orbit of the Earth the IMF has a cone angle of about 45°, although this is variable, for example due to changes in solar wind speed.

The Earth's magnetic field punches a hole in the heliosphere, forming the Earth's magnetosphere, within which the motion of particles is predominantly controlled by the Earth's magnetic field. Plasma particles contained within the IMF are transferred into the Earth's magnetosphere by magnetic reconnection, which occurs primarily on the nose of the magnetosphere and in the geomagnetic tail. Reconnection is most efficient when the reconnecting field lines are antiparallel. The rate of reconnection varies depending on the strength and direction of the IMF. Under steady state reconnection (in which the rate of reconnection is equal in the nose and tail of the magnetosphere) geomagnetic field lines are

broken on the nose of the magnetosphere forming "open" field lines connected from the polar cap out into the IMF (and ultimately to the sun). These open field lines are dragged across the poles by the solar wind and stretched out into the geomagnetic tail. In the tail open field lines connected to the northern and southern hemisphere reconnect to form a closed geomagnetic field line and an interplanetary field line. The new geomagnetic field line relaxes towards the Earth, while the interplanetary field line moves away from the Earth and forms part of the solar wind. The closed geomagnetic field line flows around the Earth to the nose of the magnetosphere and the process is repeated. This process is known as "convection", and is illustrated in figure 2.1. Individual field lines are marked with numbers, showing the progression of a field line through the convection process. The footprints of the field lines in and around the polar cap are also marked with the same numbers in the lower part of the diagram.

During a magnetic substorm the reconnection rate is temporarily increased on the nose of the magnetosphere, usually due to a strong southward IMF, allowing more particles and energy into the magnetosphere. The build up of plasma in the magnetospheric tail lobes causes a new reconnection point to form, closer to the Earth than the existing reconnection point. This creates a bubble of plasma in the tail between the old and the new reconnection regions. The bubble exits the tail and is carried away with the solar wind. Plasma particles are accelerated at the new reconnection point and injected into the inner magnetosphere, leading to dramatic auroral displays. Eventually the new tail reconnection point moves further down the tail away from Earth.

Particles inside the magnetosphere gyrate around the Earth's magnetic field lines due to the Lorentz force. If they have a velocity component parallel to the magnetic field their motion traces a spiral around a field line. Particles spiralling around the Earth's magnetic field lines move towards stronger magnetic field as they approach the poles. The convergence of the field lines introduces a radial component to the magnetic field experienced by a gyrating particle, which causes a force parallel to the field line at the centre of the particle's gyration and towards the diverging magnetic field lines (weaker field). This acts like a mirror, reflecting gyrating particles away from the poles. Since such a magnetic mirror is present at both ends of the field line (in both the northern and southern hemisphere), particles become trapped in a "magnetic bottle". The distance from the equatorial plane at which a particle is reflected is determined by the particle's pitch angle (angle between particle velocity and magnetic field line) at

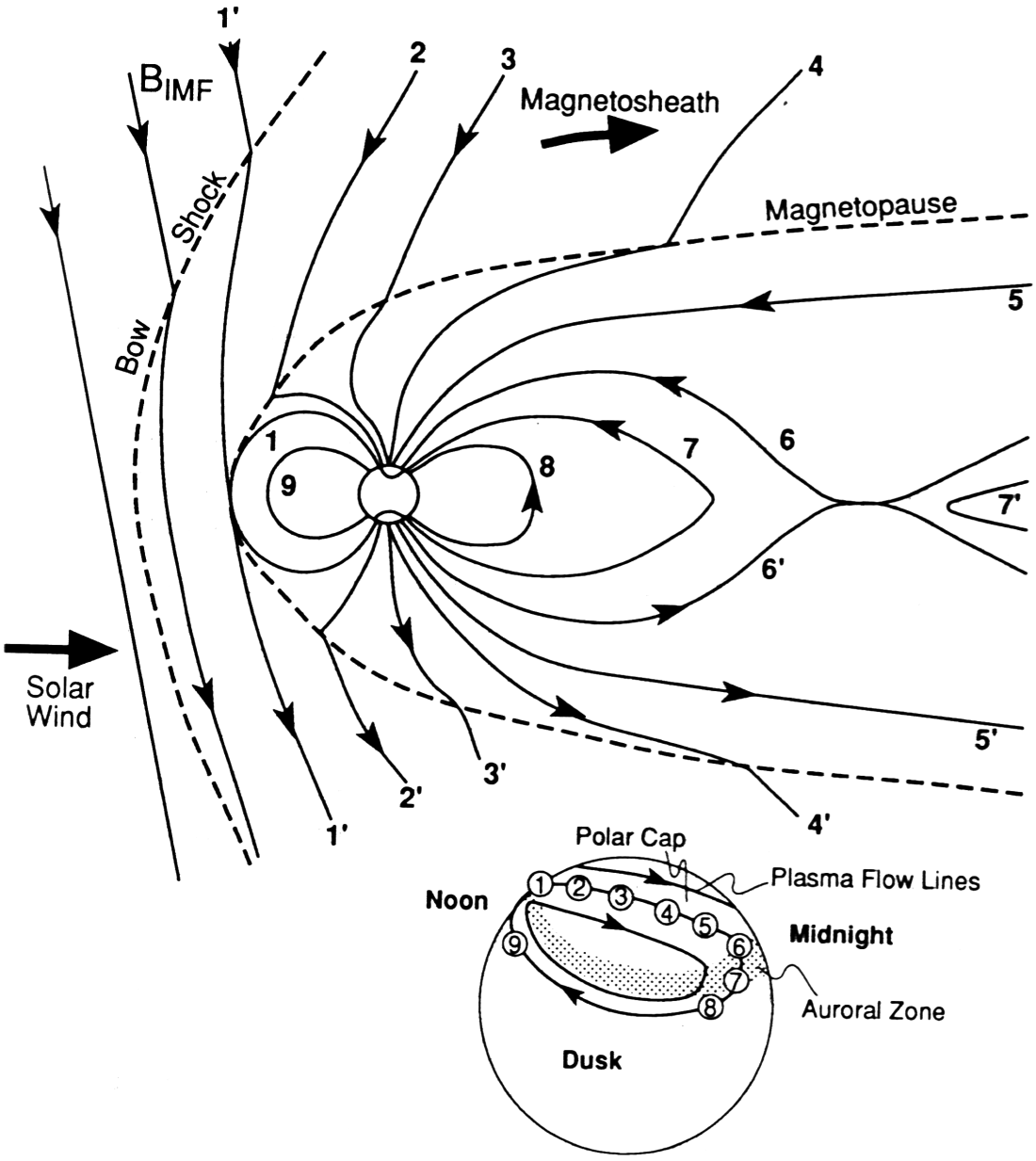

Figure 2.1: Convection within the Earth's magnetosphere under steady state reconnection. An individual field line progresses from position 1–9. Taken from *Kivelson and Russell* (1995).

the equator. A particle with a pitch angle of 90° will not travel along the field line and will gyrate in the equatorial plane. Smaller pitch angles lead to higher (in latitude) mirror points. Particles which have a small enough pitch angle are able to escape from the magnetic bottle, precipitating down into the Earth's ionosphere. The cone in velocity vectors within which particles escape and are lost from the bottle is called the loss-cone. Particles with high pitch angles which remain trapped form the Earth's radiation belts.

The source or sources of energy for particles precipitating into the ionosphere are not yet well understood. In the solar wind electrons have low energies, typically less than 1 eV. However, primary precipitating electrons responsible for the aurora in the ionosphere have much larger energies, on the order of 10^2–10^4 eV. The understanding of how these particles are accelerated to such high energies is one of the main goals of auroral research at present.

The term "inverted-V" is widely used to describe many space-based observations of precipitating electrons with a distinctive signature, in which higher energy electrons are seen in the centre of an auroral arc and lower energy electrons are seen on either edge. An example of an inverted-V signature is shown in figure 2.2, taken from (*McFadden et al.*, 1990). These observations were made using a particle detector onboard a sounding rocket. See (*McFadden et al.*, 1990) for a full description of the instrumentation and observations.

2.2 Auroral ionosphere

The ionosphere is a region of the Earth's atmosphere which is ionised to form a plasma, primarily by solar radiation. It overlaps with the thermosphere and exosphere, and to a lesser extent the mesosphere. The bottom of the ionosphere is the point where the atmospheric concentration becomes sufficiently large that the lifetime of a free electron is too short compared to the rate of ionisation to allow a plasma to form. This is typically at about 70–80 km altitude. The top of the ionosphere merges with the inner edge of the magnetosphere at altitudes of a few thousand km. Electric currents are able to flow in the ionosphere, forming an important part of the planet's current system.

The ionosphere is made up of numerous neutral and ion species. Although the ionosphere is a plasma, the neutral concentration is much larger than the ion and electron concentrations at all but the very highest altitudes. Figure 2.3

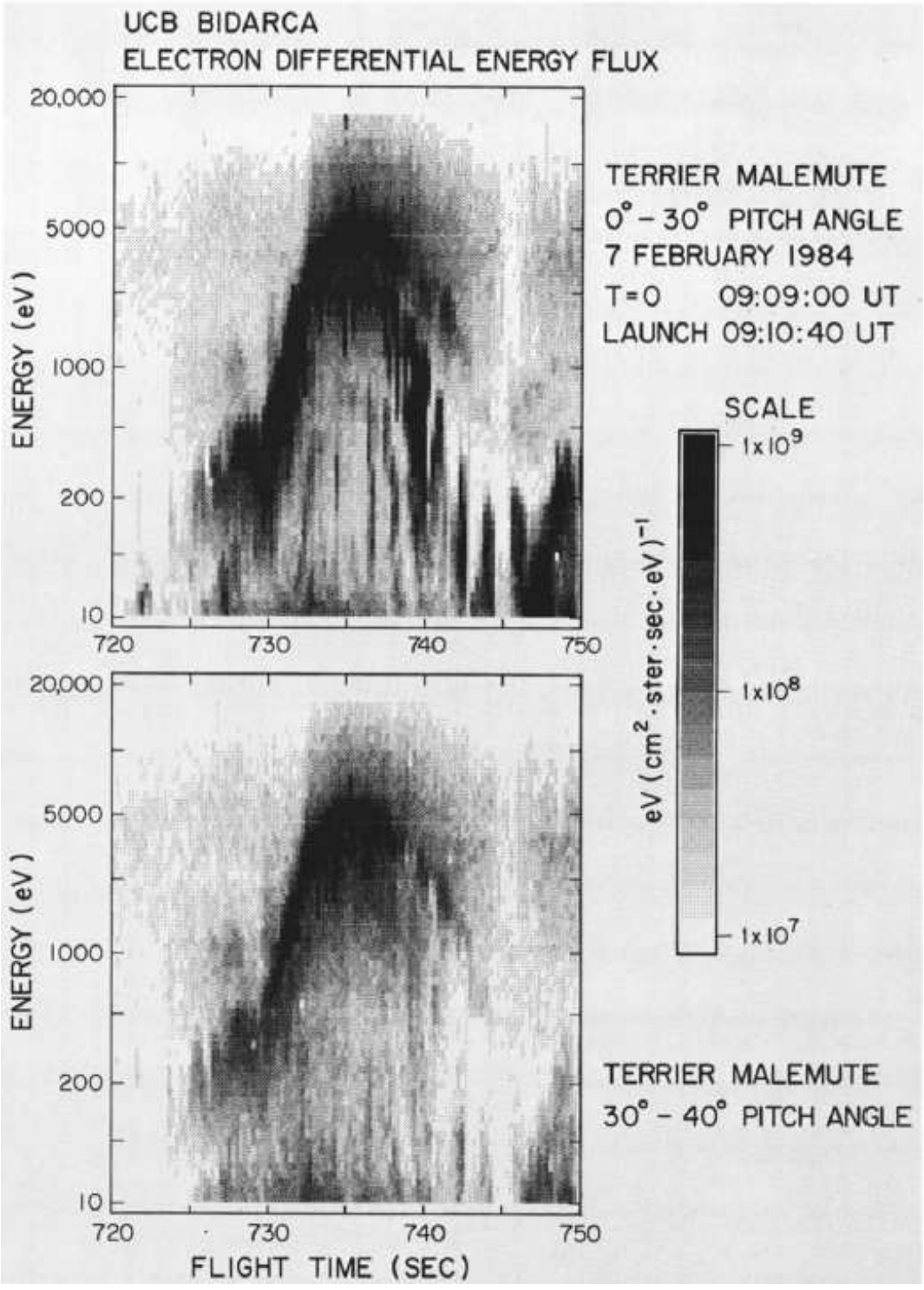

Figure 2.2: Rocket observations of precipitating electrons displaying an inverted-V signature, taken from (*McFadden et al.*, 1990).

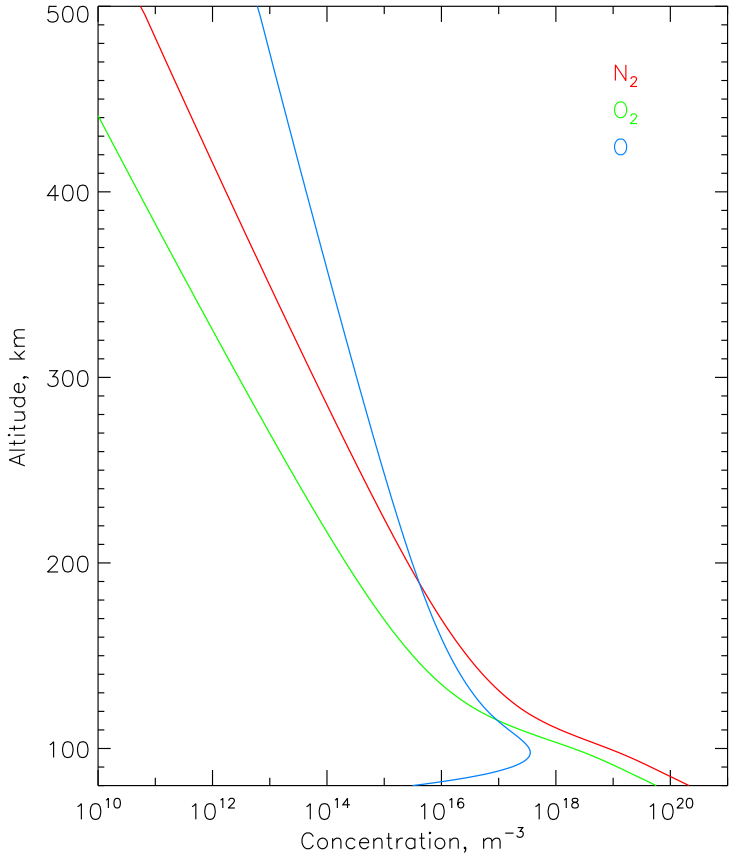

Figure 2.3: Altitude profiles of the concentration of the three major neutral species in the ionosphere, as modelled by MSISE-90 for ∼18 UT on 22 October 2006.

shows the concentration of the three major neutral species (N_2, O_2 and O) above Tromsø, Norway as a function of altitude, as predicted by the Mass Spectrometer Incoherent Scatter 1990 (MSISE-90) model. The concentration of the two molecular species decreases monotonically to higher altitudes. The concentration of atomic oxygen peaks in the E-region at about 100 km. Atomic oxygen is mainly produced by dissociation of O_2. At low altitudes (below about 200 km) the molecular species dominate, whereas at higher altitudes the concentration of atomic oxygen is larger than the concentrations of N_2 and O_2.

Energetic charged particles (mostly electrons but also protons and heavier ions) precipitating into the polar ionosphere from the magnetosphere cause ionisation and excitation of neutral species. When the excited ions and neutrals relax they emit photons, which are observed as the aurora. The relative intensities of different auroral emissions depend primarily on the relative concentrations of the major species and on the emission cross-sections. The majority of auroral

Figure 2.4: A photograph of the aurora over Tromsø, Norway, taken by the author on 18 October 2006.

emissions come from N_2, O_2, O, N_2^+, O_2^+, and O^+. Molecular emissions have a rich band structure due to vibrational and rotational energy levels, while atomic emissions are observed as single lines or multiplets. The auroral emissions used in this thesis are discussed in chapters 3 and 4. A photograph of the aurora over Tromsø, Norway, is shown in figure 2.4. The emission giving rise to the aurora's distinctive green colour, as seen in the photograph, comes from the $^1S_0$ – $^1D_2$ transition in atomic oxygen. Rays can be seen in the arcs in the centre of the image as vertical striations tracing out the magnetic field lines, although the exposure time of the photograph was 15 s, blurring and hiding rapidly moving structure.

The aurora is highly structured on many different length scales, from 100s of kilometres down to the electron gyroradius of 10s of metres (e.g. *Partamies et al.*, 2010, and references therein). This structuring is evidence of different processes both in the ionosphere and magnetosphere. Work presented in this thesis involves the study of aurora on very small scales from 10s to 100s of metres. At this scale the aurora can be very dynamic with many complicated and rapid structures. Very little is known about the generation mechanisms of such struc-

tures. Although Alfvén waves (briefly described in section 2.3) are thought to be responsible for many small-scale features (*Chaston et al.*, 2003, and references therein), the methods by which different structures form are unclear. Recent technological improvements in instrumentation have led to the discovery of new types of small-scale structures in the aurora (e.g. *Dahlgren et al.*, 2010), as well as vastly improved observations to help constrain theories regarding previously observed features (*Sandahl et al.*, 2008).

2.3 Alfvén waves and electromagnetic ion cyclotron (EMIC) waves

An Alfvén wave is a low-frequency electromagnetic plasma wave in which the ions oscillate perpendicular to the direction of wave propagation and the magnetic field line tension provides the restoring force. Dispersionless Alfvén waves travel at the Alfvén velocity, V_A, given by

$$V_A = \frac{B}{\sqrt{\mu_0 \rho_i}} \tag{2.1}$$

where B is the magnetic field strength, μ_0 is the magnetic permeability of free space, and ρ_i is the mass density of all ion species (including electrons), with an angular frequency given by

$$\omega = kV_A \tag{2.2}$$

where k is the wave number.

Dispersive Alfvén waves are produced due to kinetic effects related to the finite ion gyroradius, electron skin depth, and electron thermal speed (see e.g. *Stasiewicz et al.*, 2000, and references therein). They are important in the case of the aurora because dispersive Alfvén waves have an electric field component parallel to the magnetic field, which can accelerate electrons into the ionosphere either directly or by Landau damping. Alfvén waves are thought to be responsible for a significant fraction of aurora (*Chaston et al.*, 2007), particularly small-scale aurora. There are two different forms of dispersive Alfvén waves: inertial Alfvén waves and kinetic Alfvén waves (*Stasiewicz et al.*, 2000). Inertial Alfvén waves exist when the Alfvén velocity is larger than the electron thermal velocity, and the cold electrons oscillate in response to the wave parallel electric field. The

electron inertia slows the field-aligned group velocity of the inertial Alfvén wave. Kinetic Alfvén waves exist when the electron temperature is high, and so the electron thermal velocity is larger than the Alfvén velocity. In the ionosphere and magnetosphere inertial Alfvén waves dominate up to altitudes of about 3–4 Earth radii (R_E), which covers the auroral acceleration region.

The dispersion relation for inertial Alfvén waves is

$$k_{\parallel}^2 V_A^2 = \omega^2 (1 + k_{\perp}^2 \lambda_e^2) \tag{2.3}$$

where $k_{\parallel}$ and $k_{\perp}$ are the parallel and perpendicular wave numbers, ω is the wave angular frequency, and λ_e is the electron collisionless skin depth.

Many theories for the generation of flickering aurora (described in section 2.4), which is one of the main topics of this thesis, use electromagnetic ion cyclotron (EMIC) waves. EMIC waves are inertial Alfvén waves with a correction for finite frequency effects, with a dispersion relation given by

$$k_{\parallel}^2 V_A^2 = \frac{\omega^2 (1 + k_{\perp}^2 \lambda_e^2)}{1 - \frac{\omega^2}{\omega_{ci}^2}} \tag{2.4}$$

where ω_{ci} is the ion cyclotron frequency. This restricts the waves to frequencies below the ion cyclotron frequency.

2.3.1 Calculating the EMIC wave parallel phase velocity

The calculation of the parallel phase velocity of EMIC waves is important for the evaluation of theories for the generation of flickering aurora. This section describes how the EMIC parallel phase velocity can be calculated using observed and modelled properties of the flickering aurora and ionosphere.

The EMIC wave dispersion relation, given in equation 2.4, forms the basis of this calculation. The Alfvén velocity and electron collisionless skin depth are properties of the ionospheric plasma and can be calculated using estimated values for the magnetic field strength and ion composition (densities, masses, and charges) only. The ion cyclotron frequency of a particular ion can also be calculated using the magnetic field strength and ion composition.

The electron collisionless skin depth is given by

$$\lambda_e = \frac{c}{\omega_p} \tag{2.5}$$

where c is the speed of light and ω_p is the plasma frequency, which is given by

$$\omega_p = \sqrt{\frac{n_e e^2}{m_e \epsilon_0}} \tag{2.6}$$

where n_e is the electron number density, e is the electron charge, m_e is the electron rest mass, and ϵ_0 is the electric permittivity of free space. Assuming quasi-neutrality the electron number density can be calculated from the ion composition of the plasma.

For a particular ion with charge q_i and mass m_i the ion cyclotron frequency is given by

$$\omega_{ci} = \frac{q_i B}{m_i} \ . \tag{2.7}$$

Using equations 2.4–2.7 and equation 2.1, together with estimated values of the magnetic field strength and plasma ion composition, it is therefore possible to calculate $k_\parallel$ for given values of ω and $k_\perp$. The parallel phase velocity of the wave is then given by

$$v_\parallel = \frac{\omega}{k_\parallel} \ . \tag{2.8}$$

In the case of flickering aurora ω can be measured directly, and the horizontal diameter of flickering patches can be used to estimate $k_\perp$. Assuming the diameter of a flickering patch corresponds to half a perpendicular wavelength,

$$k_\perp = \frac{\pi}{d} \tag{2.9}$$

where d is the flickering patch diameter. This gives $k_\perp$ at the altitude of the flickering aurora. However, using a magnetic field model it is possible to trace the observed patch size up the field line to the acceleration region. For work presented in this thesis the 10th generation International Geomagnetic Reference Field (IGRF-10) magnetic field model is used. A computer program is used to trace the flickering patch up the model field line from auroral altitudes. The IGRF-10 model is also used to compute the magnetic field strength, B, when applying the method described in this section. Figure 2.5 shows the modelled magnetic field strength for the field-line in the magnetic zenith as viewed by the ASK instrument.

The ion composition necessary for the calculations performed in this work was identical to the low-density case used by *Sakanoi et al.* (2005). The number

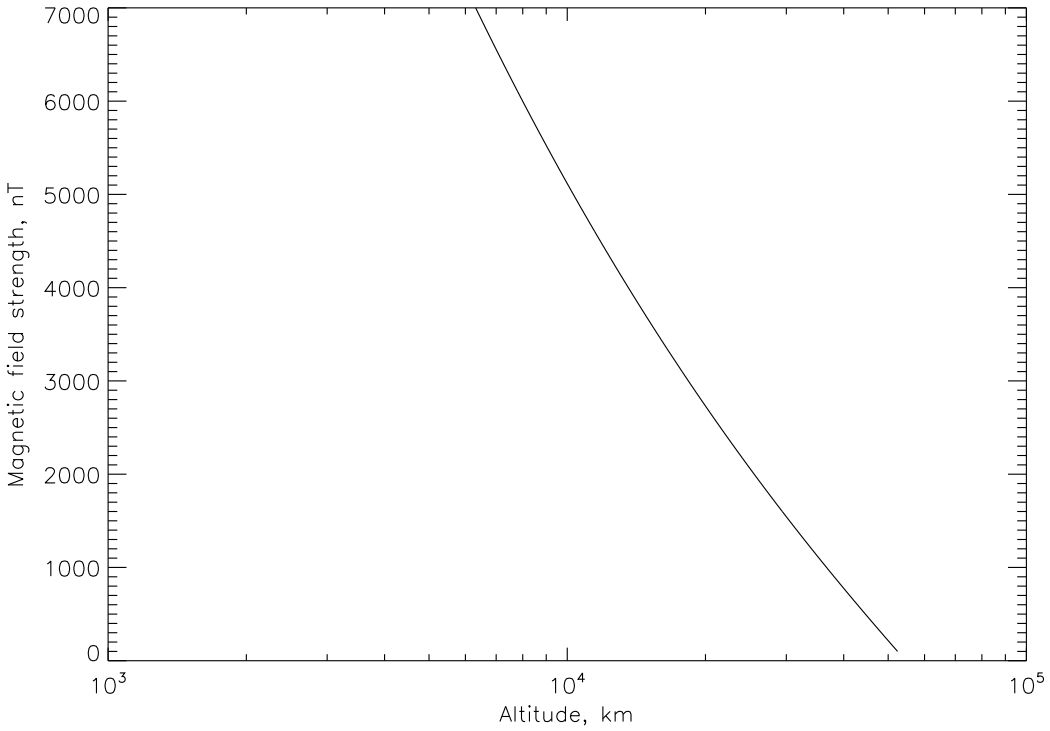

Figure 2.5: Magnetic field strength used in the calculation of EMIC wave parallel phase velocity.

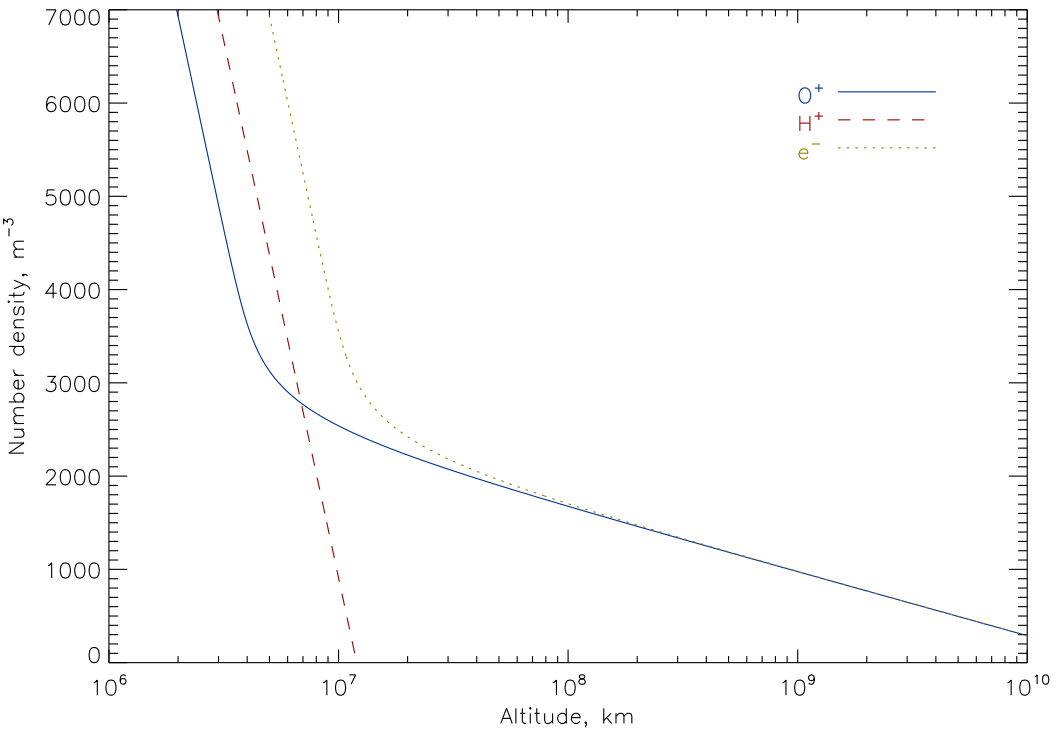

Figure 2.6: Oxygen ion (blue solid line), hydrogen ion (red dashed line) and electron (yellow dotted line) number densities used in the calculation of EMIC wave parallel phase velocity.

densities of hydrogen (n_{H}) and oxygen (n_{O}) ions are given by

$$n_{\mathrm{H}} = 1 \times 10^7 / \exp\left(\frac{z}{5000}\right) \tag{2.10}$$

and

$$n_{\mathrm{O}} = 2.64 \times 10^1 0 / \exp\left(\frac{50.42 \times z}{15000}\right) + \frac{n_{\mathrm{H}}}{1.5} \tag{2.11}$$

where z is altitude in km and n_{H} and n_{O} are in m^{-3}. The electron number density is calculated by summing over the two ion number densities. Figure 2.6 shows these number densities at altitudes from 100 km to 7000 km (slightly over 1 R_E). Note that these number densities are small compared to typical conditions, but are not unrealistic.

2.4 Flickering aurora

Flickering aurora is observed as rapid (typically 2–20 Hz) temporal fluctuations in auroral luminosity, usually in small spots or patches (less than a few 10s of km across) within a region containing discrete aurora. It is most typically observed in auroral breakup events. *Kunitake and Oguti* (1984) described flickering aurora as laterally vibrating columns, which are seen as flickering spots when viewed from below. These spots are often seen in groups, or "clusters". The typical frequencies of flickering aurora are similar to the oxygen ion cyclotron frequency at approximately 1 R_E (*Temerin et al.*, 1986; *Lund et al.*, 1995). Flickering aurora has also been observed at higher frequencies up to 180 Hz (*McHarg et al.*, 1998), which corresponds to the hydrogen ion cyclotron frequency in the same altitude range. The flickering modulation amplitude has often been reported as ∼10–20 percent of the total aurora luminosity (e.g. *Kunitake and Oguti*, 1984; *Sakanoi and Fukunishi*, 2004; *Gustavsson et al.*, 2008). It is known that flickering patches exhibit complex spatial patterns and motions on various length scales (*Kunitake and Oguti*, 1984; *Sakanoi and Fukunishi*, 2004; *Gustavsson et al.*, 2008). *Sakanoi et al.* (2005) showed that drifting and non-drifting flickering spots can be explained by interference between two EMIC waves. *Gustavsson et al.* (2008) expanded on this work and showed that interference between three or more waves can explain rotating and swirling flickering structures.

Particle detectors flown on rockets have detected field-aligned bursts of electrons (FABs) which show modulations at similar frequencies to flickering aurora (*Evans*, 1967; *Arnoldy*, 1970; *Spiger and Anderson*, 1985; *McFadden et al.*, 1987). For many years it has been suspected that FABs are responsible for flickering aurora. This connection was confirmed by *Lund et al.* (1995) using a combination of rocket-based particle and field measurements and ground-based auroral imaging. FABs are usually seen coincident with typical inverted-V precipitation, and often show dispersion over a wide energy range below the inverted-V peak energy. Few observations have been reported of FABs at exclusively high energies above or close to the inverted-V peak energy, although *McFadden et al.* (1987) discuss instrumental factors and trends which may introduce a selection effect favouring observations of lower energy flux oscillations. However, *Spiger and Anderson* (1985) reported rocket-based observations which show large oscillations in only the highest energy channel of their electron detector (10–20 keV). *McFadden et al.* (1987) also report some observations of oscillating field-aligned electron

fluxes which were restricted to a narrow energy range at the energy flux peak (inverted-V peak energy). Note that in this thesis "FABs" refers to field-aligned bursts associated with the upward ion beam inside an inverted-V potential drop, and not other classes of FABs such as those associated with shear instabilities or the plasma sheet boundary layer.

Most current theories for the origin of FABs and flickering aurora are based on electron acceleration, or the modulation of previously accelerated electrons, by EMIC waves. These waves are known to exist with frequencies similar to the local O^+ ion cyclotron frequency at altitudes of a few thousand km (*Erlandson and Zanetti*, 1998; *Lund et al.*, 1995). However, the theoretical interpretation of how EMIC waves produce the observed characteristics of flickering aurora is not yet well understood. *McFadden et al.* (1998) used instruments onboard the FAST satellite to observe wave-particle interactions between H^+ EMIC waves (at ∼120 Hz) and downgoing field-aligned electron fluxes in inverted-V arcs at altitudes of approximately 3700 km. Similar direct observations of wave-particle interactions involving O^+ EMIC waves have not yet been reported, although many O^+ EMIC waves have been observed using satellite-based instruments (e.g. *Erlandson and Zanetti*, 1998).

Temerin et al. (1986) suggested a comprehensive model in which EMIC waves allow cool ionospheric electrons to move up the field line, before accelerating them back to the ionosphere at higher energies. In their model the wave parallel electric field is a significant factor limiting electron acceleration. They showed with test particle simulations that this model can accelerate electrons to keV energies, and reproduces many of the observed characteristics of FABs. However, *McFadden et al.* (1987) and *Chen et al.* (2005) argue that the model requires wave fields with unrealistically large amplitudes in order to reach energies of a few keV. In addition, the Temerin model produces a wide spread of energies. This fits well with many observations of FABs, though not all reported observations.

McFadden et al. (1987) developed the *Temerin et al.* (1986) model by introducing a relationship between FABs and the energy flux peak. They suggested that cold electrons are trapped above and within the turbulent acceleration region associated with a parallel potential drop. As an EMIC wave travels down through the potential drop region, cold electrons are perturbed and released in phase with the wave. These electrons are subsequently accelerated by the potential drop, producing the flickering aurora. Their resulting energy will depend on the fraction of the potential drop through which they have fallen, and this model

therefore produces a range of energies with a maximum at the energy flux peak.

Arnoldy et al. (1999) proposed an alternative generation mechanism in which an on-off inverted-V potential oscillates at ion cyclotron frequencies. This model is similar to the model proposed by *McFadden et al.* (1987) in that the maximum energy attainable by precipitating FAB electrons is constrained by the maximum voltage of the inverted-V potential. The model was developed to explain simultaneous observations of energy-dispersed FABs and pitch-angle dispersed electrons at the inverted-V energy.

Chen et al. (2005) used detailed modelling to show that resonant acceleration and deceleration (Landau damping) by dispersive Alfvén waves (e.g. EMIC waves) in combination with inverted-V acceleration can produce the observed dispersion signatures seen within FABs. In their model the dominant factor limiting acceleration is the wave parallel phase velocity, whereas the amplitude of the electric field has much less effect than in the *Temerin et al.* (1986) model. They consider the interaction between the wave and electrons reflected or backscattered by the potential drop, which allows the *Chen et al.* (2005) model to accelerate electrons to high energies (10s of keV) with realistic electric field amplitudes. Their results show that while in most cases the dispersed features extend from the inverted-V peak down to lower energies, acceleration to energies above the inverted-V peak is possible if the Alfvén wave is generated at altitudes above the inverted-V potential drop. In this case electrons are first accelerated by the wave before receiving further acceleration as they fall through the potential drop.

Sakanoi et al. (2005) also explained flickering aurora using the Landau damping interaction between dispersive Alfvén waves and precipitating electrons. They considered the spatial interference patterns that would be produced by two interfering dispersive Alfvén waves, and found that their observations of spatial patterns in flickering aurora were similar to the theoretical interference patterns. *Gustavsson et al.* (2008) expanded this work to consider more than two interfering waves, in order to explain rotating and swirling patterns observed in flickering aurora.

A summary of the four theories explained in this section is given in table 2.1. These theories will be further discussed in light of the results presented in chapters 5 and 6.

Proposed by	Acceleration limited by
Temerin et al. (1986)	EMIC wave parallel electric field
McFadden et al. (1987)	Parallel potential drop peak energy
Arnoldy et al. (1999)	Parallel potential drop peak energy
Chen et al. (2005)/ *Sakanoi et al.* (2005)	EMIC wave parallel phase velocity

Table 2.1: Summary of theories for the generation mechanism of flickering aurora.

Chapter 3

Instrumentation

The author has been heavily involved in deploying, maintaining, and running the ASK instrument used in this thesis. Numerous software and hardware updates have been made by the author, together with colleagues in Southampton and at the Royal Institute of Technology (KTH), Stockholm. Several computer programs for the operation of the instrument were written by the author. The author has also performed similar roles in relation to other instruments not used in this thesis, such as the Spectrographic Imaging Facility (SIF), and has also been responsible for running the European Incoherent SCATter (EISCAT) radars during camapaigns both on Svalbard and in Tromsø, Norway. The author has participated in approximately 10 observing and maintainance campaigns during the course of his PhD.

3.1 Auroral Structure and Kinetics (ASK)

ASK is a ground-based optical auroral imager. One of the greatest strengths of the ASK instrument is its ability to image the aurora simultaneously in multiple narrow wavelength bands. As images are made in different emissions at exactly the same time they can be directly compared. Different auroral emissions are produced at different altitudes in the ionosphere and are therefore sensitive to different energies of precipitating electrons (higher energy electrons penetrate further down into the ionosphere). Through careful selection of spectral filters it is possible to estimate the energy and flux of precipitating electrons producing the aurora (e.g. *Kaila*, 1989; *Lanchester et al.*, 2009, and references therein). Estimating electron spectra using ground-based optical imagers in this way has

several advantages over other methods, such as using particle detectors on satellites or rockets. As an image of a region of aurora is obtained it is possible to resolve the space-time ambiguity which cannot be done when making single-point observations with a space-based particle detector or ground-based radar. Also, it is possible to observe an auroral event as it evolves over time, whereas a satellite passing overhead can only observe the same event for the short duration it takes to fly over.

3.1.1 Instrument overview

The ASK instrument consists of three highly sensitive Andor iXon electron multiplying charge-coupled device (EMCCD) cameras and two photometers, co-aligned on magnetic zenith. The cameras and photometers are equipped with narrow passband interference filters centred on different auroral emissions, described in detail in section 3.1.3. The cameras each have an identical narrow field of view of 3.1° × 3.1°, corresponding to roughly 5 km × 5 km at 100 km height. The photometer data used in this thesis were acquired with a field of view of 10 arcmins, although the photometer field of view is adjustable. Each EMCCD detector contains 512 × 512 pixels, which are usually binned into 256 × 256 equal-sized "super-pixels" during acquisition, primarily to allow an increased image rate. This provides a spatial resolution of approximately 20 m at 100 km height, allowing for detailed studies of auroral features on the sub-km scale. Typically the cameras are operated at 32 Hz during observations coordinated with radar runs (see section 3.3 for a description of radar observations) and at 20 Hz at all other times. ASK is jointly owned and operated by the University of Southampton and KTH, Stockholm. First results from the instrument were presented by *Dahlgren et al.* (2008).

ASK has been operational since December 2005, when it was installed at the EISCAT Svalbard Radar (ESR) in the high arctic (geographic latitude 78.15° N, longitude 16.03° E), where ASK can observe mostly dayside aurora. For the 2006/07 observing season the instrument was moved to the mainland EISCAT site in Ramfjordmoen, close to Tromsø, Norway (geographic latitude 69.58° N, longitude 19.22° E), where ASK can observe mostly nightside aurora. A photograph taken by the author of ASK deployed in Ramfjordmoen is shown in figure 3.1. In September 2007 ASK was returned to the ESR, where it has remained since. The co-location of ASK and the Southampton-owned High-Throughput

Figure 3.1: A photograph of the ASK instrument in Ramfjordmoen taken by the author on 22 October 2006. The flickering auroral event studied in chapters 5 and 6 occurred approximately 2 hours after this photograph was taken.

Imaging Echelle Spectrograph (HiTIES) instrument is a significant advantage of stationing ASK at the ESR. All ASK data analysed for this thesis were obtained in 2006 while the instrument was situated close to Tromsø.

The ASK instrument is self-contained and has always been situated outdoors, with power and computer network connections provided by the host site. A diagram of the ASK instrument is shown in figure 3.2. There are two main parts to the structure: "the bucket" and "the computer box". The bucket sits on top of the computer box, and consists of the optical bench (upon which the cameras and optics are mounted) surrounded by two "shroud" covers containing glass windows for the cameras and photometers. It is held by a frame which allows the azimuth and elevation to be adjusted. The bucket shroud covers contain access hatches for maintenance which are not shown in figure 3.2, but can be seen as a large black circle in the photograph in figure 3.1.

A diagram showing one half of the inside of the bucket is shown in figure 3.3. The two photometers (highlighted in red) are mounted on the optical bench on either side of one of the cameras (ASK3, highlighted in yellow). The other two cameras (ASK1 and ASK2) are mounted on the other side of the optical bench (not shown in diagram). An $f/1$, f=75mm Kowa lens is attached to each camera, providing a field of view of $6.2° \times 6.2°$, and the filters fit closely on top of these lenses. The ASK3 filter and lens are together highlighted in green in the diagram. Since September 2006 Galilean-type converters (highlighted in blue) with 2x angular magnification have been mounted on the optical bench in front of the lenses, reducing the field of view of the cameras to $3.1° \times 3.1°$.

The computer box houses three computers (one for each ASK camera) along with other electronic equipment such as a computer network switch. There is a small hole for cables in one corner of the base of the computer box. There are two ducts connecting the bucket and the computer box; one for carrying cables and the other for transferring heat produced by the computers to the bucket.

Heat is needed in the bucket for melting snow and ice which would otherwise build up on the windows, and for maintaining a stable ambient operating temperature. A radiator is also attached to the outside of the computer box to remove heat and ensure the computers do not get too hot. The temperature inside the computer box is typically between 10°C and 20°C, compared to a typical outside temperature of between -20°C and -10°C. The bucket also contains two thermal heaters to ensure it is warm enough to prevent snow and ice accumulating on the glass windows. Originally these heaters were controlled by a thermostat set

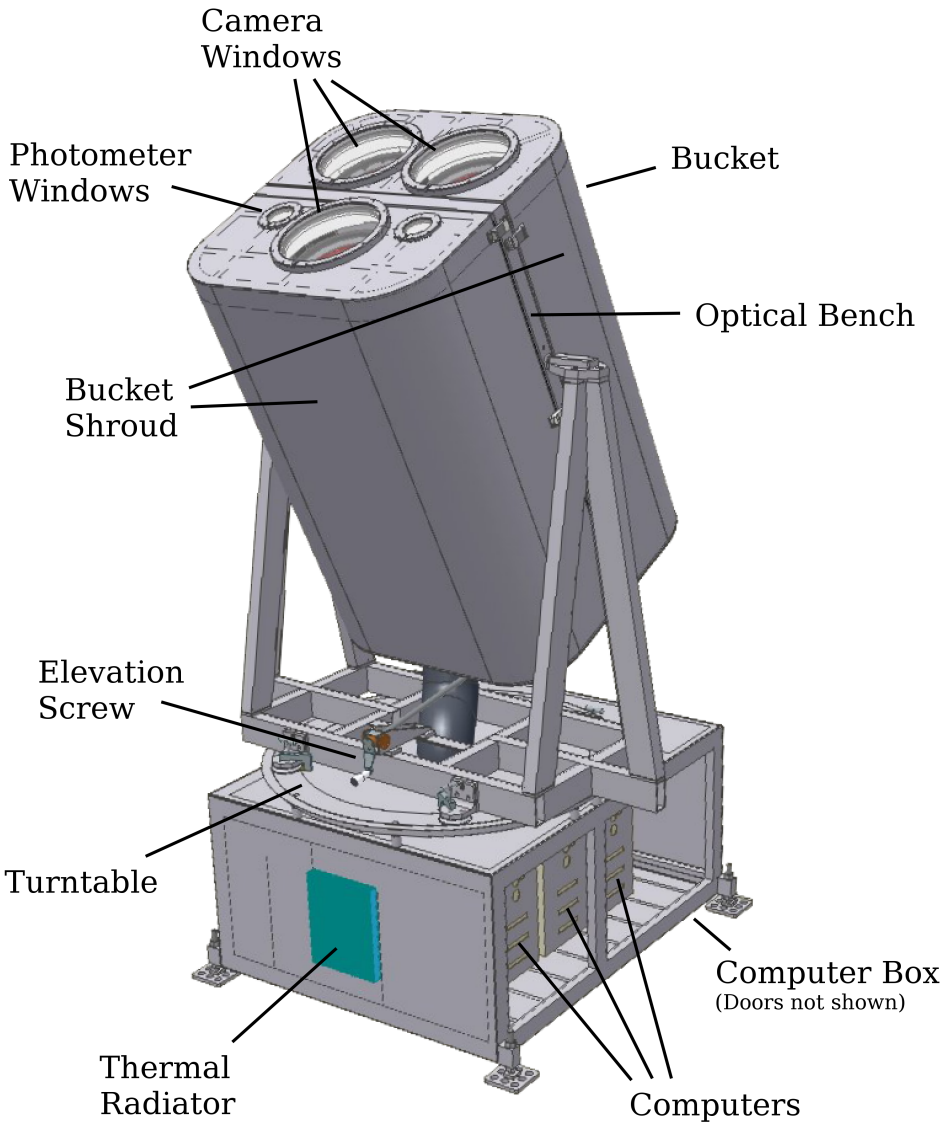

Figure 3.2: Labelled diagram of the ASK instrument.

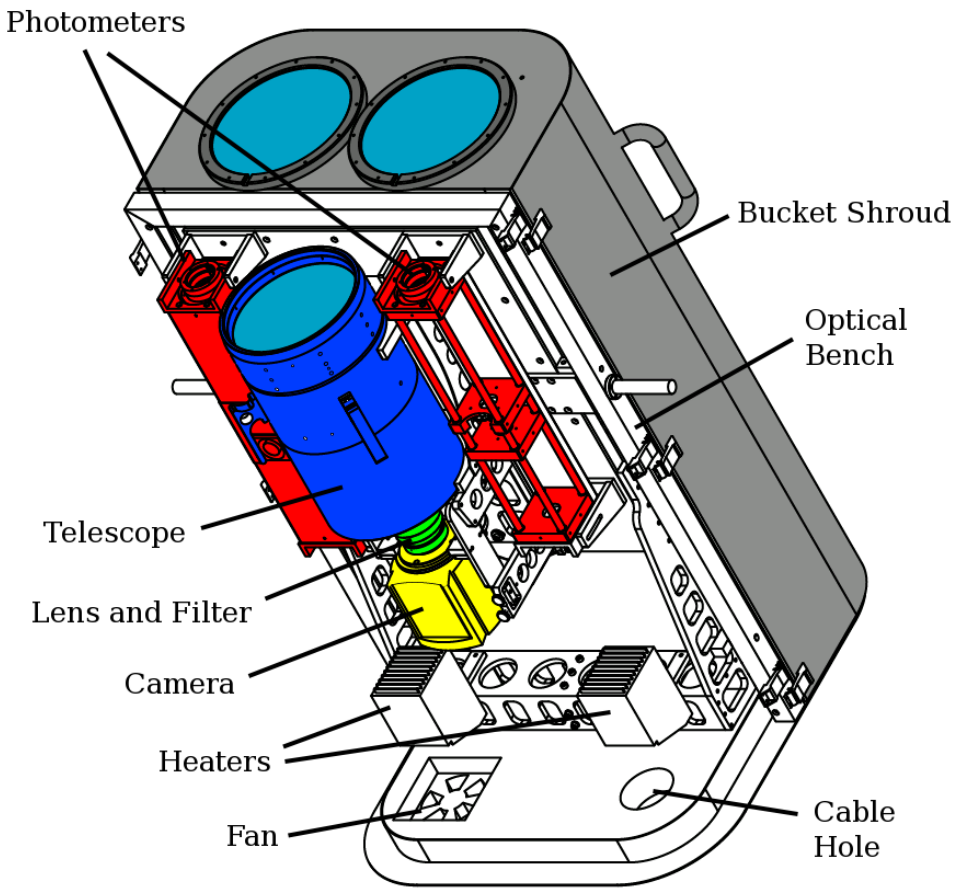

Figure 3.3: A diagram showing the arrangement inside the ASK bucket

to between 20°C and 25°C, but this system was improved with a new electronics box ("The Silverbox", described later) in October 2008. Several fans are also mounted in the base of the bucket to prevent temperature gradients from forming. An additional fan is mounted inside the opening of the one of the ducts, to draw warm air from the computer box into the bucket.

3.1.2 Data acquisition system

The data acquisition system for the ASK instrument was originally designed by *J. Höök* (2006) and N. Ivchenko. This system was in place with only minor software improvements until October 2008, when large parts of the system were replaced by N. Ivchenko, H. Dahlgren, and the author.

Images from all three cameras are acquired simultaneously, in "blocks" of 2 s, initially into the cameras' internal memory. Once a complete block is acquired the data are transferred to computers and written to disk. Mean images for each block are created by computer software (described later in this section) and are also written to disk. Blocks are acquired as part of a "megablock", nominally consisting of 600 blocks (20 minutes). A keogram (time series of a single column of pixels from the centre of the image) is created for each megablock from the mean images. Prior to the start of each megablock a series of images are acquired with the cameras' mechanical shutters closed, for calibration purposes (described in section 3.1.4). These sequences, known as "dark megablocks", are acquired at the same image rate as the standard megablocks, and are nominally 20 s long.

ASK camera images are initially acquired onto three computers in the computer box (hereafter referred to collectively as the camera computers); one computer is connected to each camera. These computers each have two hard disks in a Redundant Array of Independent Disks (RAID) configuration, providing about 250 GB of data storage space on each computer. Striped RAID level 0 (no redundancy) is used to maximise storage space and provide fast disk input/output. For the first observing season (winter 2005/06) the ASK cameras were typically operated at 5 Hz with no image binning. In October 2006 the standard image rate was increased to 20 Hz, with 2×2 binning. Both of these configurations produce the same data rate of 2.5 MiB/s per camera. The disks in the camera computers can therefore hold about 26 hours worth of data. When operating ASK in "campaign mode" in conjunction with the EISCAT radar the image (and data) rate is typically increased, such that the disks in the camera computers

can only hold about 16 hours worth of data. In order to run ASK continuously throughout the winter, accumulated data must be transferred from the camera computers at least once per day. A fourth ASK computer ("the ASK master") is located indoors. The ASK master computer has three disks for storage, also in a striped RAID 0 configuration. Originally these disks could hold about 400 GB of data, but in October 2008 they were upgraded by the author to have a total capacity of 840 GB. Each day data from the camera computers are transferred over ASK's internal computer network (TCP/IP) to the ASK master. Usually this is done remotely from Southampton or Stockholm over the Internet. Data are then written to Linear Tape-Open generation 2 (LTO-2) tapes with a capacity of 200 GB, which are stored with the ASK master and then carried back to Southampton and Stockholm by hand.

The amount of data transferred to the ASK master computer and written to LTO-2 tapes is reduced by careful exclusion of irrelevant data. This is done manually before transferring data from the camera computers to the ASK master. The keograms produced during acquisition are examined for evidence of aurora and clear skies. Data from other instruments co-located with ASK are also examined for evidence of auroral activity. Any megablocks which contain images of cloud only, or clearly have no auroral images, are deleted. The mean images are saved, so if useful data are accidentally deleted images will still be available at 2 s time resolution, although so far this has not happened. This selection process is necessary to reduce the amount of stored data both for practical and financial reasons. From 2006 onwards ASK has produced approximately 60–100 tapes (12–20 TB) of potentially useful data per year. Responsibility for the daily operation of ASK and selection of acquired data has mainly been shared between N. Ivchenko and H. Dahlgren at KTH in Stockholm and the author in Southampton.

All software for operating the instrument is stored on the ASK master, and is accessed by the three camera computers over the TCP/IP network, to ensure each camera functions in an identical manner. One piece of software is responsible for interfacing with the cameras and adjusting camera settings, reading images from the cameras and writing them to hard disk, managing megablocks and dark megablocks, and creating mean images and keograms in real-time. This software is known as the ASK daemon ("askd"). One instance of askd runs on each camera computer. The askd software was originally written by *J. Höök* (2006), but has been heavily modified by the author. The askd starts the camera in "run-till abort" mode, in which the camera waits for an external trigger before capturing

an image. The trigger is synchronised so that all three cameras capture images at exactly the same time.

Until October 2008 the trigger was provided by a National Instruments (NI) data acquisition card mounted in one of the camera computers. A Global Positioning System (GPS) 1 pulse per second (PPS) timing signal was used to provide an accurate timebase for the NI card. A second NI card was used to acquire photometer data. One of the NI cards also recorded readings from several temperature sensors placed around the instrument, as well as a light sensor placed inside one of the photometer windows. The NI cards were controlled by a piece of software called the NI daemon ("nid"), also written by *J. Höök* (2006). The nid software was able to monitor the light level and turn on and off the photometers automatically to prevent damage from moonlight or other bright sources. A black plastic box ("the Black Box") holding several connectors and electronic components was used as an interface between the NI cards and the cameras, photometers, sensors, and GPS antenna. Many problems were encountered when attempting to start the system after installation on Svalbard in 2007, mainly with the NI cards and the Black Box, and it was realised that this system was unreliable.

At the start of the 2008/09 observing season the NI cards and nid software were replaced by a custom-built printed circuit board (PCB) called the "Silverbox" together with a new piece of software called the "silverd", written by the author. The main components of the Silverbox are a field-programmable gate array (FPGA), microcontroller, and memory chip. A connection to one of the camera computers is made over a serial port. The main tasks of the FPGA are to generate timing pulses for the cameras, interface with the memory chip, switch power relays, and digitise photometer data and readings from temperature sensors and a light sensor. The photometer data and sensor readings can be accessed by the microcontroller, and are also formatted into data packets and stored in the memory chip. The microcontroller interprets commands from the computer (usually sent by the silverd software) and controls settings within the FPGA such as timing pulse frequencies. In addition the microcontroller manages memory readout to the computer (via the FPGA), and turns the photometers on and off (via the relays) based on the light sensor reading. The microcontroller also creates a human readable "heartbeat" message which is sent to the computer containing status information, including the sensor readings. As well as the photometer power, the heaters inside the bucket can also be switched using the relays. A

duty cycle algorithm is implemented in the microcontroller, adjusting the heat produced according to the temperature reading inside the bucket and the rate of change of temperature. This has led to far more stable temperatures than was possible using the thermostat, and a far more stable dark current in the cameras as a result. The Silverbox clock signal is controlled by a crystal oscillator with a variable (voltage controlled) frequency. The frequency is synchronised to a 1 PPS signal provided by a GPS chip mounted on the Silverbox PCB, by adjusting the oscillator frequency based on the phase difference between the 1 PPS signal and the clock signal. This ensures the timing signals sent to the cameras have a very accurate frequency. N. Ivchenko was responsible for programming the FPGA while the author was responsible for programming the microcontroller.

The silverd software runs on one of the camera computers and acts as the controlling piece of software for the whole ASK instrument. It sends commands to the attached Silverbox to set camera and photometer frequencies and start and stop the timing signals, and is also responsible for transferring data from the Silverbox memory chip to the computer hard disk. It has control over the three instances of the askd via network socket messages, and monitors the status of the three cameras to ensure operations such as starting the timing signals happen at the correct time. The silverd also monitors the light sensor reading and stops the cameras if the light level gets too high. When the light level drops the silverd restarts the cameras. It is therefore possible to leave ASK running continuously with minimal input from the operator, other than selecting data for deletion and writing data to LTO-2 tapes. The askd and silverd (or nid) share a common configuration file created by the operator, which contains all settings such as camera image frequencies, the directories in which to store data on disk, and the network addresses of the computers.

The askd, nid, and silverd are all written in the C++ programming language. However, for ease and speed of operation several Linux shell scripts are usually used by the operator to start, stop, and control these pieces of software. In addition, camera images and keograms are created in Portable Network Graphics (PNG) format in real-time by two shell scripts running in a loop, for display on the ASK instrument web page (currently `http://ask1.esr.eiscat.no/`). These scripts also create simple plots of the photometer measurements, temperature sensor readings, and light level in real-time, as well as providing information on the computer disk usage and cameras' status. This web page is used by operators to monitor the instrument and observations.

Filter	Target Species	Central Wavelength	Width (FWHM)
1	O_2^+ 1N	562.0 nm	2.6 nm
2	N_2 1PG	673.0 nm	14.0 nm
3	O ($3p^5P$)	777.4 nm	1.5 nm
4	O^+ (^2P)	732.0 nm	1.0 nm
5	N_2^+ 1N	427.8 nm	3.5 nm

Table 3.1: ASK camera filters.

Combination	ASK1	ASK2	ASK3
1	562.0 nm (1)	732.0 nm (4)	777.4 nm (3)
2	673.0 nm (2)	732.0 nm (4)	777.4 nm (3)
3	427.8 nm (5)	673.0 nm (2)	777.4 nm (3)

Table 3.2: ASK camera filter combinations.

3.1.3 Observed emissions

A set of five filters is currently available for the ASK cameras, listed in table 3.1. Three filter combinations, listed in table 3.2, have been made from this set to allow various studies of the aurora. Only the ASK1 and ASK3 cameras as part of filter combinations 1 and 2 have been used in this work. By convention emissions observed with ASK are referred to as I_a in this thesis, where a is the central wavelength of the relevant filter.

The 562.0 nm, 673.0 nm, and 427.8 nm emissions are all sensitive primarily to high-energy electron precipitation, due to their origin in the excitation of molecular species at low altitudes (E-region ionosphere). The 777.4 nm emission comes from a transition in atomic oxygen, and is sensitive primarily to low-energy electron precipitation. Using the emission intensity ratio ASK3/ASK1 (e.g. 777.4 nm/673.0 nm) in combination with ionospheric modelling it is possible to estimate the energy of precipitating electrons. This is discussed in more detail in chapter 4. The 732.0 nm emission is also a result of electron impact on atomic oxygen and is therefore sensitive primarily to low-energy electrons. However, the transition emitting at 732.0 nm (O^+ ^2P – ^2D) is forbidden, with its origin in a meta-stable state, leading to a long radiative lifetime of about 5 s. This long lifetime is useful for the study of plasma flows in the ionosphere (*Dahlgren et al.*, 2009), but makes the emission unsuitable for direct comparison with emissions observed by the other ASK cameras for estimation of electron precipitation energies. The 427.8 nm filter (as part of filter combination 3) was tested during early 2007. It was found that a combination of a low filter transmission factor

(∼50% peak) and a low quantum efficiency of the EMCCD detector at this short wavelength led to very low measured intensities, so much so that the 427.8 nm filter has not been used at any other time since initial testing. Modelled altitude profiles of the volume emission rates for the three main ASK emissions used in this work are shown in figures 4.2 and 4.3, and are discussed fully in chapter 4.

N_2 1PG (673.0 nm filter) emission

The 673.0 nm filter passes emission from the N_2 $B^3\Pi_g$–$A^3\Sigma_u^+$ transition (N_2 1PG band), specifically the (4,1) and (5,2) bands. The emission is emitted by molecular nitrogen excited by predominantly high-energy auroral electrons. Due to the wide filter transmission curve of 14.0 nm measuring with this filter provides the best signal-to-noise ratio when compared to the other ASK camera filters. This makes it ideal for use in high-resolution spatial studies of the aurora. Data obtained using this filter were analysed for the spatial study of flickering aurora presented in chapter 5 of this thesis.

O_2^+ 1N (562.0 nm filter) emission

The 562.0 nm filter passes emission from the O_2^+ 1N(1,0) and O_2^+ 1N(2,1) bands. These emissions are the result of excitation by predominantly high-energy electron precipitation on molecular oxygen. One advantage of using this filter instead of the 673.0 nm filter is that the O_2^+ emission passed through this filter is also observed by the HiTIES instrument (not used in this work), located close to ASK on Svalbard.

O ($3p^5P$) (777.4 nm filter) emission

ASK3 has always been fitted with an interference filter centred on 777.4 nm, measuring an emission line from an atomic transition from O ($3p^5P$). This emission is most efficient for low-energy electrons. It is a result of two distinct processes in the ionosphere: Direct excitation of atomic oxygen and dissociative excitation of molecular oxygen. The direct excitation process dominates for low-energy electron precipitation, while the dissociative excitation process dominates for high-energy electron precipitation.

Filter	Target Species	Central Wavelength	Width (FWHM)
1	N_2^+ 1N	470.9 nm	1.0 nm
2	O	844.6 nm	1.7 nm

Table 3.3: ASK photometer filters in use during winter 2006/07.

Emissions observed with photometers

A set of four filters is available for the two ASK photometers. During winter 2006/07 the photometers were fitted with spectral filters centred on 470.9 nm and 844.6 nm, which select emissions of N_2^+ 1N and O respectively. These are summarised in table 3.3. As the 470.9 nm emission results from electron impact ionisation of molecular oxygen, the emission production is weighted towards precipitation of high-energy electrons in the ionosphere. The 844.6 nm emission results from a similar transition to the 777.4 nm emission observed with the ASK3 camera, and has a similar dependence on electron energy.

3.1.4 Calibration

ASK camera images are both geometrically and absolute intensity calibrated. Both types of calibration are briefly described in this section.

Intensity calibration

The total intensity (counts/s) measured by a camera pixel comes from several sources: the aurora; background light such as airglow and moonlight; and the "dark current". Intensity calibration is the process of correcting images to provide a measure of the intensity of the target (the aurora) only. Absolute intensity calibration is the process of converting intensity measurements made in arbitrary units (counts/s) to meaningful units (Rayleighs) for comparison with other instruments. The total intensity measured in a camera pixel is given by:

$$I_{tot} = (I_{aur} + I_{air})\, C_{PRNU} + I_{dark} \tag{3.1}$$

where I_{tot} is the total intensity, I_{aur} is the auroral intensity, I_{air} is the intensity of airglow and other background light, I_{dark} is the intensity due to dark current, and C_{PRNU} is a constant factor (pixel-by-pixel) to correct for photo response non-uniformity (PRNU).

Absolute intensity calibration of the ASK cameras is performed by measuring

Camera and filter	Sensitivity
ASK1, 673.0 nm	1.92 counts/s/pixel/R
ASK1, 562.0 nm	2.00 counts/s/pixel/R
ASK3, 777.4 nm	1.11 counts/s/pixel/R

Table 3.4: ASK camera sensitivities obtained by absolute intensity calibration using stars.

the brightnesses of stars (in units of counts) in a clear image (no cloud or aurora) and comparing them to theoretical brightnesses (in Rayleighs) obtained from a star catalogue. For each star the image intensity is integrated over the pixels containing the star, and then a background obtained from the region surrounding the star is subtracted, leaving a value for the number of counts measured due to light from the star. This is done for a large number of stars from a large number of images. The theoretical observed brightness of each star is calculated by convolving its wavelength spectrum with the ASK filter transmission curve and integrating the result. Several star catalogues and spectra classifications have been used to estimate the spectrum of each star. By fitting a large number of theoretical and observed stellar brightnesses values for the camera sensitivity can be obtained. The sensitivities of the ASK1 and ASK3 cameras during late 2006 (when data used in this thesis were acquired) are listed in table 3.4. The ASK photometers were not absolute intensity calibrated until late 2010, using a different process to that used for the cameras.

Dark current is intensity measured by a pixel which is not caused by light falling on the pixel (I_{dark} in equation 3.1), and must be subtracted from the total intensity before absolute intensity calibrating the image. It is mainly caused by thermal noise within the camera electronics. The dark megablock recorded immediately prior to a megablock (see section 3.1.2) is used to produce a "dark image" for that megablock. The images in the dark megablock are averaged together pixel by pixel, with outliers (usually caused by cosmic rays) excluded. As no light is falling on the EMCCD during acquisition of the dark megablock the resulting image is a measure of the dark current present in the camera electronics, which fluctuates with temperature. During data analysis the dark image is subtracted from the sky images, leaving signal resulting from light falling on the EMCCD only.

Dark-corrected sky images are divided by a normalised "flat image" to correct for PRNU, which is differences in pixel sensitivity due to both electronic and

optical effects. The flat image is made in a similar way to the dark image, but using images of uniform cloud from a megablock instead of images from a dark megablock. The flat image is normalised to have a mean value of 1, and so dividing sky images by the flat image does not affect absolute intensity calibration.

When analysing ASK data each camera and photometer are background corrected independently, to remove contamination from airglow and other irrelevant emissions (I_{air} in equation 3.1). This is done by averaging images from a clear period with no cloud or aurora close (in time) to the event being studied, and then subtracting the resulting background image from the event data. This process is performed after the other intensity calibration processes.

Geometrical calibration

Geometrical calibration of the camera images is done by matching observed star constellations with a theoretical image of the star field generated from the Smithsonian Astrophysical Observatory (SAO) star catalogue. Initial estimates for the camera pointing direction are required. The constellations are then matched manually, before a fitting process is performed to generate a set of coefficients for converting image pixel location to azimuth and elevation coordinates. These coefficients can also be used to perform the reverse transformation, converting azimuth and elevation coordinates to pixel numbers in the image plane.

3.2 Reimei

Reimei is the first satellite to make multi-spectral optical measurements of the aurora and measurements of precipitating particles on the corresponding field line simultaneously. It is a Japanese microsatellite in a sun-synchronous orbit at a height of about 620 km, launched as a technology demonstration satellite (*Saito et al.*, 2001) and previously known as INDEX. Its scientific payload consists of the Electron Spectrum Analyzer (ESA) and Ion Spectrum Analyzer (ISA) particle detectors (*Asamura et al.*, 2003) and the Multi-spectral Auroral Camera (MAC) optical imaging system (*Obuchi et al.*, 2008; *Sakanoi et al.*, 2003). The satellite is three-axes stabilised, and can be flown such that the geomagnetic footprint of the satellite passes through the field of view of MAC while ESA/ISA simultaneously measure auroral particle precipitation (*Asamura et al.*, 2003; *Sakanoi et al.*, 2003). This is known as "Mode-S", and is very useful for studies of auroral features and

the acceleration mechanisms leading to them. An alternate mode in which the field of view of MAC is directed almost parallel to the direction of orbital motion allows observations of the height distribution of auroral emission ("Mode-H"). All data analysed in this thesis were acquired while the satellite was operating in Mode-S.

The MAC system consists of three co-aligned cameras each with a narrow field of view covering ∼80 × 80 km at 100 km altitude. Each camera is equipped with a different spectral filter. The first camera (channel 1) observes emission in the N_2^+ 1N(0,1) band, with a filter centred at 427.8 nm. This is known as the auroral blue line. The second camera (channel 2) observes the auroral green line centred at 557.7 nm, resulting from emission by atomic oxygen. This is the emission which gives the aurora its distinctive green colour. The third camera (channel 3) observes emission in the N_2 1PG (3,0), (4,1), (5,2), (6,3), and (7,4) bands, with a filter centred on 670.0 nm. This filter is similar to the 673.0 nm ASK filter, but transmits light from a wider wavelength region. For all data analysed for this thesis MAC has a time resolution of 120 ms with an exposure time of 60 ms.

ESA is a top-hat type electron spectrometer, described fully by *Asamura et al.* (2003). It measures precipitating electrons in 32 energy bins covering a range of 12 eV to 12 keV. ESA records a complete electron energy spectrum over all 32 bins every 40 ms.

ISA is a similar instrument to ESA but for measuring precipitating ions (e.g. protons) instead of electrons. ISA has not been used for work presented in this thesis.

3.3 European Incoherent SCATter Radar

Incoherent scatter radars are able to measure several properties of the ionospheric plasma: electron concentration, ion temperature, the ratio of electron to ion temperature, ion composition, and the line of sight plasma drift velocity. The EISCAT Scientific Association operates three radar systems across northern Scandinavia. These are ultra high frequency (UHF) and very high frequency (VHF) systems in mainland Scandinavia and a UHF system located on Svalbard (the EISCAT Svalbard Radar, ESR). The mainland UHF system is tristatic, with two remote receiving sites in Kiruna, Sweden and Sodankylä, Finland complimenting the transmitting and receiving antenna in Tromsø, Norway. The VHF system

Figure 3.4: A photograph of the EISCAT UHF radar in Tromsø, taken by the author.

consists of a single transmitting and receiving antenna in Tromsø. For this work only the mainland UHF system in Tromsø was used, as all ASK data used were acquired in late 2006 when ASK was stationed in Tromsø. A photograph of the UHF antenna in Tromsø is shown in figure 3.4. The radar control room and transmitter hall can be seen in front of the antenna.

The incoherent scatter radar (ISR) technique involves illuminating the ionosphere with a powerful radar beam at a specific frequency and then measuring the back-scattered spectrum, from which various properties of the ionospheric plasma can be derived. Most of the radar signal travels straight through the ionosphere and out into space, but a small fraction is scattered by weak gradients in electron concentration (incoherent scatter). The motion of the ionospheric electrons is heavily dominated by the more massive and slow moving ions, and therefore the electrons have a collective behaviour imposed by the ions. For a thermal plasma the shape of the back-scattered spectrum is determined by the electron concentration, ion and electron temperatures, ion composition, and line of sight plasma drift velocity. Therefore it is possible to derive these parameters from a mea-

sured spectrum. However, since the plasma wave fluctuations responsible for the returned spectrum are stochastic, a single radar measurement is not individually useful. Instead an autocorrelation function (ACF) is formed by cross-correlating the returned spectrum with itself. The ACF is the Fourier transform of the incoherent scatter spectrum, and so accurate values for the plasma parameters can be determined by forming an ACF over a sufficiently long series of measurements. Since the return time of a transmitted radar pulse is dependent on the distance it has travelled the leading edge of the received pulse comes from the lowest scattering altitude while the trailing edge comes from the highest altitude. By gating the received signal it is possible to form altitude profiles of the various plasma parameters.

Another method of estimating the electron concentration altitude profile is by simply scaling the total returned power, forming what is known as a "power profile". While less accurate than fitting the incoherent scatter spectrum, power profiles can have a better time resolution than usual ionospheric ISR measurements. This is because is it necessary to use fairly long integration times (seconds to 10s of seconds) to reduce noise to a sufficiently low level that it is possible to fit the incoherent scatter spectrum. For studies of small-scale rapid aurora the best time resolutions are necessary. Radar data used in this thesis were acquired using the "arc1" experiment program run on the mainland EISCAT UHF radar, which includes power profiles with a 0.44 s time resolution. While this resolution is an order of magnitude worse than the resolution of ASK measurements, it is significantly better than the 4 s resolution fitted spectrum data are available at with this program.

ISR measurements of the incoherent scatter spectrum made by transmitting a simple radar pulse (a "long pulse") and then receiving it some time later are limited to measuring ionospheric parameters in the F2 layer, above the brightest and most important auroral emissions. This is because at lower altitudes the ionospheric correlation time at radar frequencies becomes longer than the minimum radar pulse length giving a range resolution equal to the scale height. To combat this problem various pulse coding techniques have been developed, including multi-pulse measurements (*Farley*, 1972), random codes (*Sulzer*, 1986), alternating codes (*Lehtinen and Häggström*, 1987), and Barker codes (*Turunen et al.*, 1985; *Lehtinen et al.*, 2002). As well as allowing measurements in the E-region and D-region, these codes can improve range and time resolution. The arc1 experiment program uses an alternating code technique, providing measurements

of the incoherent scatter spectrum between 96 km and 422 km with a best range resolution of 0.9 km. However, only power profiles have been used in this thesis, and therefore details of the coding scheme are not discussed further.

Chapter 4

Modelling

While the Southampton Ionospheric Model was written before the start of this PhD, the author has been involved in recent software modifications to improve the running and application of the model, and was also responsible for extending the model to simulate emissions observed by Reimei.

4.1 The Southampton Ionospheric Model

A combined electron transport (*Lummerzheim and Lilensten*, 1994) and time-dependent ion chemistry model (see appendix in *Lanchester et al.*, 2001) has been used in this work. The model (hereafter referred to as the Southampton Ionospheric Model) solves the coupled continuity equations time-dependently for all important positive ions and minor neutral species. The main input to the model is an electron energy spectrum precipitating at the top of the ionosphere (500 km in the model). This can be specified as a sum of Gaussian and Maxwellian components with an optional power law at low energies, or as an arbitrary spectrum, for example as obtained from satellite data. The model utilises the MSISE-90 model to provide concentrations of the three major neutral species, which are molecular nitrogen (N_2), molecular oxygen (O_2) and atomic oxygen (O). At each time step (typically chosen to match the time resolution of observations) the electron transport code is run once, followed by the ion chemistry code. The electron transport code calculates ionisation and excitation rates together with the degraded electron spectrum at each altitude. Backscattered and secondary electrons are also included. From the ionisation and excitation rates it is possible to calculate many different auroral emission rates. The ion chemistry code is

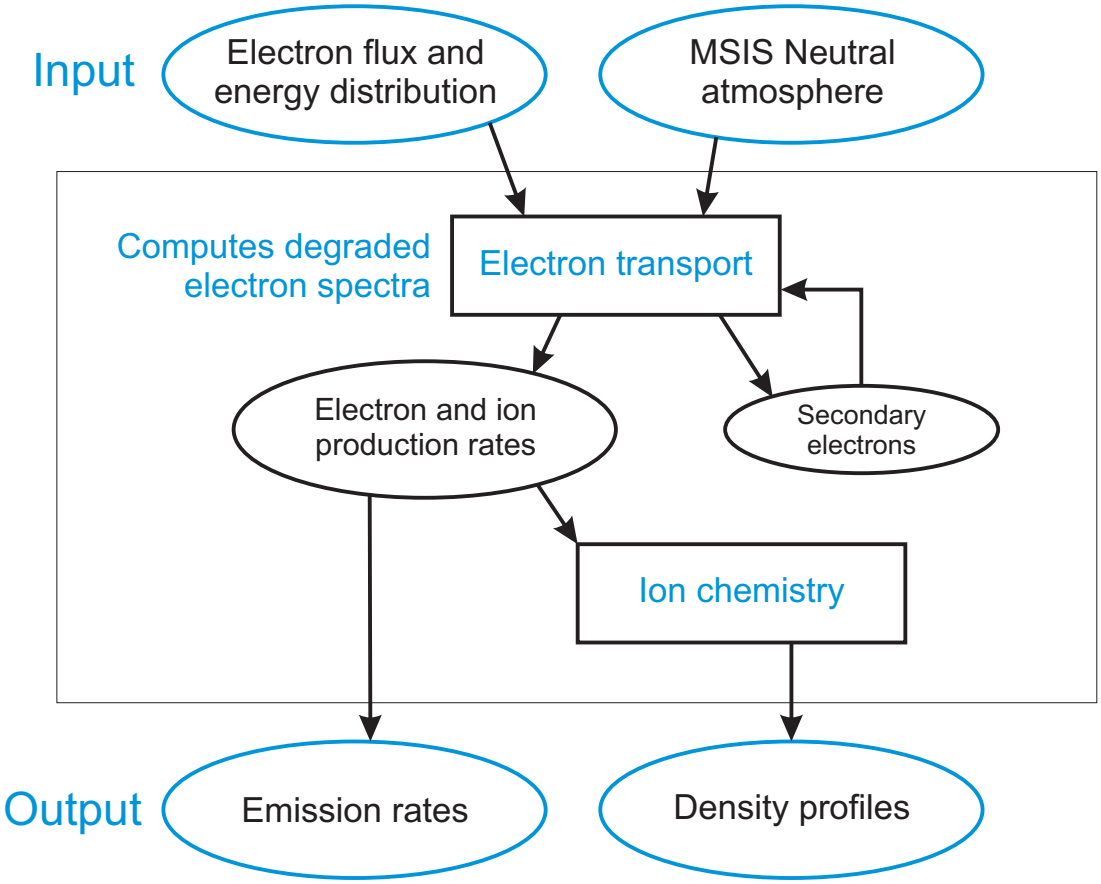

Figure 4.1: Basic flow diagram of the Southampton Ionospheric Model.

run after the electron transport code, and solves various chemical equations time dependently to produce concentration altitude profiles for a large number of ion species, as well as the electron concentration profile. A basic flow diagram of the model is shown in figure 4.1. This illustrates the processes applied during a single time step. The ion composition profiles calculated during this time step are then used as the starting ionosphere for the next time step.

Volume emission rates are calculated in different ways depending on the particular emission, but usually involve multiplying the rate of electron impact excitation of the relevant species by a factor containing branching ratios or other similar coefficients. Modelled altitude profiles of the volume emission rates relevant to the ASK observations studied in this thesis are shown in figures 4.2 and 4.3. In both cases a Gaussian input electron spectrum was used with a total flux of 1 mW/m^2. The peak energy of the Gaussian was 1 keV in the case of figure 4.2 and 10 keV in the case of figure 4.3. As is to be expected the peak emission altitude for all emissions is lower for the higher energy input spectrum

(figure 4.3). As described in section 3.1.3 two processes lead to the 777.4 nm emission. These two processes were modelled separately, and are shown as dotted (dissociative excitation) and dashed (direct excitation) blue lines. The total 777.4 nm emission is shown as a solid blue line. The profile for 777.4 nm emission produced by dissociative excitation of O_2 closely resembles the profile for the O_2^+ 1N (562.0 nm) emission (black line), as both emissions depend primarily on the concentration of molecular oxygen (O_2). The 777.4 nm emission produced by direct excitation of O (dashed blue line) depends primarily on the concentration of atomic oxygen, and therefore has a different profile shape, with a larger proportion of the emission coming from higher altitudes. The N_2 1PG emission (red line) depends primarily on the concentration of molecular nitrogen, with a profile shape quite similar to that for O_2^+ 1N.

By integrating the volume emission rate profiles in altitude the emission intensity on the ground can be calculated. Figure 4.4 shows the model brightnesses of the three main ASK emissions used in this study as the peak energy of a Gaussian electron distribution was varied at a constant flux of 1 mW/m^2. The top panel of the figure shows the absolute brightnesses as would be observed through the ASK instrument filters (the filter transmission curves were taken into account). The two processes producing 777.4 nm emission are plotted individually, together with the total 777.4 nm emission. The bottom panel shows two emission ratios: I_{7774} / I_{6730} and I_{7774} / I_{5620}, hereafter referred to as OI/N_2 and OI/O_2^+ respectively. The local time, location, and geomagnetic conditions (specifically the Ap index and F10.7 solar radio flux) were included in the model. Therefore the ratios plotted apply specifically to observations made using ASK on 22 October 2006 (for 673.0 nm) and 12 December 2006 (for 562.0 nm) which are analysed in chapters 5 and 6. The ratios have a clear dependence on electron precipitation energy. Therefore the observed ratio between I_{7774} (ASK3) and I_{6730} or I_{5620} (ASK1) can be directly related to the energy of auroral electron precipitation (*Lanchester et al.*, 2009).

Figure 4.5 shows the modelled brightnesses of the three main ASK emissions as the peak energy of a Maxwellian electron distribution was varied at a constant flux of 1 mW/m^2. Note that the energy axis scale is different to that for figure 4.4. The model cannot provide accurate emission brightnesses for Maxwellian distributions with a peak energy above about 10 keV, as the amount of flux at very high energies above the maximum energy considered in the model (approximately 70 keV) becomes too large. Also, errors appear in the model as very high energy electrons

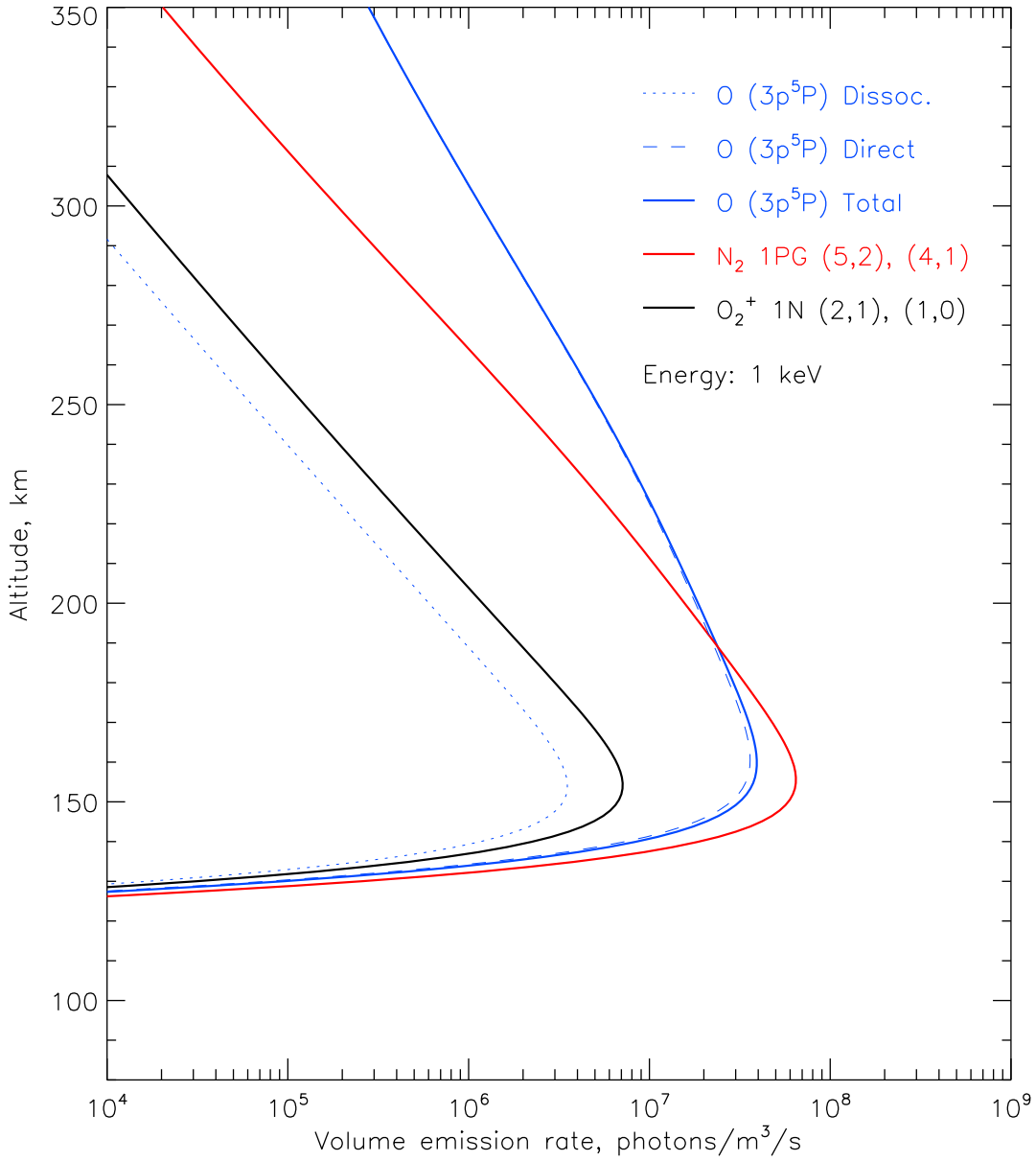

Figure 4.2: Modelled volume emission rate profiles of the three main ASK emissions for a 1 mW/m^2 Gaussian electron spectrum peaking at 1 keV.

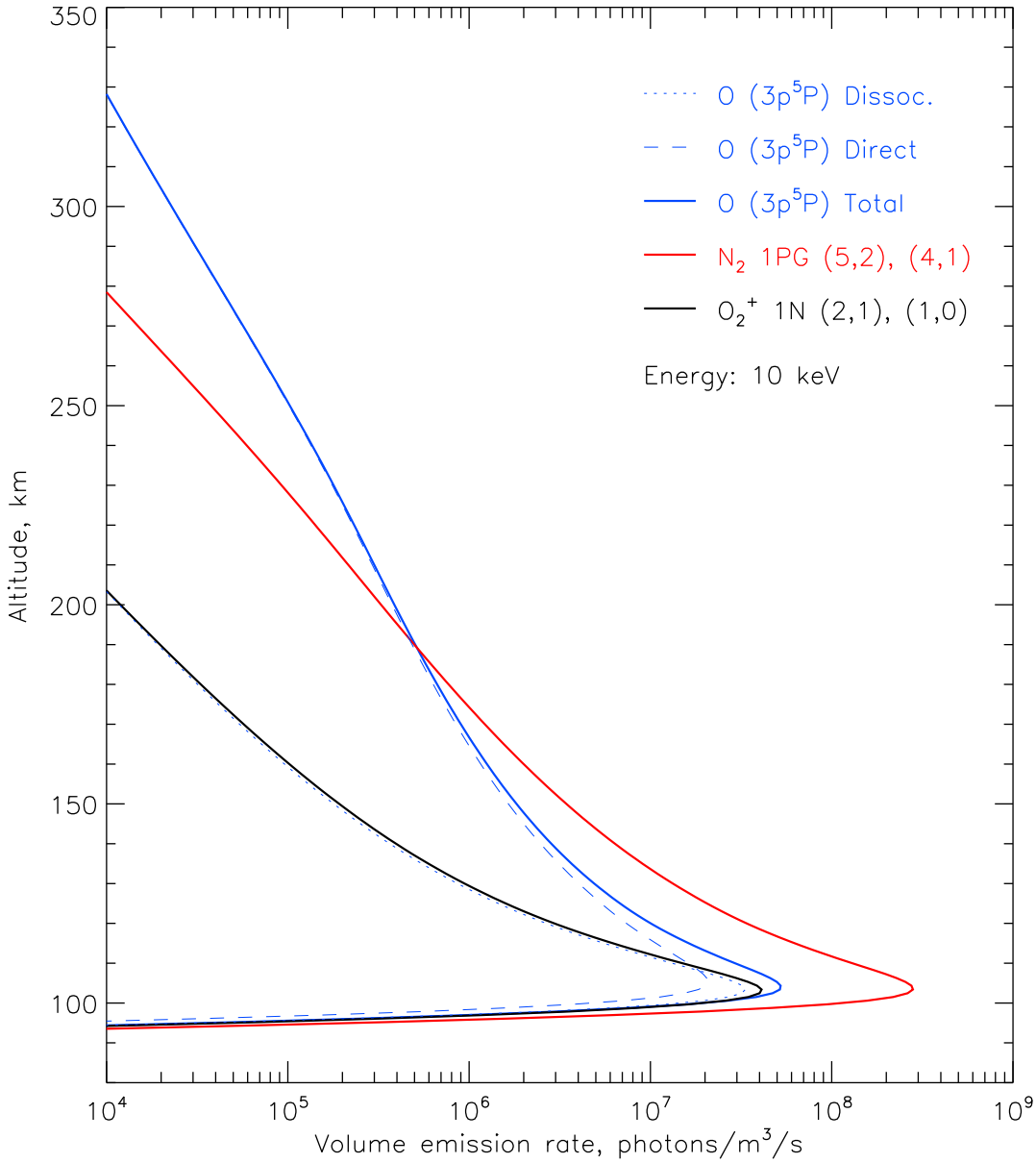

Figure 4.3: Modelled volume emission rate profiles of the three main ASK emissions for a 1 mW/m^2 Gaussian electron spectrum peaking at 10 keV.

pass through the lower border of the model altitude grid (80 km). While in many cases Maxwellian distributions more accurately represent real world conditions than Gaussian distributions, flickering aurora is most likely not well represented by a Maxwellian distribution. Observations of FABs typically show velocity-dispersed electrons in a narrow energy range, and none of the existing theories for flickering aurora could explain electron distributions with a significant high-energy tail. For these reasons all energy estimates made in this thesis use Gaussian electron distributions.

The estimated systematic uncertainty in modelled ASK emission brightness is 35%. Errors in the electron transport model are discussed in detail by *Lummerzheim and Lilensten* (1994). The main sources of error in modelled auroral emissions are related to the input parameters, rather than in any numerical calculations. Two inputs introduce most error: the cross-sections and the neutral density profiles. Errors in cross-sections have been minimised by using recent estimates and by evaluating different cross-section estimates with observations (e.g. *Ashrafi et al.*, 2009).

Uncertainties in the MSISE-90 model will have a significant impact on results from the Southampton Ionospheric Model. The relative intensities of the auroral emissions depends on the relative concentrations of the neutral species. For example when the atomic oxygen concentration is large compared to the concentrations of other species the auroral emissions produced by excitation or ionisation of atomic oxygen will be more intense, as a larger fraction of precipitating and secondary electrons will interact with atomic oxygen instead of other species. As the main source of auroral emissions from the excitation of neutrals are secondary electrons rather than primary precipitating electrons, the altitude profile of these auroral emissions is chiefly decided by the altitude at which primary electrons deposit their energy, rather than the energy of the primary electrons directly. Figure 4.6 shows the emission cross-section for the ASK and Reimei observations of N_2 1PG emission as a function of electron energy. Despite the fact that these emissions are sensitive to precipitating electrons with energies of several keV (see figure 4.4), the emission cross-sections decrease rapidly past a peak at less than 20 eV, showing that the high-energy precipitating electrons do not produce significant auroral emission directly. The altitude at which precipitating electrons deposit their energy is largely decided by the concentration profiles of the major neutral species, which are provided by the MSISE-90 model for the Southampton Ionospheric Model. Primary electrons play a larger role in directly producing

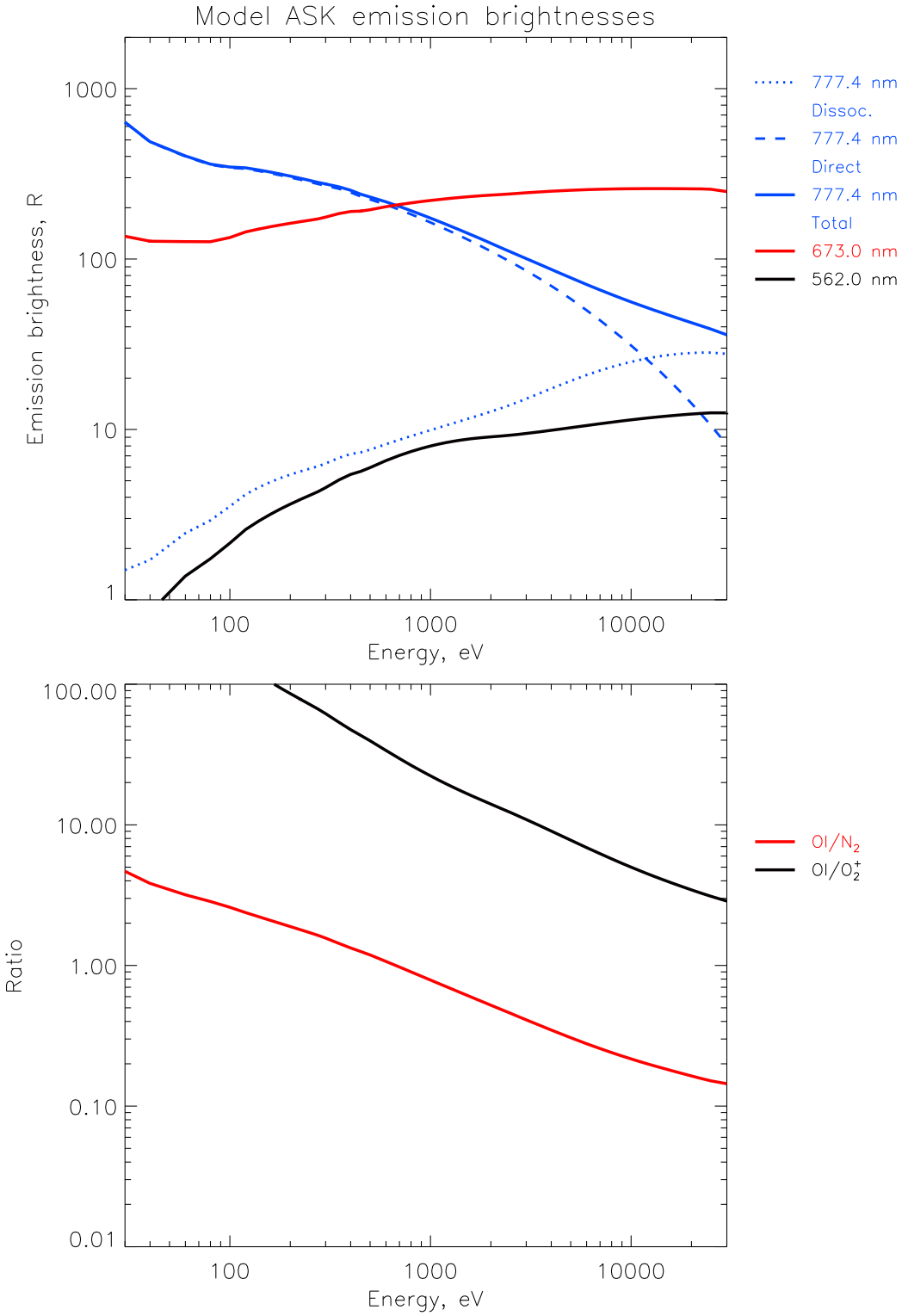

Figure 4.4: Modelled ASK emission brightnesses (top panel) and associated ratios (bottom panel) as functions of energy, for Gaussian shaped electron spectra.

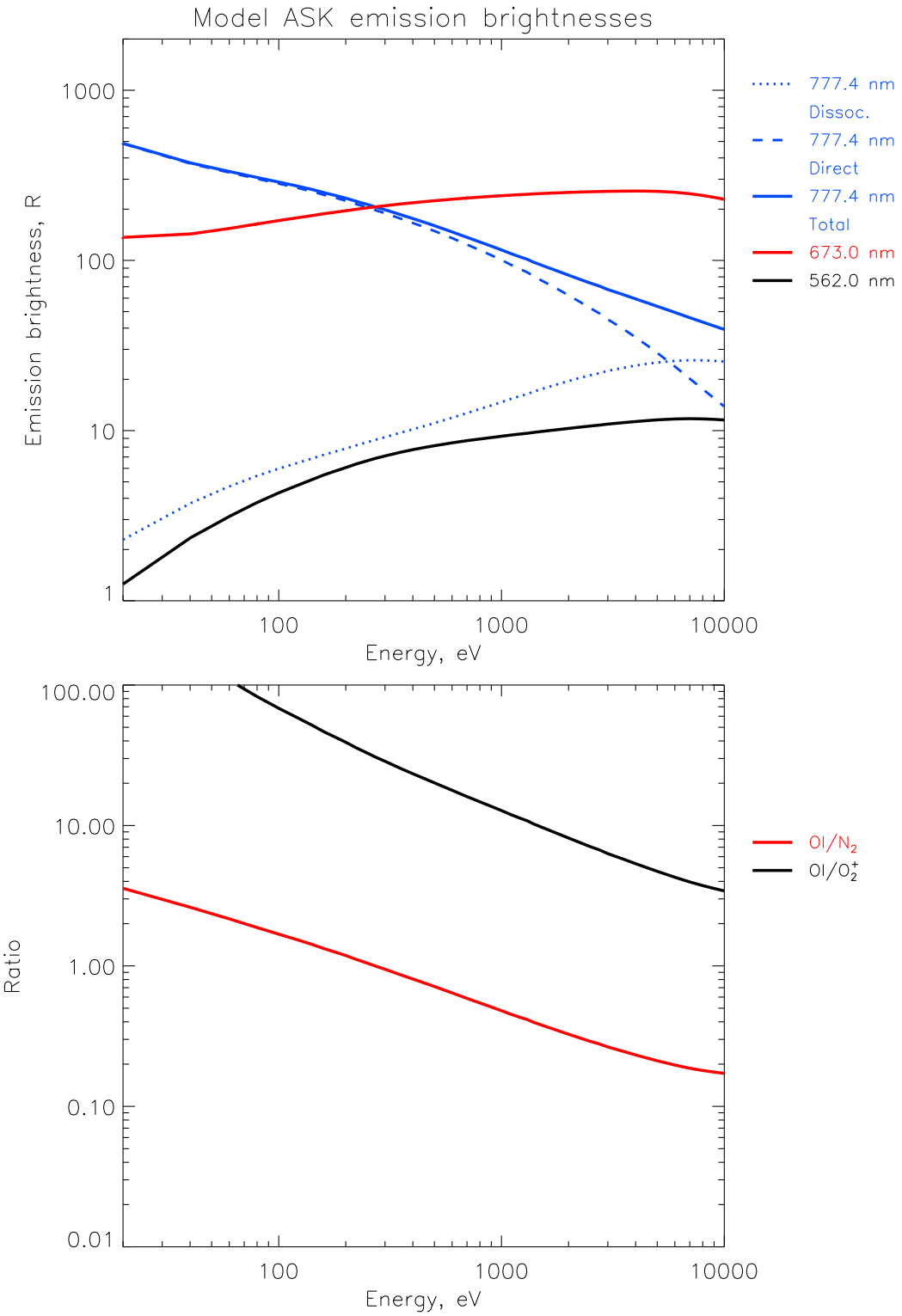

Figure 4.5: Modelled ASK emission brightnesses (top panel) and associated ratios (bottom panel) as functions of energy, for Maxwellian shaped electron spectra.

auroral emissions originating from ionisations rather than only excitations, as the ionisation cross sections peak at higher energies ($\sim 10^2$ eV) and are still of significant size at keV energies (e.g. *Solomon et al.*, 1988; *Itikawa*, 2005). However, the altitude of ionisations by primary electrons still depends on the neutral concentration altitude profile; ionisations are more likely to occur where there is a larger concentration of neutrals.

4.2 Modelling Reimei observations of N_2 1PG

When modelling emissions originating from molecular species the emission cross-sections used often have to be calculated for a specific instrument, as different instruments observe different parts of the wide (in wavelength) band structure. The emission cross-section for the N_2 1PG system as observed by ASK was calculated by *Ashrafi et al.* (2009). In this case only the (5,1) and (4,2) bands of N_2 1PG are included in the cross-section. This is not suitable for modelling the Reimei observations of N_2 1PG, as MAC uses a filter covering a much wider wavelength range, as described in section 3.2. An equivalent cross-section covering the 5 bands observed by Reimei was calculated in the same manner, following the method briefly described here.

Firstly the emission cross-section for each specific band i (e.g. (4,1) band), $C_i(e)$, is calculated using

$$C_i(e) = \sum_{\forall j} W_{i,j}\sigma_j(e) \tag{4.1}$$

where $\sigma_j(e)$ is the excitation cross-section for the transition from the ground state to a state j and $W_{i,j}$ is a weighting factor obtained by multiplying the steady state population of the band's transition parent level by the Einstein coefficient for the transition. The parent level population is found using Franck-Condon factors, accounting for cascading. For this work the excitation cross-sections σ were taken from the review by *Itikawa* (2005) and the weighting factors W were calculated by O. Jokiaho. The product $W_{i,j}\ \sigma_j(e)$ is summed over all states: B, A, C, B′, W. Both $C_i(e)$ and $\sigma_j(e)$ are functions of electron energy, e. The total emission cross-section for the MAC 670.0 nm observations is then calculated by summing $C_i(e)$ over the 5 observed bands, as follows:

$$C_{\mathrm{MAC}}(e) = C_{(3,0)}(e) + C_{(4,1)}(e) + C_{(5,2)}(e) + C_{(6,3)}(e) + C_{(7,4)}(e) \tag{4.2}$$

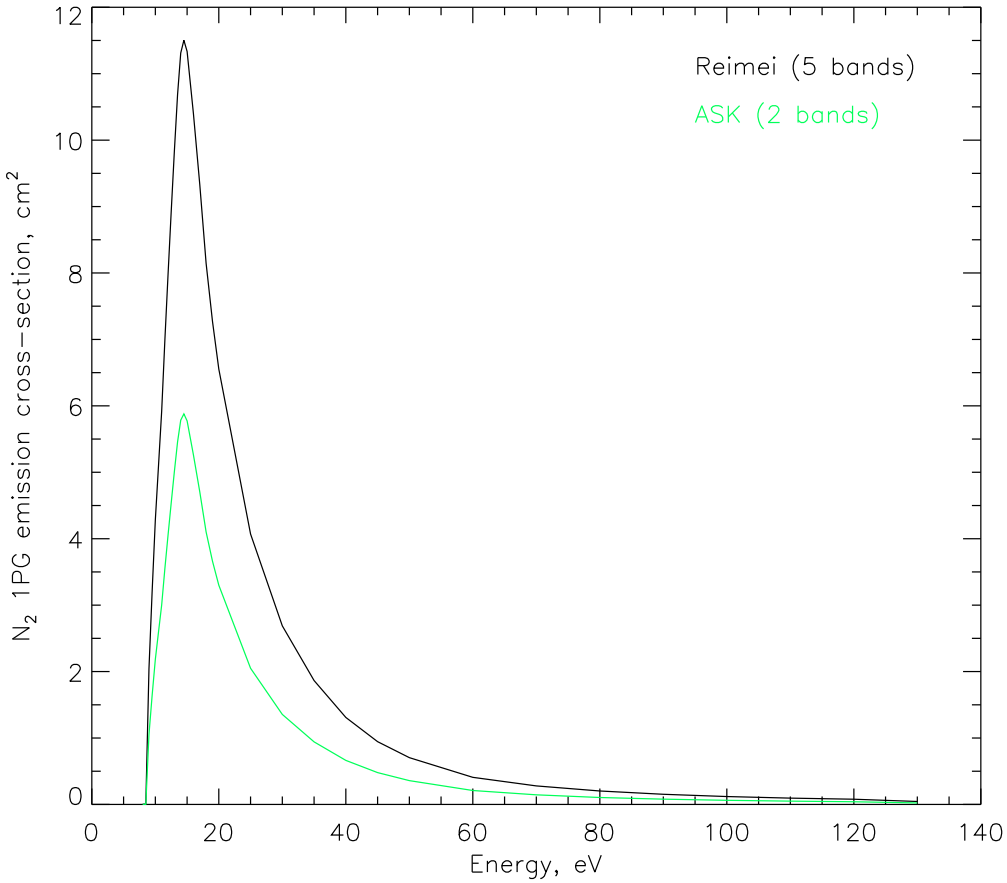

Figure 4.6: Emission cross-section for Reimei and ASK N_2 1PG observations.

The emission cross-section used in the model for Reimei and ASK N_2 1PG observations is plotted in figure 4.6 as a function of electron energy. The cross-section is larger for Reimei observations as the wider filter covers more bands.

Chapter 5

Flickering Aurora: Spatial Study

Results presented in this chapter have been published in:
Whiter, D. K., B. S. Lanchester, B. Gustavsson, N. Ivchenko, J. M. Sullivan, and H. Dahlgren, Small-scale structures in flickering aurora, Geophys. Res. Lett., 35, L23103, doi:10.1029/2008GL036134, 2008

This study was carried out entirely by the author, although the analysis, results and scientific interpretation were discussed with colleagues (particularly Betty Lanchester, Björn Gustavsson and Nickolay Ivchenko) throughout the work.

5.1 Introduction

On 22 October 2006 strong flickering was observed in aurora over Tromsø, Norway, with the ASK instrument. This chapter presents results of a study into the spatial properties of the flickering. Temporal and spatial variations of the flickering are interpreted in relation to current theories for the generation of flickering aurora, which are explained in section 2.4 of this thesis.

Previous reports of flickering aurora have almost exclusively concentrated on patches with scale sizes larger than 1 km. This study uses the narrow field of view of the ASK instrument to observe flickering aurora with a spatial resolution of 40 m at 100 km height. There has been only one other study devoted to very small-scale flickering, reported by *Holmes et al.* (2005a) and *Holmes et al.* (2005b). They found scale sizes of flickering patches ranging from 215 m to 1 km.

5.2 Instrumentation

The ASK instrument is described in section 3.1. For this spatial study only the ASK1 camera was used, fitted with the 673.0 nm spectral filter. Due to the relatively wide filter transmission curve the images have a good signal to noise ratio, allowing small structures to be clearly distinguished. At the time of the event studied here the cameras were run at 32 frames per second, allowing for analysis of flickering aurora up to a Nyquist frequency of 16 Hz.

5.3 Analysis

The data used in this study were recorded in a 33 s period between 18:16:20 universal time (UT) and 18:16:53 UT (∼21 magnetic local time (MLT)) on 22 October 2006. The initial 4 s of data exhibit a bright, flickering auroral arc moving into the field of view. The arc has a width of about 1°. Dynamic flickering aurora then fills the field of view.

In the first stage of the analysis each image was binned into 128 × 128 (16,384) equal-sized super-pixels. Part of this binning was performed by the camera hardware during acquisition, as mentioned in the instrumentation chapter. Each super-pixel corresponds to 4 × 4 on-chip detector pixels. The additional post-acquisition binning was carried out in order to reduce noise and computational time required during the analysis. After binning the images have a spatial resolution of approximately 40 m at 100 km height.

A third order polynomial was fitted through the first 32 frames (1 second) of data from each super-pixel, and each fit subtracted from its corresponding data. This procedure removes intensity fluctuations caused by auroral structures moving in and out of the pixel, leaving only the flickering. A Hann window was applied over these residuals, before a fast Fourier transform (FFT) was performed on the sequence. The Hann window was used to reduce edge effects when performing the FFT. This process results in a frequency spectrum with a resolution of 1 Hz. The flickering magnitude was obtained by taking the absolute value of the complex FFT result, producing a quantity referred to as power spectral density (PSD) throughout this thesis. This was done for each super-pixel, so the spatial structure within the flickering can be identified. A 32-frame sliding window was applied in time steps of 1 frame (1/32 s), repeating the analysis at each time step, to facilitate the study of temporal changes in the flickering structure.

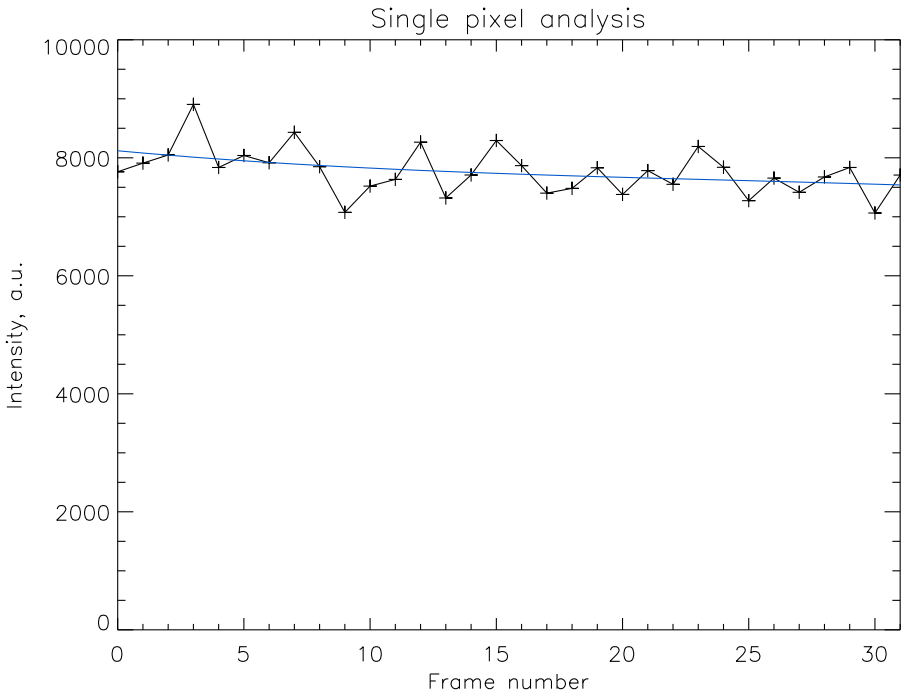

Figure 5.1: A third order polynomial fit through an intensity sequence from a single pixel in a single set of 32 frames.

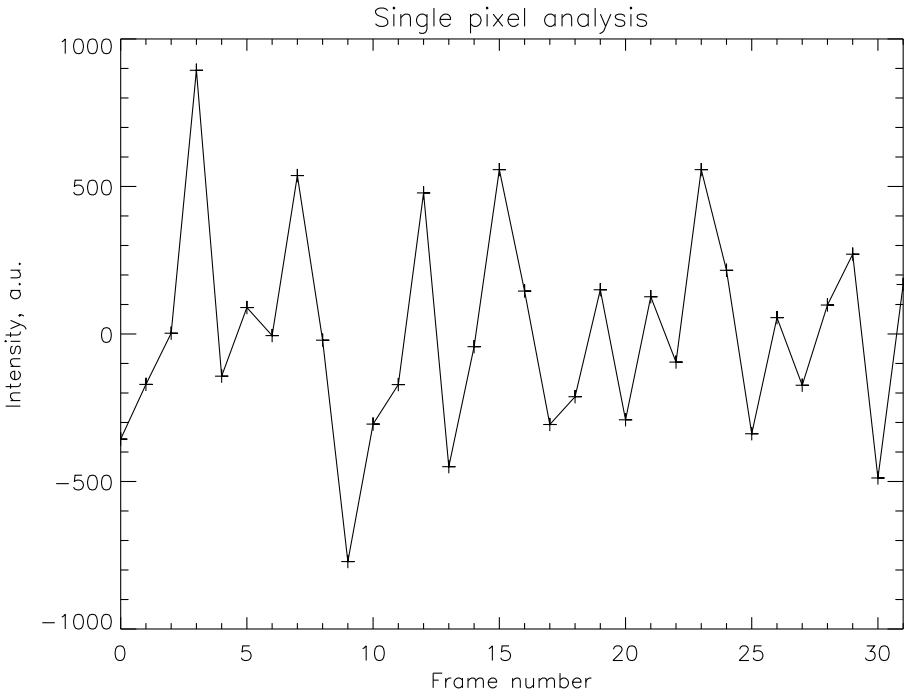

Figure 5.2: The residual flickering component obtained by subtracting the polynomial fit from the sequence.

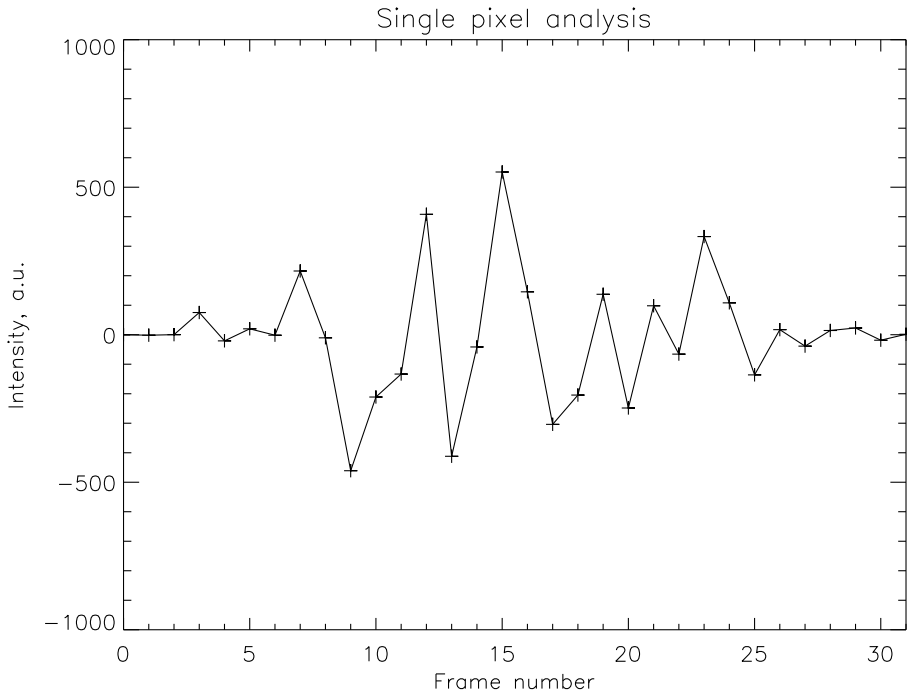

Figure 5.3: Flickering component after applying a Hann window.

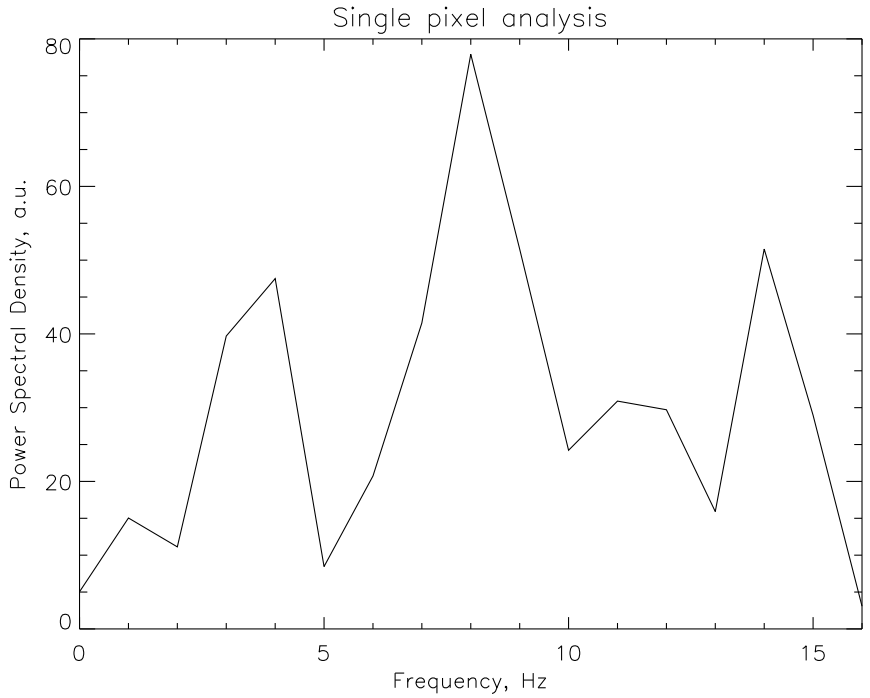

Figure 5.4: Flickering component transformed to frequency domain.

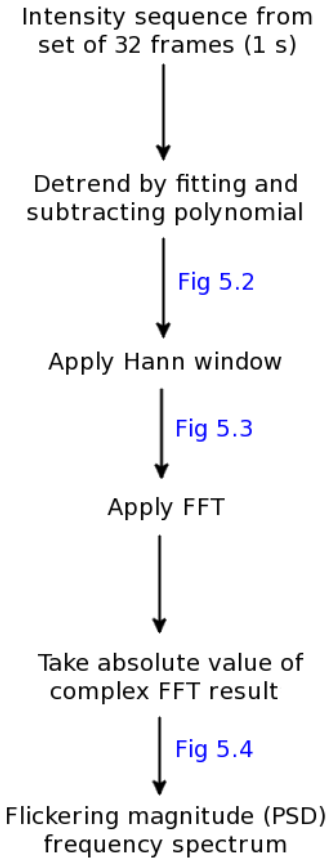

Figure 5.5: A flow chart showing how power spectral density (PSD) is calculated in the analysis presented in chapter 5.

Figures 5.1–5.4 show the analysis process applied to a single pixel in a single set of 32 frames. The initial time sequence of intensities is shown in figure 5.1, with the third order polynomial fit through this sequence shown in blue. Figure 5.2 shows the residual flickering component after the polynomial has been subtracted from the sequence. The result of applying a Hann window is shown in figure 5.3. An FFT is performed on this result to produce a frequency spectrum, shown in figure 5.4. This analysis process is shown on a flow chart in figure 5.5.

The frequency response of the process used to transform from time to frequency domain was tested, and is shown in figure 5.6. To produce this plot a sinusoidal signal with a peak-to-peak amplitude of 2 a.u. and an offset of 10 a.u. was used in place of actual ASK data. The signal had a time resolution of 32 Hz, to match ASK data, and was treated in exactly the same way as real observational data. The peak PSD is shown on the ordinate of figure 5.6. Above 3 Hz the

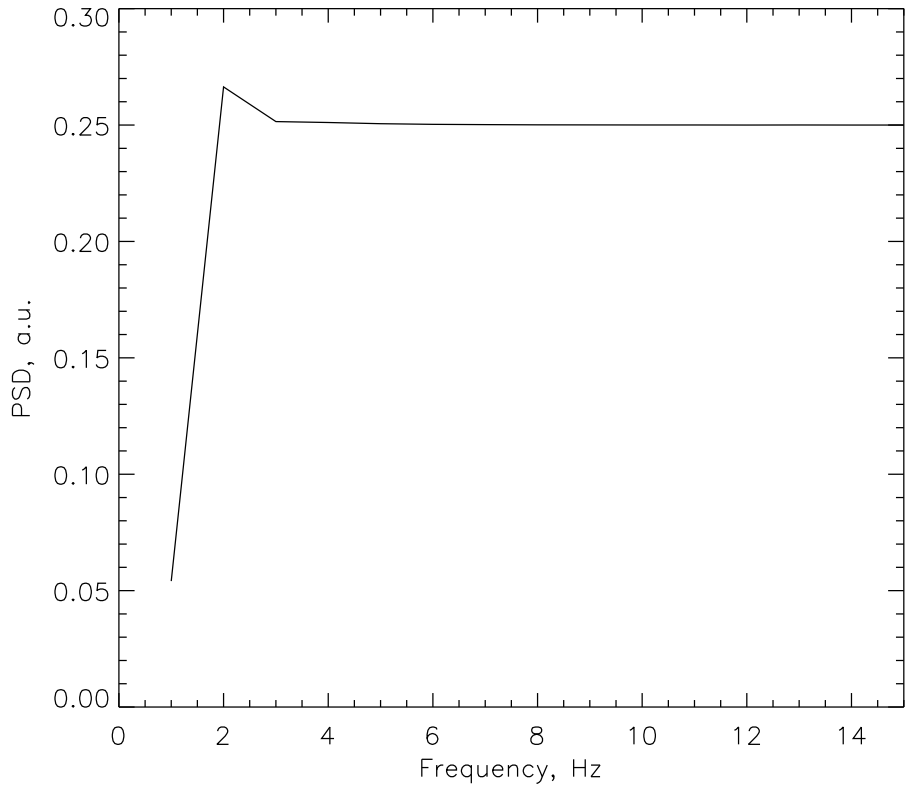

Figure 5.6: The frequency response of the method used to convert from time to frequency domain.

sensitivity of the analysis method is uniform across the entire frequency range.

To test the significance of possible periodic signals (flickering) a simple randomisation simulation was performed on the ASK1 image sequence used in this chapter. A single intensity value was taken from the centre of each image. These values were arranged in random order (rather than chronological order) before performing the process detailed earlier in this section to produce a frequency spectrum. The peak power (peak PSD) was taken from the resulting spectrum. This process was repeated 100,000 times, and the peak powers were sorted into increasing order, allowing a confidence level to be obtained. The 99% confidence level is defined to be the 99,000th largest of the 100,000 peak powers. A plot of confidence level against PSD is shown in figure 5.7. The confidence that a periodic signal detected in actual (chronological) data is flickering aurora, rather than noise, can then be determined using the results of this randomisation simulation. The 99.9% confidence level corresponds to a PSD of 75.

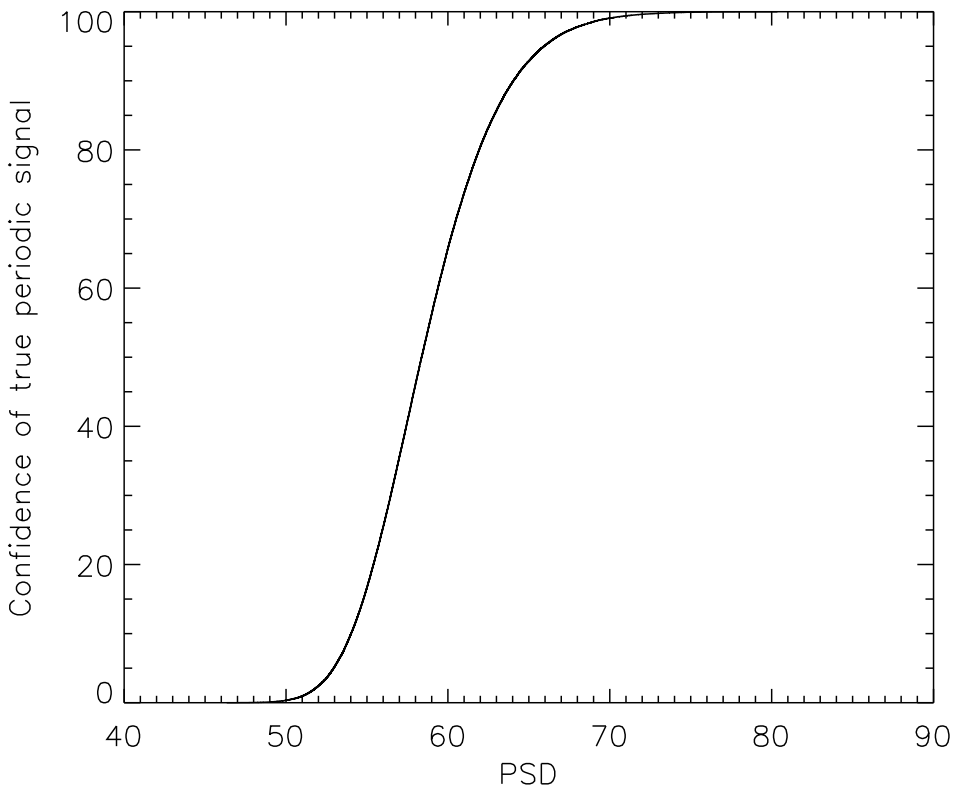

Figure 5.7: Confidence level of periodic signals in results shown in chapter 5, obtained using a randomisation simulation.

In addition to the frequency analysis, mean images were made in order to compare auroral structure with flickering structure. The same 32-frame sliding window was used. For each set of 32 frames the binned camera images were averaged pixel-by-pixel, in order to produce a valid image for comparison with the FFT results.

5.4 Results

The most notable feature of the analysis results is the ubiquitous small scale structure in the intensity of the flickering. Selected results are shown in figures 5.8–5.11. The eight small panels on the right of each figure show the flickering PSD across the whole image in a frequency range of 2 Hz, centred on the frequency indicated beneath the panel. The top-left panel shows the mean auroral image corresponding to the 32 frames used in the frequency analysis. The bottom-left panel highlights the peak flickering frequency for each of the super-pixels in the image.

When the initial auroral arc moves through the field of view the strongest region of flickering at each frequency lies roughly within the region occupied by the main part of the arc, although the flickering region often does not cover the whole arc, and varies in frequency. In figure 5.8, at 18:16:30 UT, 6 s after the front of the main arc has passed, there are small-scale flickering patches with different frequencies which can overlap but are not necessarily co-located. This is typical of the flickering throughout the remainder of the studied event. There are often patches which fill only a small fraction of the instrument field of view. Most have widths smaller than 1 km, and there are many examples where patches as narrow as 4 super-pixels ($\sim$160 m) occur. At most times there are patches and structures which appear and remain in the same location for a few seconds before fading or being replaced by other structures. Some narrow patches move through the field of view. Figure 5.9 shows an example frame where a relatively large patch flickering at $\sim$7 Hz almost fills the instrument field of view. This patch appears to have a width of about 5 km at 100 km altitude. At about 18:16:35 UT the mean auroral brightness decreased significantly. Figure 5.10 shows a time towards the end of the period studied. It can be seen that there is still small-scale flickering structure, despite the aurora having weakened considerably (note the change in brightness scale in the top left panel of the figure). At 18:16:47 UT (figure 5.11)

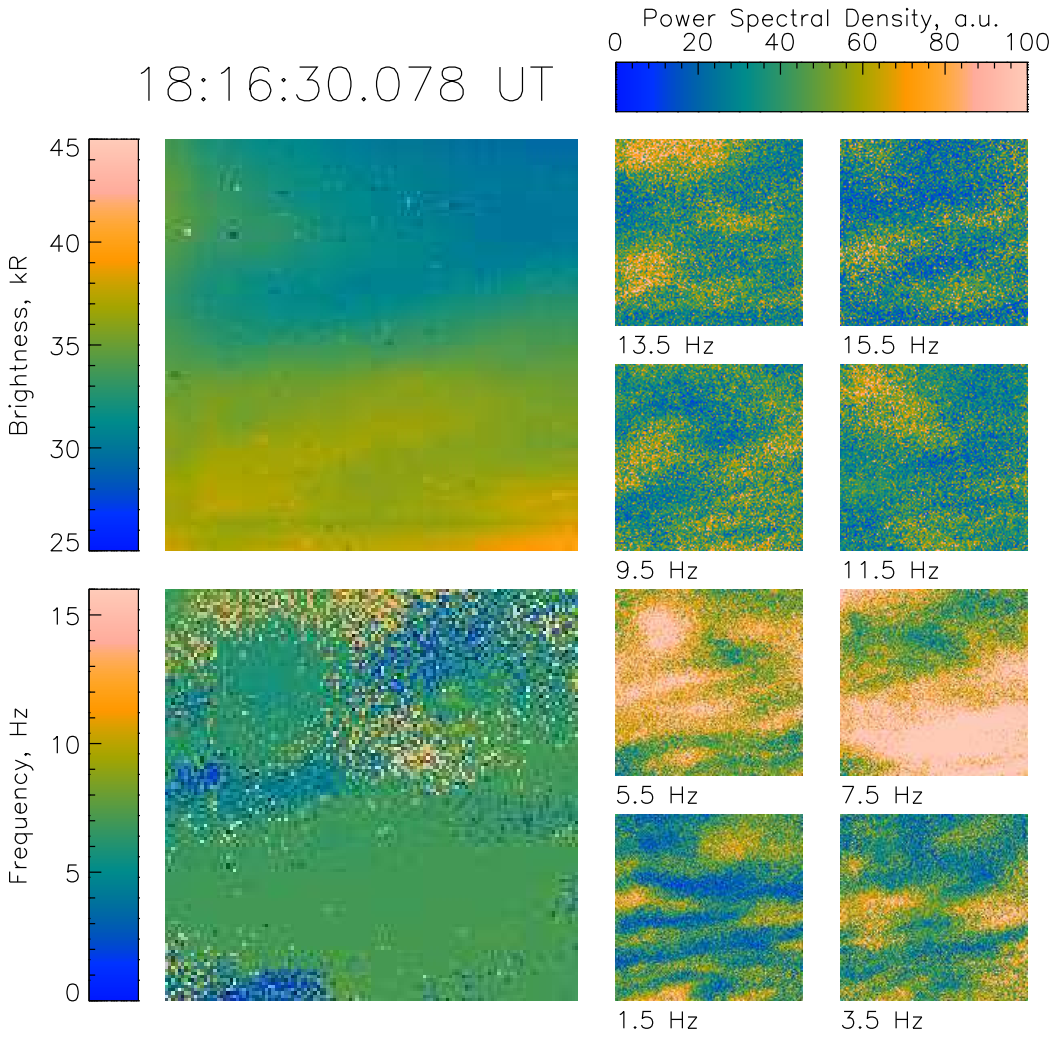

Figure 5.8: Flickering aurora after the arc has moved completely into the field of view. The eight small panels to the right show the power spectral density in the labelled 2 Hz ranges. The top left panel shows the mean image of the 32 frames used in the frequency spectra analysis. The bottom left panel shows the peak flickering frequency for each super-pixel in the image. Each panel has a size of 3.1°× 3.1°, equivalent to approximately 5 km × 5 km at a height of 100 km.

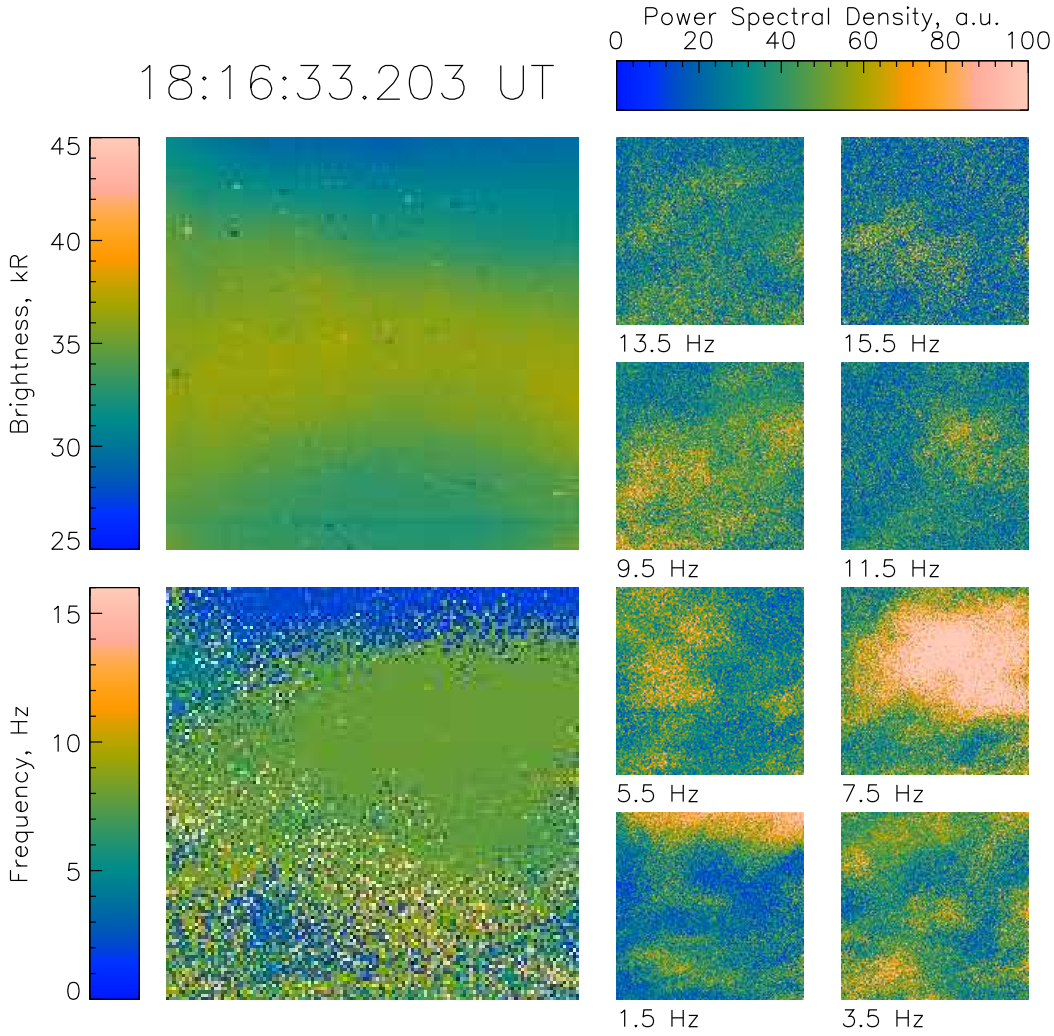

Figure 5.9: Spatial properties of the flickering aurora observed on 22 October 2006, about 10 s after the arc moved into the field of view. The layout of this figure is identical to that of figure 5.8.

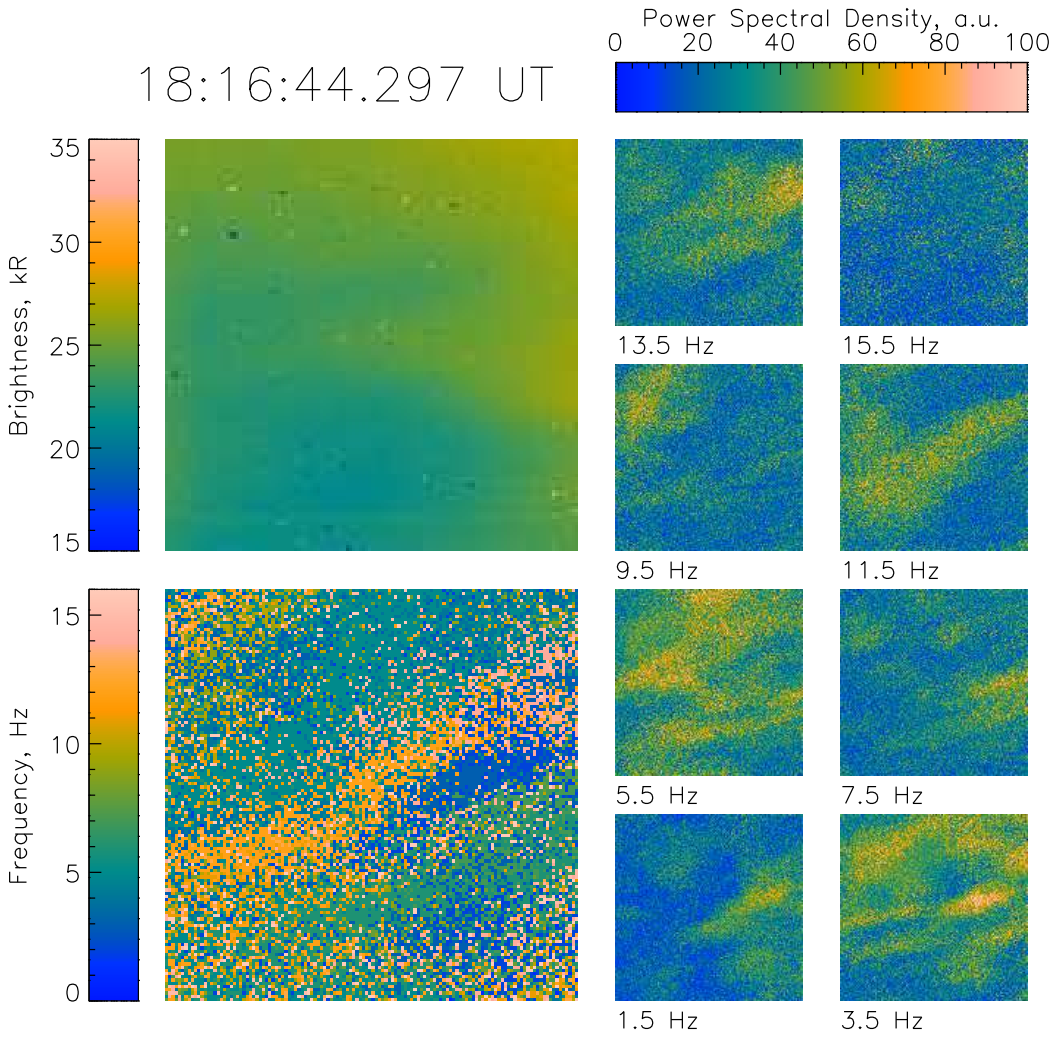

Figure 5.10: Spatial properties of the flickering aurora observed on 22 October 2006, after the aurora has dimmed (note change in brightness scale). The layout of this figure is identical to that of figure 5.8. There are still structures visible in the flickering despite the decrease in mean auroral brightness.

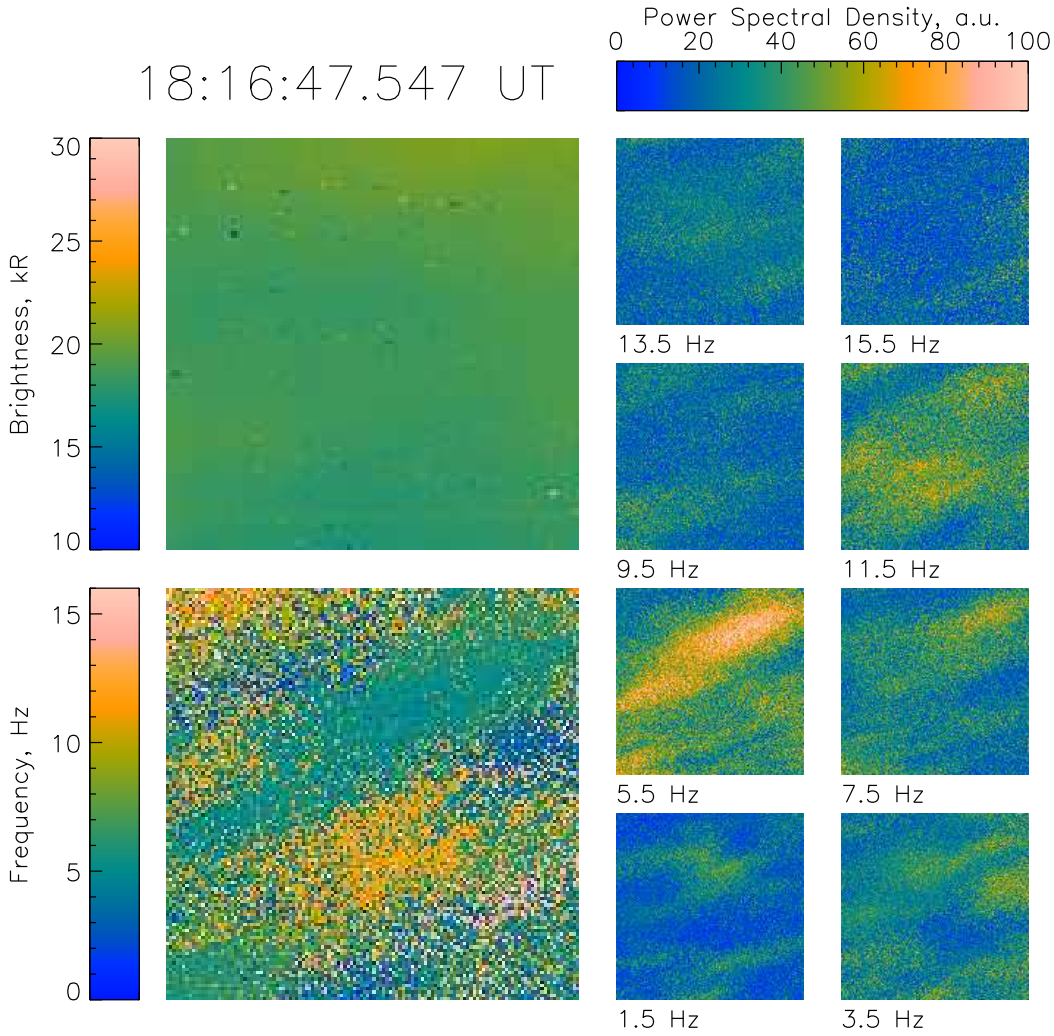

Figure 5.11: Spatial properties of the flickering aurora observed on 22 October 2006, near the end of the period studied. The layout of this figure is identical to that of figure 5.8.

there is a narrow patch of strong flickering aurora with a frequency of about 5.5 Hz, but there are few other flickering patches at this time. A video of the results in the same format as figures 5.8–5.11 was produced. This continuous view of the results leads the eye to the occurrence of elongated narrow structures which are often co-aligned, with major axes roughly parallel to the strong structure shown in figure 5.11. The ratio between width and length of the structures could be related to the difference in propagation angle between two or more interfering dispersive Alfvén waves. Modelling work done by *Gustavsson et al.* (2008) has shown that it is possible to produce many different structures by varying the parameters of multiple interfering EMIC waves.

The dominant frequency of the flickering is between 6–8 Hz for a substantial portion of the 33 s interval. However, it is clear from the small panels in figures 5.8–5.11 and the peak frequency in the bottom left panel that other frequencies dominate in small structures at other times. For example in figure 5.10 the dominant frequencies of a distinct feature across the image are in the 11–12 Hz range. Usually structures partially overlap across a frequency range of a few Hz.

In order to study the spatial and temporal nature of flickering aurora, and its relationship to the steady auroral intensity, the mean images have been compared with the PSD of the flickering. The bottom panel in figure 5.12 addresses the temporal relationship between flickering aurora and the background steady aurora. The solid grey line shows the mean flickering PSD across all frequencies, obtained by averaging over all super-pixels. It is likely that the large peak at 18:16:24 UT is caused by the transient intensity increase resulting from the auroral arc moving into the field of view. The black line shows the mean brightness of the 32-frame mean images. This is equivalent to a 1 s running mean auroral brightness. This panel shows that when there is increased auroral activity there is also increased flickering activity. As there is aurora filling the field of view for all but the initial part of the sequence, this high correlation cannot be caused by changes in auroral coverage. Therefore there is a temporal correlation between flickering strength and auroral brightness.

To address the spatial relationship between flickering aurora and the background steady aurora the mean images have been correlated spatially with the PSD of the flickering. The top panel of figure 5.12 shows the time-varying correlation coefficient for three 2-Hz-wide frequency ranges and also for all frequencies (thick black line). The correlation coefficient is obtained for each mean image individually. Each super-pixel is treated as a separate data point, and the image

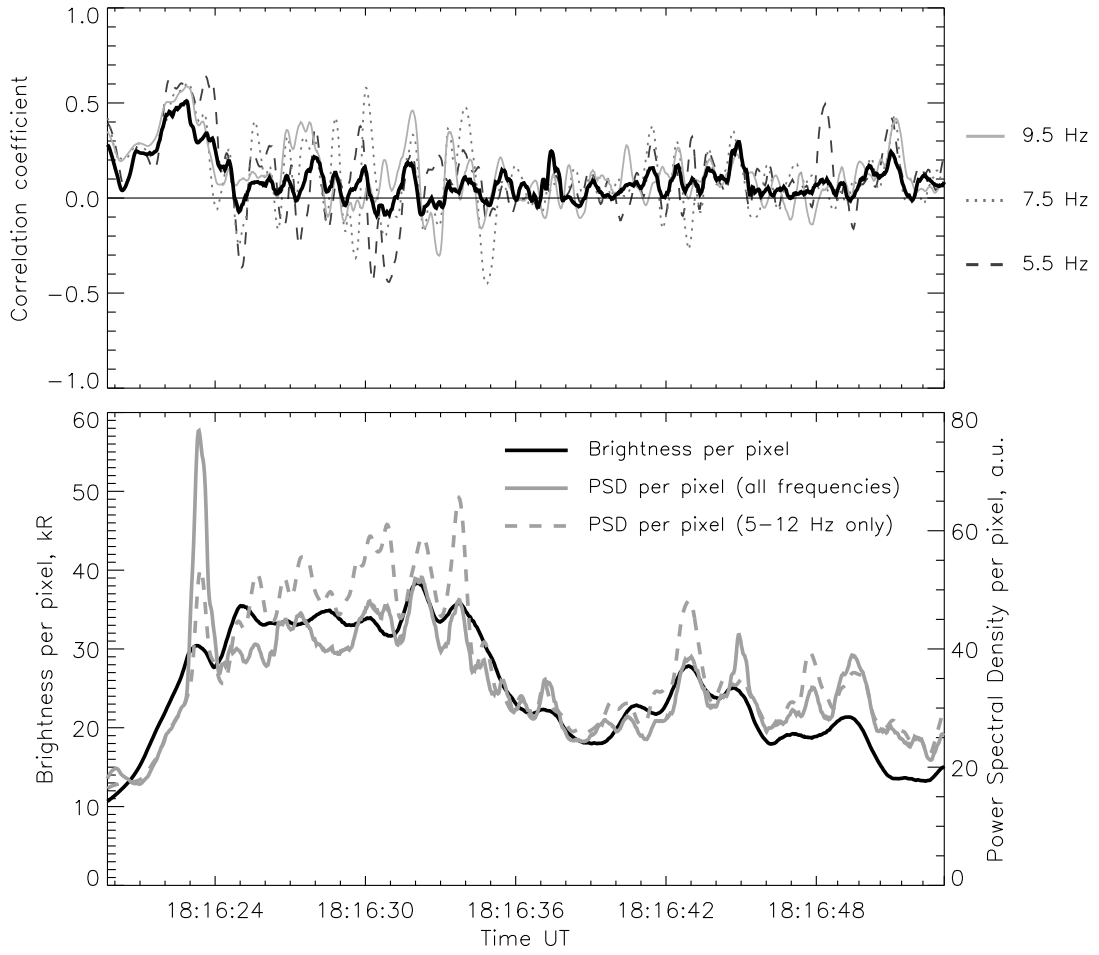

Figure 5.12: Spatial and temporal correlation between flickering and non-flickering aurora. The top panel shows the time-varying spatial correlation coefficient between flickering power spectral density and auroral brightness, in three 2-Hz ranges and across all frequencies (thick black line). The bottom panel shows the mean PSD over all frequencies (grey solid line) and in the range 5–12 Hz (grey dashed line), together with the 1-s running mean auroral brightness (black line), all averaged over the whole image.

brightness is correlated with the flickering power at the frequencies within the specific range. It can be seen that the correlation is generally low. There are times where the correlation coefficient is considerably positive (or negative) at specific frequencies, but this is simply the result of the flickering matching with the brighter (or less bright) auroral features at those times. This correlation has been tested for each frequency, including those not plotted in figure 5.12. The mean correlation coefficient over the whole 33 s period for all frequencies (thick black line) is only 0.094. This is also biased by the relatively high correlation coinciding with the period in which the arc is moving into the field of view (first 4 seconds). The mean correlation coefficient for the last 28 seconds of the period (where aurora is filling the field of view) is 0.064. Therefore on small scales the flickering is not necessarily stronger where there is brighter aurora, i.e. there is no spatial correlation. The combined result of the correlations shown in figure 5.12 is that flickering is linked temporally to auroral activity, but not spatially on small-scales.

5.5 Conclusions

This work has shown that the intensity of flickering in aurora has small-scale structure on sub-km scales. To the author's knowledge there has been only one other analysis of flickering patches on such small scales, reported by *Holmes et al.* (2005a) and *Holmes et al.* (2005b). The ASK observations agree closely with these reports. The work presented here has produced evidence to suggest that the source of flickering and the source of the general aurora are linked, as flickering strength and auroral activity correlate temporally. However, on small scales the two are not linked spatially. These results are consistent with the theories of *Sakanoi et al.* (2005), that small-scale structure in flickering is a result of interference between two or more dispersive Alfvén waves, modulating the auroral intensity. According to this theory the spatial structure seen within the flickering of the aurora is an interference pattern, which is not necessarily affected by or linked to mechanisms producing fine-scale structures in non-flickering aurora, or the non-flickering component of flickering aurora. In order to explain the lack of spatial correlation using the oscillating inverted-V theory of *Arnoldy et al.* (1999) it would be necessary to assume that the auroral brightness is strongly dependent on small-scale non-flickering structures which are not related to the

oscillating inverted-V potential. This seems unlikely. Also it is difficult to explain the small-scale structure seen in the flickering PSD using this theory, since inverted-V auroral structures are usually of greater horizontal widths than the sub-km sizes described here.

Chapter 6

Flickering Aurora: Spectral Study

Results presented in this chapter have been published in:
Whiter, D. K., B. S. Lanchester, B. Gustavsson, N. Ivchenko, and H. Dahlgren, Using multispectral optical observations to identify the acceleration mechanism responsible for flickering aurora, J. Geophys. Res., 115, A12315, doi: 10.1029/2010JA015805, 2010

This study was carried out entirely by the author, although the analysis, results and scientific interpretation were discussed with colleagues (particularly Björn Gustavsson, Betty Lanchester and Nickolay Ivchenko) throughout the work.

6.1 Introduction

This chapter presents a temporal and spectral analysis of flickering aurora using ASK data. By observing different auroral emissions simultaneously it has been possible to estimate the energies of precipitating electrons responsible for flickering aurora. A major part of this work concentrates on the analysis of flickering auroral "chirps". These are short (approximately 1–2 s) intervals where the frequency of flickering ascends or descends significantly. There have been no previous reports on the analysis of such features, although they have been observed by *Gustavsson et al.* (2008). In this chapter current theories for the generation of flickering aurora have been evaluated in the light of the results, leading to the conclusions that electron acceleration is limited by the EMIC wave parallel phase velocity.

6.2 Instrumentation

The ASK cameras and photometers have been used in this study, and were operated at 32 Hz and 96 Hz respectively during acquisition. The time resolution of the photometer data has been reduced to 32 Hz by summing over sets of three consecutive data points, thus reducing noise and giving the same resolution for photometer and camera data. This resolution allows for analysis of flickering aurora up to a Nyquist frequency of 16 Hz. Spectra were created for full-resolution photometer data (96 Hz), allowing flickering up to a frequency of 48 Hz to be identified. No significant oscillations were found at frequencies above those observed by the ASK cameras. The imaging part of the camera EMCCDs have 512 × 512 pixels, which were binned equally into 256 × 256 pixels during the acquisition of the data.

6.3 Observations

A detailed study has been made of four chirps which have been identified within two flickering auroral events. Three of the four chirps occurred on 22 October 2006 during the same event as studied in chapter 5. A shorter event on 12 December 2006 provided the fourth chirp. Both events occurred pre-midnight, at ∼21 MLT and ∼22 MLT respectively. So far 95 s of flickering aurora has been found in ASK data, all during the two events studied here. All identified chirps are included in this work and cover about 7% of the total flickering time. On 22 October 2006 ASK1 was fitted with the 673.0 nm spectral filter, whereas on 12 December 2006 ASK1 was fitted with the 562.0 nm spectral filter. The data have been analysed in the same way for all chirps.

Figures 6.1–6.4 show time series of flickering emission brightnesses (top panels) together with power spectra (middle and bottom panels) obtained from images in I_{6730} or I_{5620} (ASK1) and I_{7774} (ASK3) for each of the four chirps. The chirps are clearly visible in the frequency spectra, as a steady change in flickering frequency over a short period of time. The first and fourth chirps are "down" chirps, where the frequency decreases over time. The second and third chirps are "up" chirps. The duration of all chirps is 1–2 s, with frequency changes of about 2–6 Hz over this time period. The mean auroral brightness and signal to noise (S/N) ratio of the first chirp is 34 kR and 543 respectively in I_{6730}, and 6.5 kR and 93 respectively in I_{7774}. The second and third chirps both have mean auroral brightnesses and

S/N ratios of approximately 20 kR and 200 respectively in I_{6730} and 3.5 kR and 35 in I_{7774}. The fourth chirp displays the weakest aurora and flickering, with mean auroral brightnesses and S/N ratios of 320 R and 6 respectively in I_{5620} and 1.6 kR and 14 respectively in I_{7774}. The peak-to-trough flickering amplitude varies, but is typically 10-20% of the mean auroral brightness during all chirps.

During winter 2006/2007 the ASK instrument was located 400 m from the EISCAT UHF radar dish in Norway. The main beam of the radar was field-aligned during these observations, co-aligned with ASK. The radar data for the 22 October 2006 event are shown in figure 6.5 as power profiles, which are a measure of electron concentration obtained by scaling the total returned radar power (see section 3.3). The time resolution of these data is 0.44 s. During the flickering (between 18:16:20 UT and 18:17:30 UT) the electron concentration enhancement extended below the lowest altitude probed by the EISCAT radar, which for the experiment program in operation ("arc1") is 92 km when field-aligned. The fact that the electron concentration peak was at or below this height indicates that the electron energy peak was above about 12 keV (*Rees*, 1989). The shape of the profiles in electron concentration suggest a high-energy monoenergetic (Gaussian) spectrum of electron precipitation, rather than a Maxwellian spectrum which would produce more ionisation at higher altitudes.

6.4 Analysis

6.4.1 ASK camera data

In this study only the temporal variation of the aurora has been considered, not the spatial variation. A digital circular "mask" with a radius of 16 pixels (0.2°) was applied over the centre of the camera images, and the mean number of counts recorded per pixel within this circular mask was calculated at each time step. From the camera images it is known that the aurora fills the field of view at all of the times studied here.

The process to transform from time to frequency domain is nearly identical to that performed for the analysis in chapter 5. The main difference is that in this study there is only one intensity value for each frame, as opposed to the many pixels used in the other spatial and temporal analysis. In addition a noise subtraction process has been carried out in order to compare more accurately the data from different cameras and emissions. This is accomplished by perform-

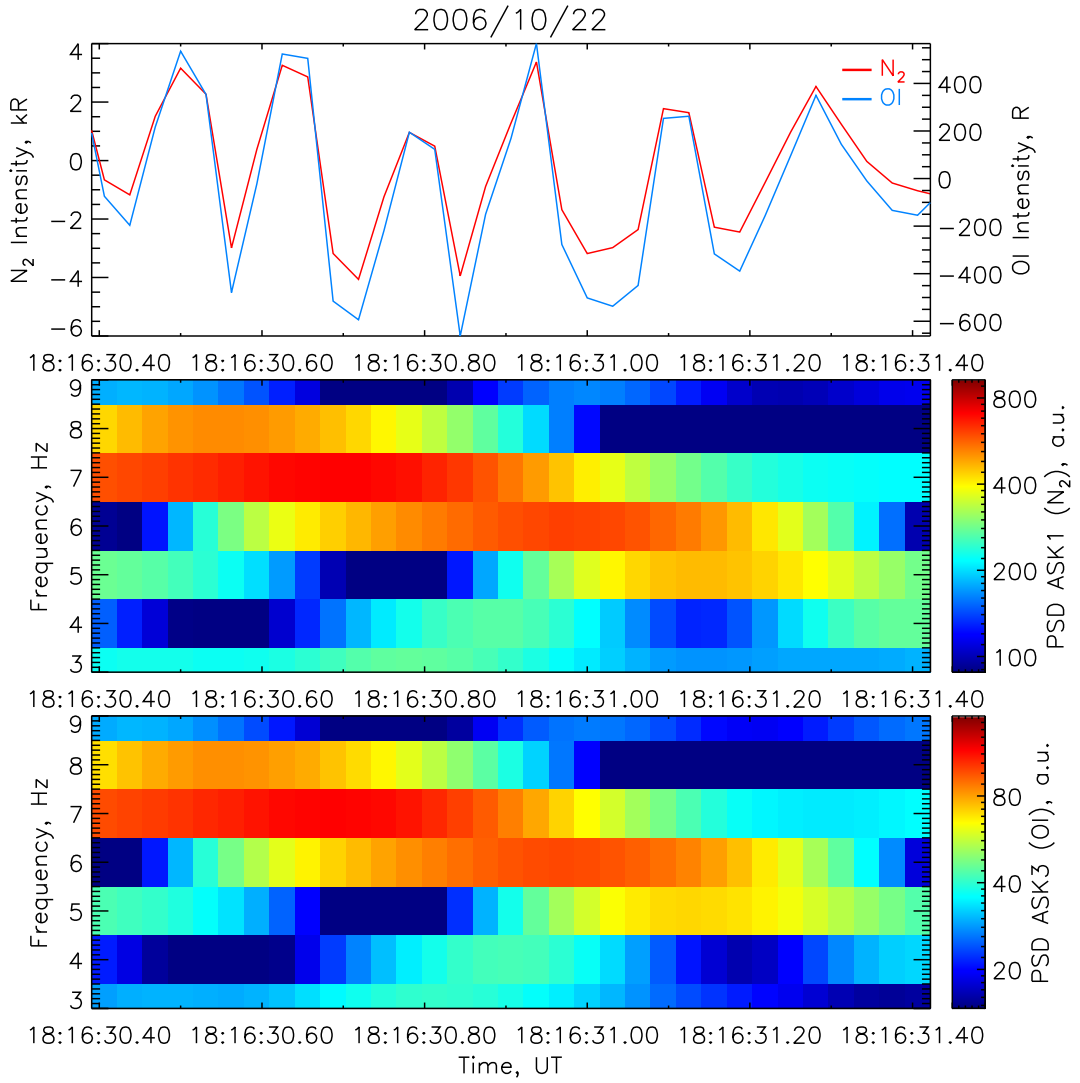

Figure 6.1: Chirp 1. The top panel shows the detrended intensity time series for the ASK1 (N_2) and ASK3 (OI) cameras. The second and third panels show the power spectra obtained from these time series for ASK1 and ASK3 respectively.

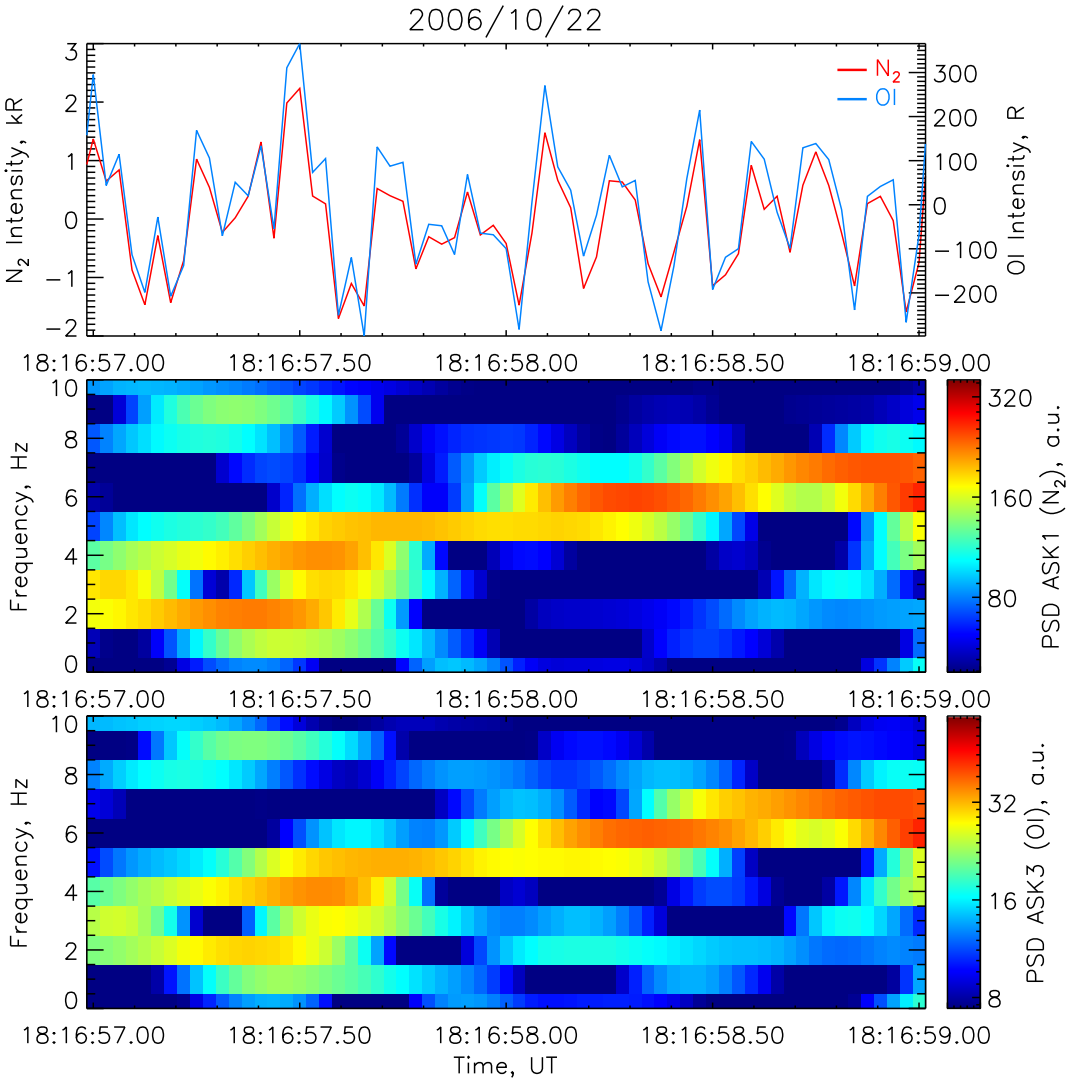

Figure 6.2: Chirp 2. The top panel shows the detrended intensity time series for the ASK1 (N_2) and ASK3 (OI) cameras. The second and third panels show the power spectra obtained from these time series for ASK1 and ASK3 respectively.

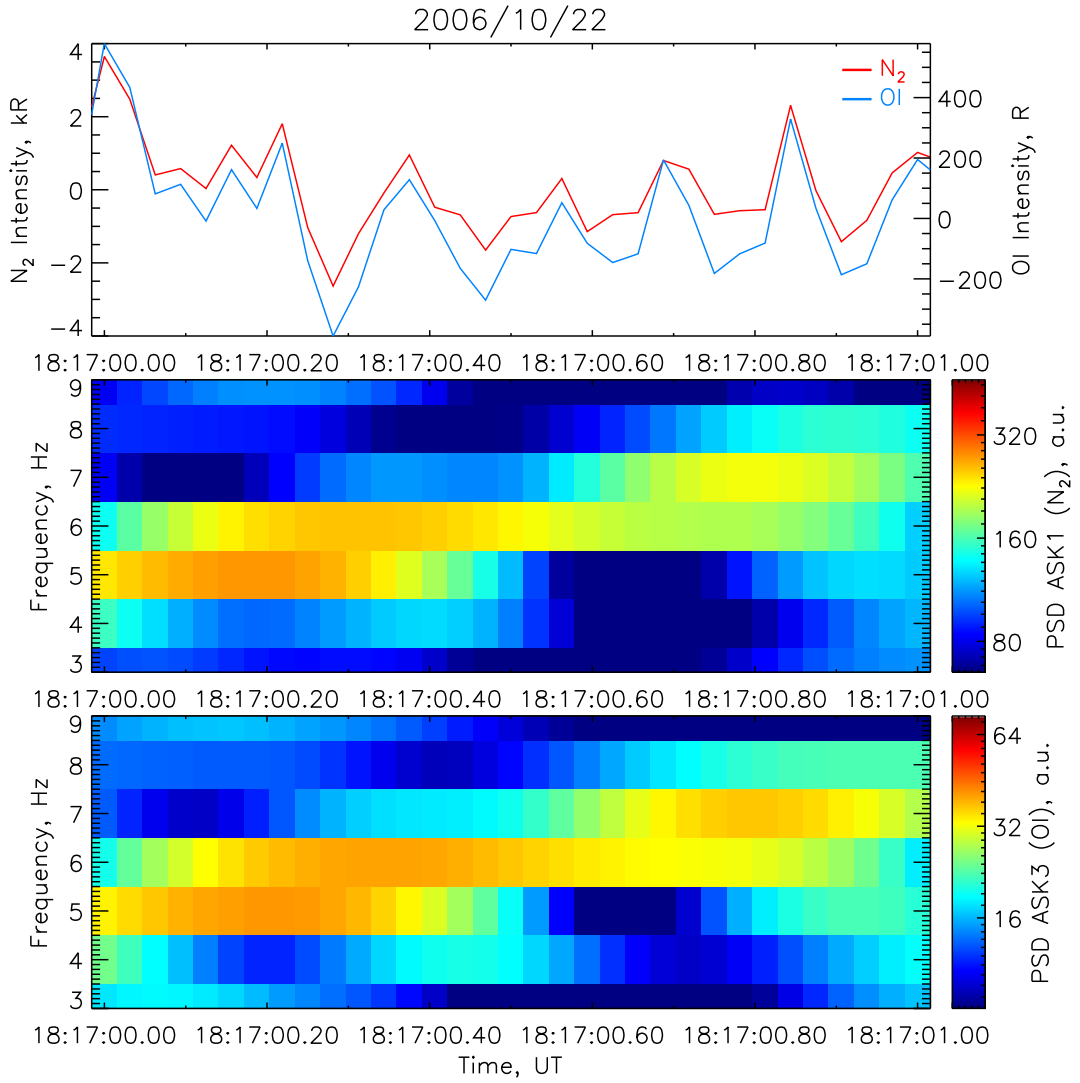

Figure 6.3: Chirp 3. The top panel shows the detrended intensity time series for the ASK1 (N_2) and ASK3 (OI) cameras. The second and third panels show the power spectra obtained from these time series for ASK1 and ASK3 respectively.

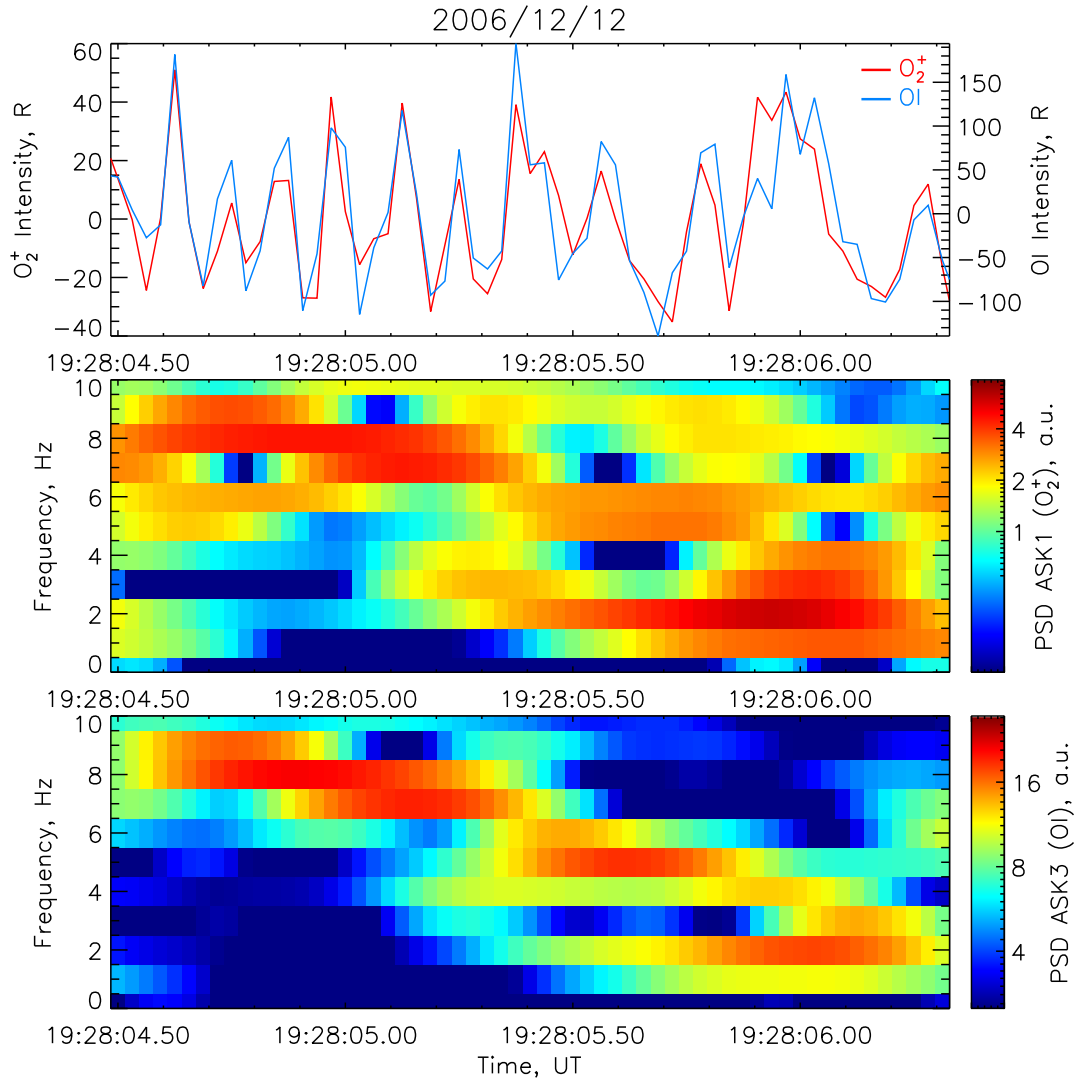

Figure 6.4: Chirp 4. The top panel shows the detrended intensity time series for the ASK1 (O_2^+) and ASK3 (OI) cameras. The second and third panels show the power spectra obtained from these time series for ASK1 and ASK3 respectively.

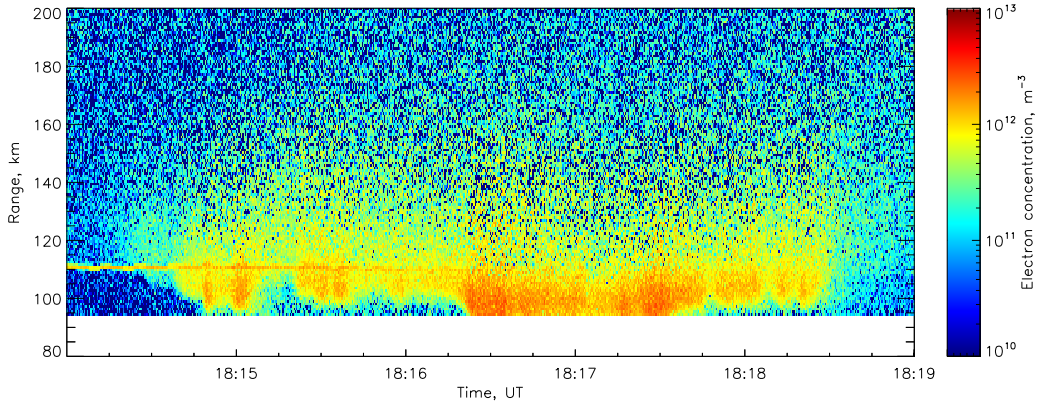

Figure 6.5: EISCAT power profiles from 22 October 2006. The flickering aurora was observed during the time of increased electron concentration at the lowest height gates, between 18:16:25 UT–18:17:25 UT.

ing an identical analysis on the image sequence used to produce the image for background subtraction. As this is a clear period with no cloud or aurora the resulting frequency spectrum is instrument dependent. As expected, this spectrum is white noise, but the overall magnitude is different for different cameras and filter combinations. As an example the noise spectra for the ASK cameras on 12 December 2006 are shown in figure 6.6. The only other difference from the process performed in chapter 5 is that a digital filter is applied to the intensity sequence to remove the effects of non-flickering aurora, instead of detrending the sequence by fitting and subtracting a third order polynomial to each set of 32 frames. Here a 1 Hz low-pass filter is applied, which is then subtracted from the sequence. Little difference is seen in the resulting frequency spectra, but the filtering method is more robust and flexible than using a third order polynomial fit.

As for the earlier analysis presented in chapter 5, the frequency response of the process used to transform from time to frequency domain was tested, and is shown in figure 6.7. This plot was produced in an identical way to figure 5.6, except that the analysis method explained in this section was used. Above 3 Hz the sensitivity of the analysis method is uniform across the entire frequency range, and there is only a slight increase in sensitivity between 2 Hz and 3 Hz.

To compare the frequency of flickering with the PSD ratio between different emissions a method to calculate a "peak frequency" and equivalent parameter for PSD ratio has been developed. This reduces the influence of noise in the flickering spectra. At each time step a weighting factor, $W(f)$, has been calculated for each

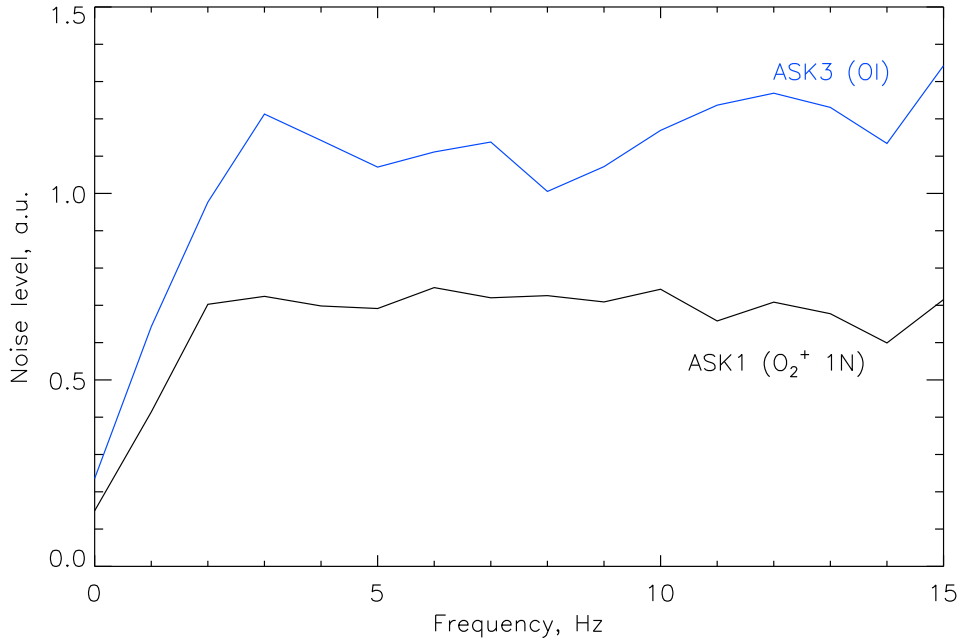

Figure 6.6: Noise spectra for the ASK1 (black) and ASK3 (blue) cameras on 12 December 2006.

frequency.

$$W(f) = \frac{\omega(f)}{\sum_{\forall f} \omega(f)} \tag{6.1}$$

where

$$\omega(f) = \exp\left(\frac{P(f)^2}{\text{mean}(P(f)^2)}\right)$$

and $P(f)$ is the PSD at frequency f.

The "peak frequency" used throughout this study is then defined as

$$f_{\text{peak}} = \sum_{\forall f} f.W(f) \tag{6.2}$$

This weighting method gives sufficient dominance to frequencies with large PSDs. Frequencies with no significant flickering power have a negligible effect on the peak frequency. In addition the weighting is restricted to the frequency range containing the chirps, as used on the ordinate scale in the lower two panels of figures 6.1–6.4.

The same weighting factors are used to calculate a single PSD ratio value at each time,

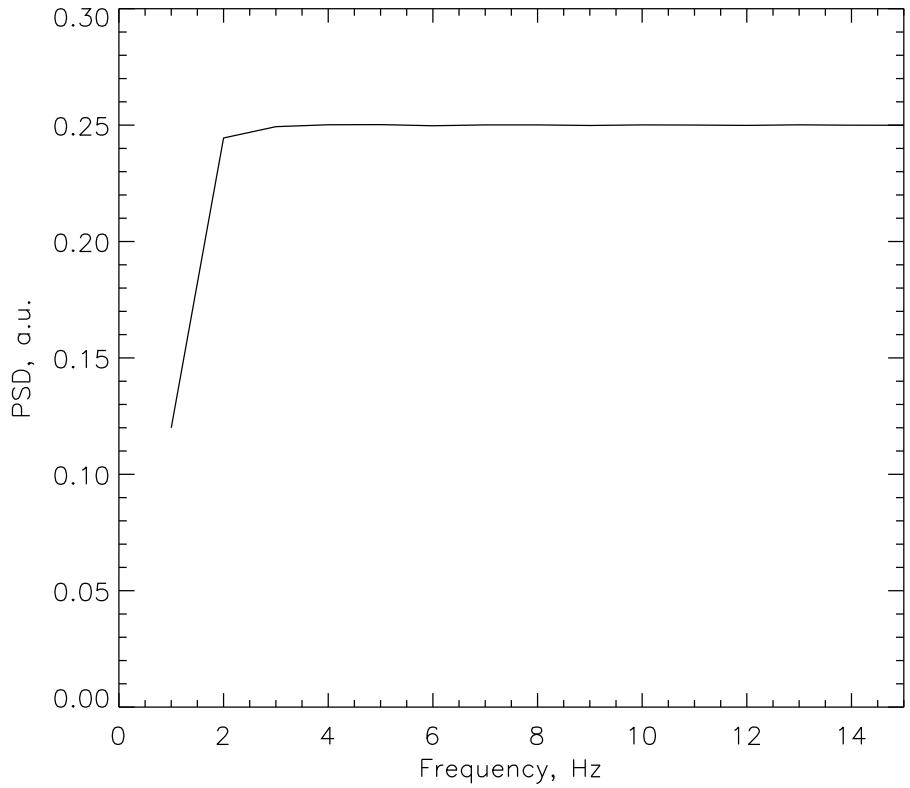

Figure 6.7: The frequency response of the method used to convert from time to frequency domain in the analysis of chirps.

$$R_{\text{peak}} = \sum_{\forall f} R(f).W(f) \tag{6.3}$$

where $R(f)$ is the ratio of PSDs between the emissions at I_{7774} (ASK3) and I_{6730} or I_{5620} (ASK1) at a given frequency, f. This quantity is hereafter referred to as the "peak ratio". The $P(f)$ used in the calculation of $W(f)$ is the sum of the PSDs observed in the two cameras. As the same weighting process is applied, the peak frequency and peak ratio values can be directly compared. The PSD ratio has been constrained to lie in the range 0.01–1000. Occasionally extreme ratios are calculated when the PSD at a particular frequency is exceptionally small or negative (at or below the calculated noise level). These values are discarded from the analysis.

6.4.2 Ionospheric modelling

Using the Southampton Ionospheric Model the ratio between I_{7774} (ASK3) and I_{6730} or I_{5620} (ASK1) can be directly related to the energy of auroral electron precipitation, as explained in chapter 4. This applies equally to PSD ratios, which have an identical relationship to precipitation energy, assuming the flickering aurora can be treated as an additional electron flux.

It is important to consider the effects of velocity dispersion when studying flickering aurora. Electrons which are simultaneously accelerated to different velocities (energies) will reach the auroral altitudes in the ionosphere at different times. When the difference in electron arrival times is comparable to the oscillation period velocity dispersion can cause peaks in auroral emission to smear significantly, reducing the apparent flickering amplitude. *Peticolas and Lummerzheim* (2000) carried out time-dependent electron transport modelling of this effect, showing that due to velocity dispersion flickering amplitudes decreased for high frequencies. Velocity dispersion can also introduce a phase difference between different emissions which are sensitive to different electron energies (velocities). A simple simulation has been carried out to correct for velocity dispersion in the modelling analysis, based on the observed phase difference between ASK emissions. This is done for each time step and frequency individually. The simulation, though more simple than that carried out by *Peticolas and Lummerzheim* (2000), is sufficient for this work.

In the velocity dispersion simulation the modelled emission brightness curves

shown in the top panel of figure 4.4 are convolved with a Gaussian of specific peak energy and width to estimate emission from a single instantaneous burst of electrons with such a Gaussian energy distribution. The energy axis is then converted to a time axis by considering the flight time of electrons travelling at constant velocity from an altitude of 1 R_E, resulting in a time sequence of emission brightnesses caused by the instantaneous burst of electrons. A representation of flickering aurora is then built up by adding together emission time sequences from consecutive instantaneous electron bursts of varying total flux. The total flux is modulated by a $\sin^2$ function to simulate flickering aurora at a specific frequency. The predicted phase difference and PSD ratio between the different emissions is calculated by applying the same process to the simulated flickering aurora as is applied to the ASK data. A simple flow diagram demonstrating the velocity dispersion simulation process is shown in figure 6.8.

Figure 6.9 shows the predicted phase difference (top panel) and PSD ratio (bottom panel) between the I_{7774} and I_{6730} emissions as a function of peak energy and width of the Gaussian used in the simulation. The total electron flux is modulated at 7 Hz. It is found that for wide simulated energy distributions the phase difference between I_{6730} (or I_{5620}) and I_{7774} can be as high as 15–20° for 7 Hz flickering. For narrow energy distributions the predicted phase difference is only a few degrees. The phase difference between the flickering observed in I_{6730} (or I_{5620}) and I_{7774} was found to be small throughout the events, typically 0–5° on 22 October 2006 and 0–7° on 12 December 2006. The PSD ratio has only a slight dependence on the width of the Gaussian, showing that the correction derived from the velocity dispersion simulation has only a slight effect on the electron precipitation energies derived from the observed PSD ratio between ASK emissions.

6.5 Results

The flickering proportion of the total brightness was found to vary between the different emissions. Power spectra were computed for the cameras and photometers which were subsequently normalised to the mean of the data used in the FFT analysis. The resulting normalised PSD is a measure of the fraction of the total auroral brightness which is flickering. Comparison can then be made between the camera data and the photometer data, which could not be absolute

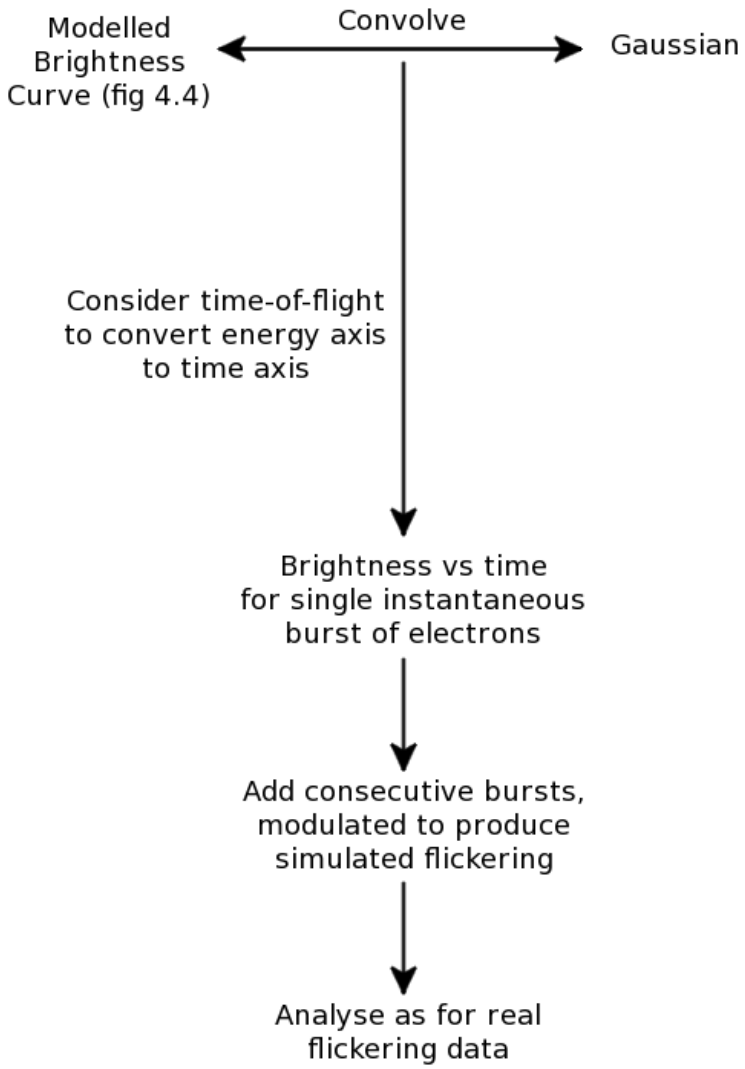

Figure 6.8: A flow diagram demonstrating the velocity dispersion simulation process.

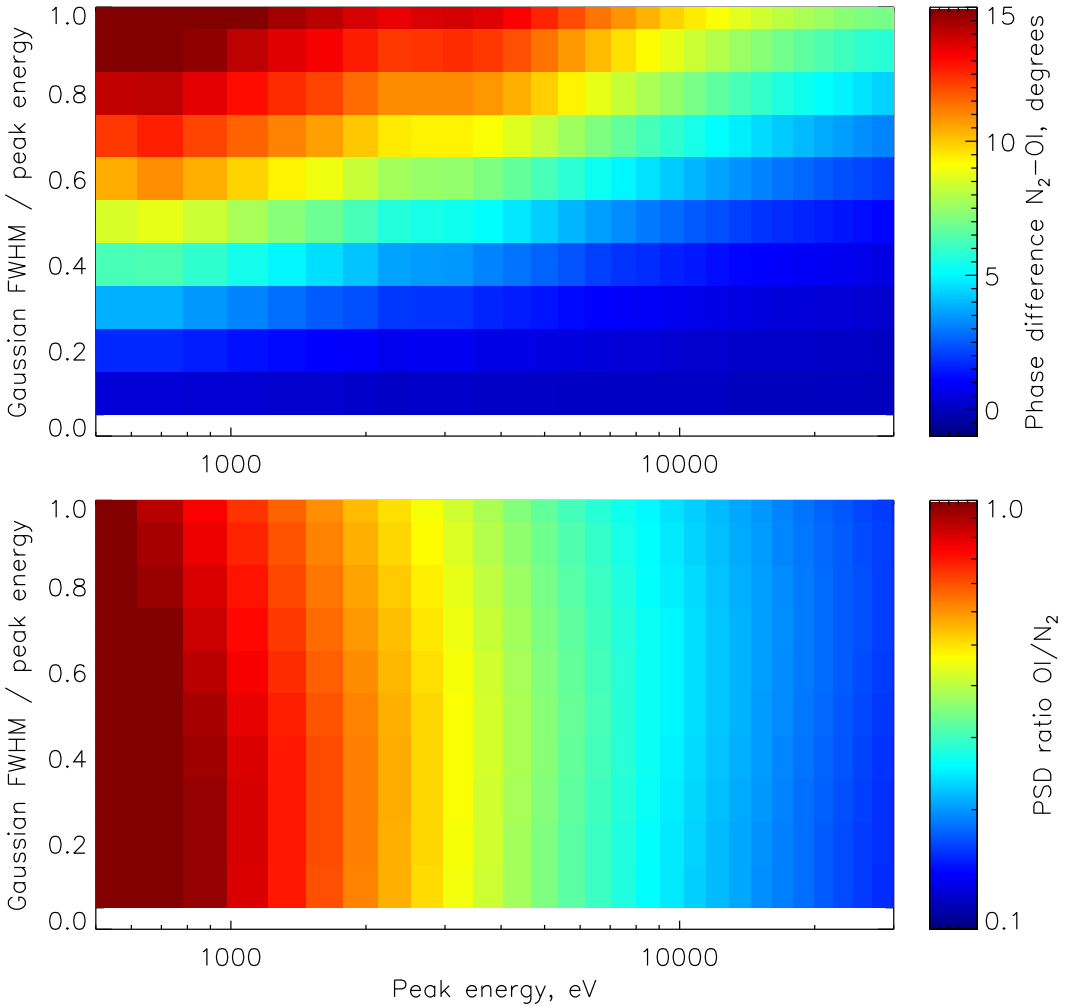

Figure 6.9: Modelled effect of velocity dispersion on phase difference (top) and PSD ratio (bottom) between ASK emissions.

intensity calibrated. Figure 6.10 shows these normalised spectra for part of the 22 October 2006 event, from both cameras and photometers. The ratio between the normalised PSD calculated for any two of the emissions is not generally unity, even after velocity dispersion effects have been removed.

To produce flickering auroral emission, the auroral electron flux must be changing periodically in some way. The two parameters which can change are the total energy flux and the energy distribution of the flux. Periodicity in either parameter would create periodicity in a specific auroral emission. As different fractions of the total emission are flickering for different emissions the mean energy of the electron flux must be oscillating. As shown in figure 4.4 the two ASK camera emissions have opposite dependencies on the precipitation energy; I_{6730} and I_{5620} increase with increasing energy, whereas I_{7774} decreases with increasing energy. If the total flux was constant while the mean energy oscillated periodically, the flickering seen with the two cameras would be in anti-phase. However, the emissions are flickering approximately in phase with one another. Therefore the total flux must be oscillating, and must be the dominant oscillation.

Generally the 673.0 nm emission displays the largest fraction of flickering, followed by the 470.9 nm emission and then the 777.4 nm emission. The 844.6 nm emission typically displays the weakest flickering. For the 12 December 2006 event the 562.0 nm emission has a larger fraction of flickering than the 777.4 nm emission (no photometer data were available for this event). It is therefore inferred that during flickering peaks the mean energy of the precipitating electron distribution is higher than during flickering troughs, and the oscillations in mean energy are in phase with the oscillations in total precipitating energy flux.

From the OI/N_2 ratio the peak energy of electron precipitation responsible for the background non-flickering aurora was estimated to be 11–15 keV throughout the flickering event on 22 October 2006, with a mean value corresponding to 13 keV. This is in good agreement with the energies estimated from the EISCAT data. Assuming that the flickering aurora is caused by an additional oscillating electron flux, the PSD ratio can provide an estimate of the energy of this additional flux. The peak PSD ratio for the 22 October 2006 event corresponds to energies of about 12–40 keV. The mean peak energy for the period is 22 keV, suggesting that although the non-flickering aurora was high-energy, the flickering precipitation was at substantially higher energies. For the 12 December 2006 event the non-flickering electron precipitation peaked at energies of 8–13 keV, with a mean of 10 keV, while the flickering precipitation peaked at energies of

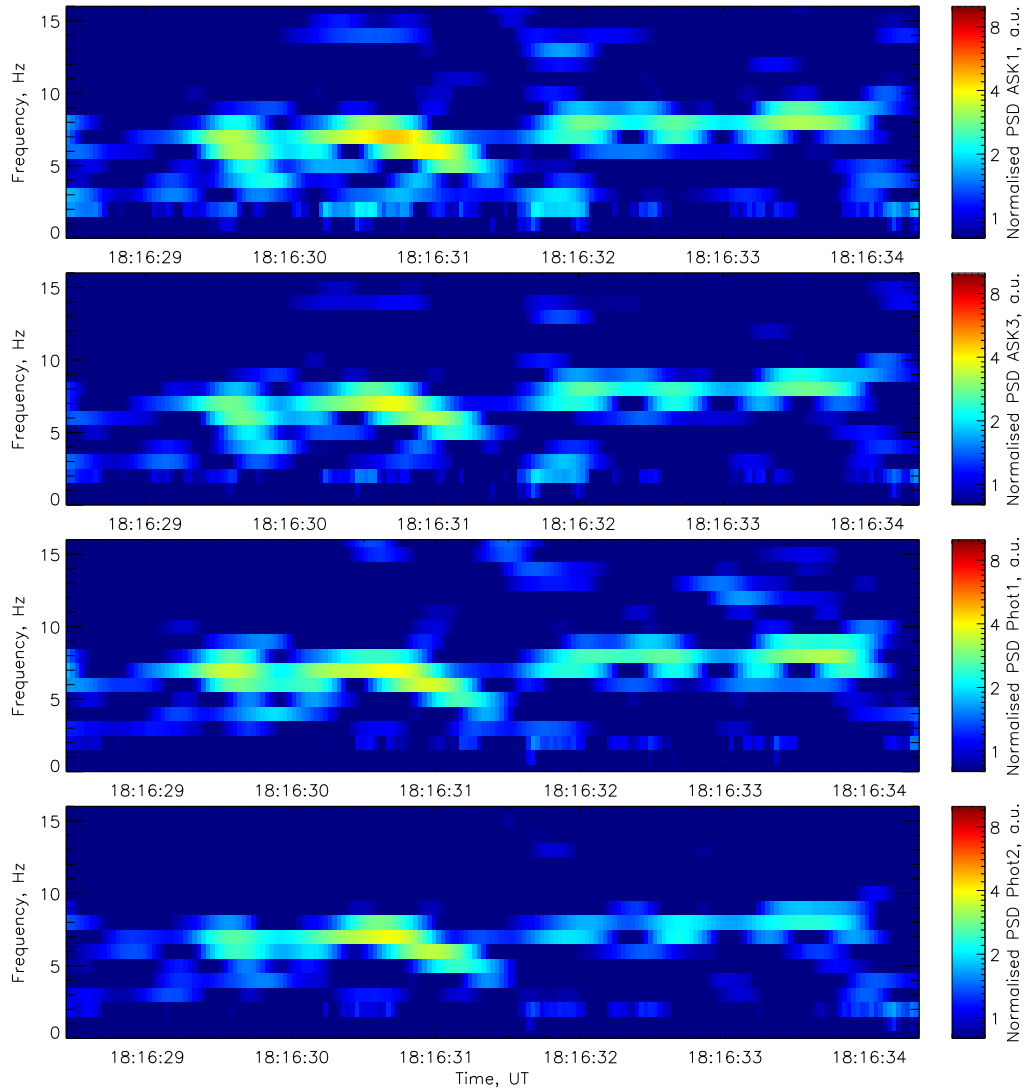

Figure 6.10: Normalised power spectra for the ASK cameras and photometers for part of the 22 October 2006 event. Top–bottom: ASK1 camera (I_{6730}), ASK3 camera (I_{7774}), photometer 1 (I_{4709}), photometer 2 (I_{8446}).

around 8–45 keV, with a mean of 20 keV. These observations differ from observations of FABs reported by *Arnoldy et al.* (1999) and others referenced therein, who found that FABs are widely dispersed in energy with a maximum energy at the peak energy of the inverted-V electrons.

Although EISCAT data will primarily show the result of the continuous non-flickering precipitation, it is likely there would be more enhancement at higher altitudes if the flickering had a significant low-energy component. *Grydeland et al.* (2008) showed that flickering precipitation can modulate the radar backscattered power from the upper E-region. Their EISCAT experiment did not record backscatter from below 130 km, so it is not known whether there were larger modulations in the lower E-region. The "conditional integration" technique they used requires raw data from each individual radar pulse, which is not available with the arc1 experiment, and therefore it is not possible to perform a similar analysis on the data used in this work.

Results from the analysis of the chirps are plotted in figure 6.11. Both the peak frequency (dashed line) and the flickering electron precipitation energy estimated from the peak PSD ratio (solid line) are plotted for each chirp. The peak frequency is calculated using exactly the same weighting as the peak ratio, i.e. the sum of the PSDs for both cameras is used. The correlation coefficients between the peak frequency and electron precipitation energy are given. The top three panels all show a very clear anti-correlation between the flickering peak frequency and electron precipitation energy as the chirp progresses (note that the electron energy axis is inverted). The first of these is a "down chirp", where the frequency decreases by about 1.5 Hz over 1 s and the energy increases at a rate of 4–5 keV/s. The other two are "up chirps" where the frequency increases. These chirps are similar, and show roughly equal frequency and energy changes, although the second chirp is temporally longer than the third. The rate of frequency change is approximately 1.5 Hz/s for both chirps, with an energy change of approximately 12 keV/s.

The fourth chirp (figure 6.4 and bottom panel of figure 6.11) is more complicated. The frequency stays roughly constant at about 8 Hz for the first second, before the peak of the spectrum splits into two parts at about 5 Hz and 2 Hz. These two peaks are distinct for approximately half a second, before rejoining at the lower frequency. At the end of the chirp (19:28:06 UT) the OI/O_2^+ PSD ratio is lower than at the start of the chirp (19:28:05 UT), agreeing with the other three chirps in that the PSD ratio is proportional to the flickering frequency.

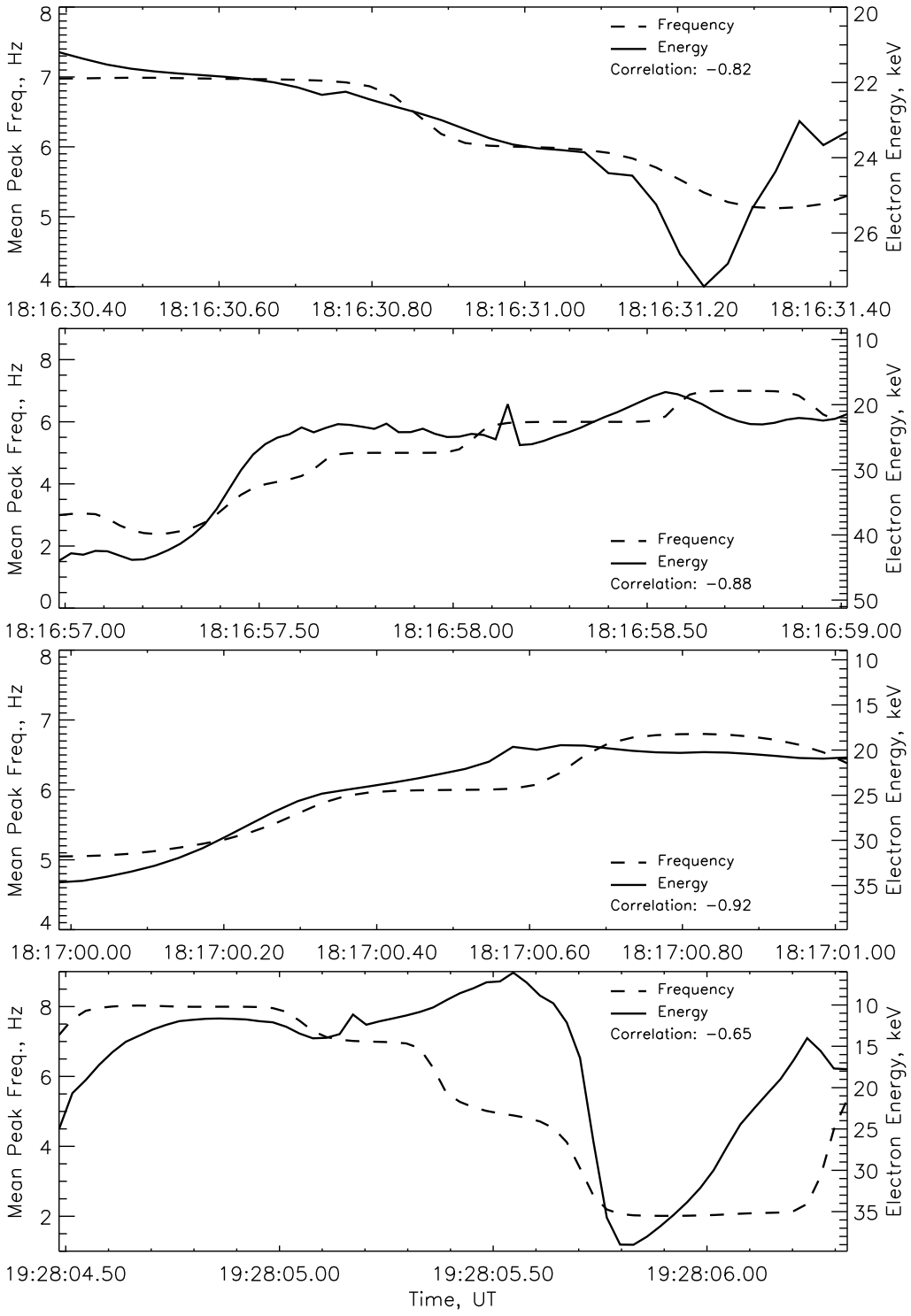

Figure 6.11: Peak frequency and electron precipitation energy over the duration of chirps 1–4 (top–bottom).

This conclusion is also supported during the period where the spectra have two peaks. At this time (19:28:05.4 – 19:28:05.9 UT) the higher frequency flickering is stronger in I_{7774} (lower energy precipitation), whereas the lower frequency flickering is stronger in I_{5620} (higher energy precipitation).

All four chirps support the conclusion that the electron precipitation energy of flickering aurora is inversely proportional to the flickering frequency to first order and on short timescales. This conclusion has been supported by both up chirps and down chirps. There is no correlation over longer timescales where several distinct periods of flickering aurora are observed. So far no other flickering chirps have been found in ASK data.

6.6 Discussion and conclusions

The above results are consistent with the theory that the resonance interaction between EMIC waves and precipitating electrons is responsible for flickering aurora, and that the wave parallel phase velocity is the primary factor limiting electron acceleration, rather than the magnitude of the wave parallel electric field. As electrons accelerated by the wave subsequently escape towards the ionosphere their precipitation energy will be equal to their resonant energy at the time of escape. *Sakanoi et al.* (2005) calculated the resonant energies of electrons within an EMIC wave under different conditions. Their work predicts that the resonant energy is lower for higher frequency EMIC waves, as the peak parallel phase velocity is lower for higher frequency waves. They calculate the resonant energy directly from the parallel velocity of resonant electrons, which is derived from the EMIC wave dispersion relation for given values of the perpendicular wave number (flickering spot size traced up the magnetic field line), H^+ ion concentration, O^+ ion concentration, and magnetic field. These calculations have been reproduced following the method described in section 2.3.1, for EMIC waves at frequencies of 4 Hz, 6 Hz, and 8 Hz, for the low plasma density conditions ($\sim 10^1$/cc above 3000 km) used by *Sakanoi et al.* (2005) and plotted in figure 2.6. The resulting wave parallel phase velocities, together with the Alfvén velocity, are shown as a function of altitude in figure 6.12. The clear relationship between wave (flickering) frequency and parallel phase velocity (electron precipitation energy) is matched in the ASK observations of chirps. A flickering patch diameter of 12 km at 120 km height was used in these calculations, as was used by *Sakanoi et al.* (2005). Although smaller flickering structures were reported in chapter 5, these structures are thought to be the result of interference between multiple EMIC waves, and so do not lead to an accurate estimate of $k_\perp$. Using a flickering patch diameter of 1 km produces a peak wave parallel phase velocity approximately 3 times smaller than that obtained using a flickering patch diameter of 12 km. The relationship between wave parallel phase velocity and frequency is reproduced for any $k_\perp$.

The ASK observations are completely consistent with the model suggested by *Chen et al.* (2005) of EMIC wave acceleration in combination with a parallel potential drop. The fact that ASK does not see flickering precipitation at energies less than the potential drop peak energy supports the theory that the wave acceleration occurs at heights above the potential drop, and that the flickering precipitation is accelerated by the potential drop together with the non-flickering

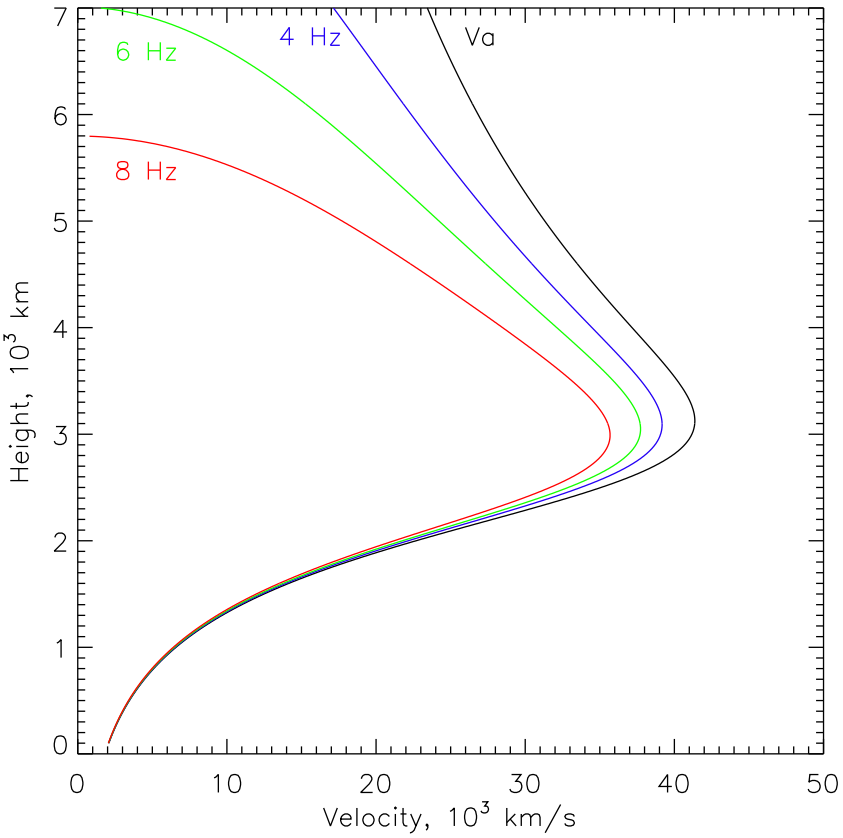

Figure 6.12: Height profiles of the wave parallel phase velocity for 8 Hz, 6 Hz, and 4 Hz O^+ EMIC waves, together with the Alfvén speed.

precipitation. The small phase difference observed between emissions indicates a relatively narrow spread in energy of the flickering precipitation. The entire energy distribution created by the wave acceleration is shifted to higher energies by the potential drop, and therefore as a fraction of the peak energy, the width of the distribution is relatively narrow. Variations in the magnitude of the potential drop could also explain the lack of correlation between energy and frequency over timescales longer than a single chirp. This could also be explained by plasma density fluctuations causing variations in the EMIC wave speed, or by other differences between waves generated at different times.

Inertial Alfvén waves with the dispersion relation given in equation 2.3 (without correction for finite frequency effects) would not produce the observed relationship between flickering frequency and electron precipitation energy. The parallel phase velocity of such waves is not dependent of the frequency of the wave. It is the finite frequency correction present in the dispersion relation for EMIC waves (equation 2.4) which leads to the theoretical relationship shown in figure 6.12. This is evidence supporting the theory that flickering aurora is caused by EMIC waves. Note that in the model developed by *Chen et al.* (2005) inertial Alfvén waves were considered, rather than specifically EMIC waves. However, the conclusion that the wave parallel phase velocity is the dominant factor limiting electron acceleration rather than the wave parallel electric field is valid for either type of wave.

The spatial analysis presented in chapter 5 produced results supporting the conclusions drawn in this chapter. The strong temporal correlation between the flickering PSD and the brightness of the non-flickering aurora, combined with the lack of spatial correlation between flickering structure and the background auroral brightness, supports the theory that the flickering was caused by EMIC waves above a parallel potential drop. As the magnitude of the potential drop varied the number of reflected and backscattered electrons suitable for acceleration by the EMIC waves also varied, together with the acceleration of unmodulated "background" auroral electrons. This gave rise to the strong temporal correlation. Interference between multiple EMIC waves was primarily responsible for the spatial structure of the flickering aurora, and therefore there was no correlation between flickering structure and non-flickering structure within the auroral arc on the small-scales observed by ASK. The two are probably correlated on larger scales where the spatial structure of the potential drop will have an affect, but it is not possible to investigate this using ASK.

While the theories suggested by *Chen et al.* (2005) and *Sakanoi et al.* (2005) can explain the properties of the chirps observed with ASK, further work is necessary to explain the physical processes causing the chirps. The change in frequency may be caused by the source of the EMIC wave moving, either because the local ion cyclotron frequency increases (decreases) as the wave source moves downwards (upwards), or because a Doppler shift is introduced. Assuming the observed flickering frequency matches the local oxygen ion cyclotron frequency at the wave source (no Doppler shift), a change between 7 Hz and 5.5 Hz corresponds to a height change between approximately 6300 km and 7300 km. This inferred height change occurs over an interval of about 1 s, corresponding to a speed of 1000 km/s. This is the same order of magnitude as the Alfvén speed at these altitudes under the high density plasma ($\sim 10^3$/cc) case modelled by *Sakanoi et al.* (2005). However, in order to accelerate electrons to several keV the EMIC wave speed must be at least an order of magnitude greater than this, which is possible at lower altitudes ($\sim$3000 km) under the low density plasma ($\sim 10^1$/cc) case. *Bellan and Stasiewicz* (1998) demonstrated how fine-scale, deep plasma cavities can be created by the ponderomotive force of inertial Alfvén waves. A similar process could have occurred during the events studied here, creating a low density plasma cavity. EMIC waves within this cavity could then have attained high parallel phase velocities, accelerating electrons to high energies.

It is worth emphasising that the correlation shown by the chirps cannot be explained using a velocity dispersion argument. The dispersion is most apparent at higher frequencies, where it decreases the OI/N_2^+ PSD ratio more than at lower frequencies. This is in opposition to the correlation which is observed in the ASK results. The chirps themselves cannot be explained using a velocity dispersion argument, as both up-chirps and down-chirps have been observed.

Both energy dispersion and the wavelength range of optical observations may limit which FABs are clearly observable as flickering aurora from the ground. FABs which are spread over a wide energy range will be significantly dispersed as discussed previously. When observing in a wide wavelength band covering multiple emissions, it is likely that the different emissions detected simultaneously will be sensitive to different energies. This will reduce the apparent flickering amplitude relative to the non-flickering brightness, as the oscillations will not be in phase between emissions. In addition, some of the emissions may not be prompt. These will therefore display only weak flickering if any, and so will reduce the proportion of the total auroral brightness which is flickering. The clearest flicker-

ing will be observed when the oscillations are confined to a narrow energy range, and observations are made in prompt emissions sensitive primarily to those energies, as is the case for the ASK observations presented here. Also, cases in which EMIC wave acceleration occurs above a parallel potential drop are more likely to be observed as flickering aurora as the accelerated "flickering" electrons will have energies which are high enough to produce significant optical emission. However, FABs are more likely to be observed when wave acceleration occurs below a parallel potential drop, producing low-energy precipitating electrons which can be detected by typical rocket-based instruments but may not be easily observed as optical flickering aurora.

Most of the errors associated with these measurements and results are systematic, and therefore will not affect the conclusions. Uncertainties related to absolute intensity calibration (roughly estimated at 30%) will not affect the trend found within the chirps, but could affect the electron precipitation energies determined from the measurements. However, this will affect both flickering and non-flickering calculations equally, so the overall conclusions are valid independent of these uncertainties. The same is true in relation to modelling errors, the most significant of which is due to uncertainty in the O/N_2 concentration ratio estimated by the model. The electron energies observed during these events could be overestimated by a factor as large as 3. However, the good agreement between energies inferred from ASK and EISCAT data independently suggest these systematic errors are minimal, and it is unlikely that the electron energies are overestimated by more than a factor of 1.5. Random errors associated with noise within the camera images are minimised by averaging over a large number of pixels, and have a negligible effect on the results.

This is the first reported detailed analysis of simultaneous multi-spectral optical observations of flickering aurora, and is also the first reported analysis of flickering auroral chirps. Future work should include searching for further flickering events in ASK data to confirm the correlation between frequency and energy with a larger number of chirp observations. The ASK instrument has also been located on Svalbard, where it is possible to observe dayside aurora. There may have been ASK observations of flickering events within dayside aurora, which could be compared with the nightside events studied in this work. In addition variations in the energy spectra of flickering aurora spatially across the ASK camera images should be investigated.

6.7 Summary

In the events studied here the energy of flickering electron precipitation was higher than the energy of the non-flickering auroral electrons, and was inversely proportional to the flickering frequency over short timescales. These observations can be explained by the resonance interaction between electrons and EMIC waves modulating the electron precipitation above and within a parallel potential drop, which further accelerates these electrons. This theory was proposed and modelled in detail by *Chen et al.* (2005) in the case of inertial Alfvén waves (which includes EMIC waves). *Sakanoi et al.* (2005) suggested that small-scale structures seen within flickering aurora can be explained by interfering EMIC waves. A consequence of their model and calculations is that lower frequency waves should accelerate electrons to higher energies than higher frequency waves. The ASK observations presented here are the first reported observations clearly showing this behaviour. It is significant evidence supporting the idea that the parallel phase velocity of the wave is the primary factor in determining the energy of wave-accelerated electrons responsible for flickering aurora, rather than the amplitude of the parallel electric field. While possibly related to the parallel potential drop peak energy, the maximum energy of flickering electron precipitation is not limited by the potential drop. The only theory listed in table 2.1 which can explain all properties of the ASK observations presented here is that of *Chen et al.* (2005) and *Sakanoi et al.* (2005).

Chapter 7

Intercalibrating Reimei Observations Using the Southampton Ionospheric Model

This work was initiated by B. S. Lanchester and the author as part of a larger International Space Sciences Institute (ISSI) study led by H. U. Frey. The analysis of the events presented here was carried out entirely by the author, although the results and interpretation were discussed with B. S. Lanchester, T. Sakanoi and K. Asamura.

7.1 Introduction

This chapter demonstrates a powerful new technique for intercalibrating Reimei optical and particle measurements using the Southampton Ionospheric Model. It was originally developed for an ISSI "team" led by H. U. Frey, and a description of an early form of the technique has been published by *Frey et al.* (2010).

As described in section 3.2 the Reimei satellite carries both particle detectors (ESA/ISA) and optical imagers (MAC), and can simultaneously measure auroral particle precipitation and observe the resulting optical aurora. Using ESA it is possible to measure the total energy flux and energy distribution of precipitating electrons up to about 12 keV. However, ESA gives no information on high-energy electrons above this cut-off energy, which can be a serious limitation when studying many auroral events. An alternate method of estimating the total electron flux is by measuring the brightness of the aurora in a specific emission known

Event	Date	Time (MLT)
1	2005/11/30	3:14
2	2005/12/22	1:04
3	2005/12/26	1:11
4	2005/12/28	1:00
5	2005/12/29	3:59

Table 7.1: Dates and times of the 5 events

to have little dependence on electron precipitation energy. Both 670.0 nm and 427.8 nm emissions observed by MAC fulfil this criterion, but MAC cannot give accurate measurements of the auroral brightness due to an unknown and variable background. The background is a result of additional light sources (for example the Moon) as well as auroral light reflected from the surface of the Earth. By employing the technique described here MAC observations can be calibrated using ESA observations in combination with an ionospheric model, allowing the total electron flux (and hence flux of high-energy electrons above 12 keV) to be found. An early version of the technique was utilised by *Frey et al.* (2010) to estimate the total electron flux in a substorm onset arc.

Five events have been studied as part of this work, providing examples of the application of the intercalibration technique under different conditions. The dates and magnetic local times of the five events are given in table 7.1. Events 1 and 5 took place over the Arctic Ocean in the European sector, while the remaining three events took place over mainland northern Canada. The geographic locations of the centre of the MAC field of view (pink trace) and footprint of the ESA detector (yellow trace) for each event are shown in figure 7.1. Note that in most cases the trace is longer than the corresponding event, but the times of the trace end points are shown in the figure. Each event is described in detail in section 7.3.

7.2 Description of the technique and analysis of the first event

The aurora during the first event (starting 04:04:34 UT) is highly structured with banding parallel to the main arc, but is fairly static. For the first half of the event the satellite footprint crosses several weaker bands before entering the main arc at 04:07:59 UT. The main arc is structured into two major bands with additional

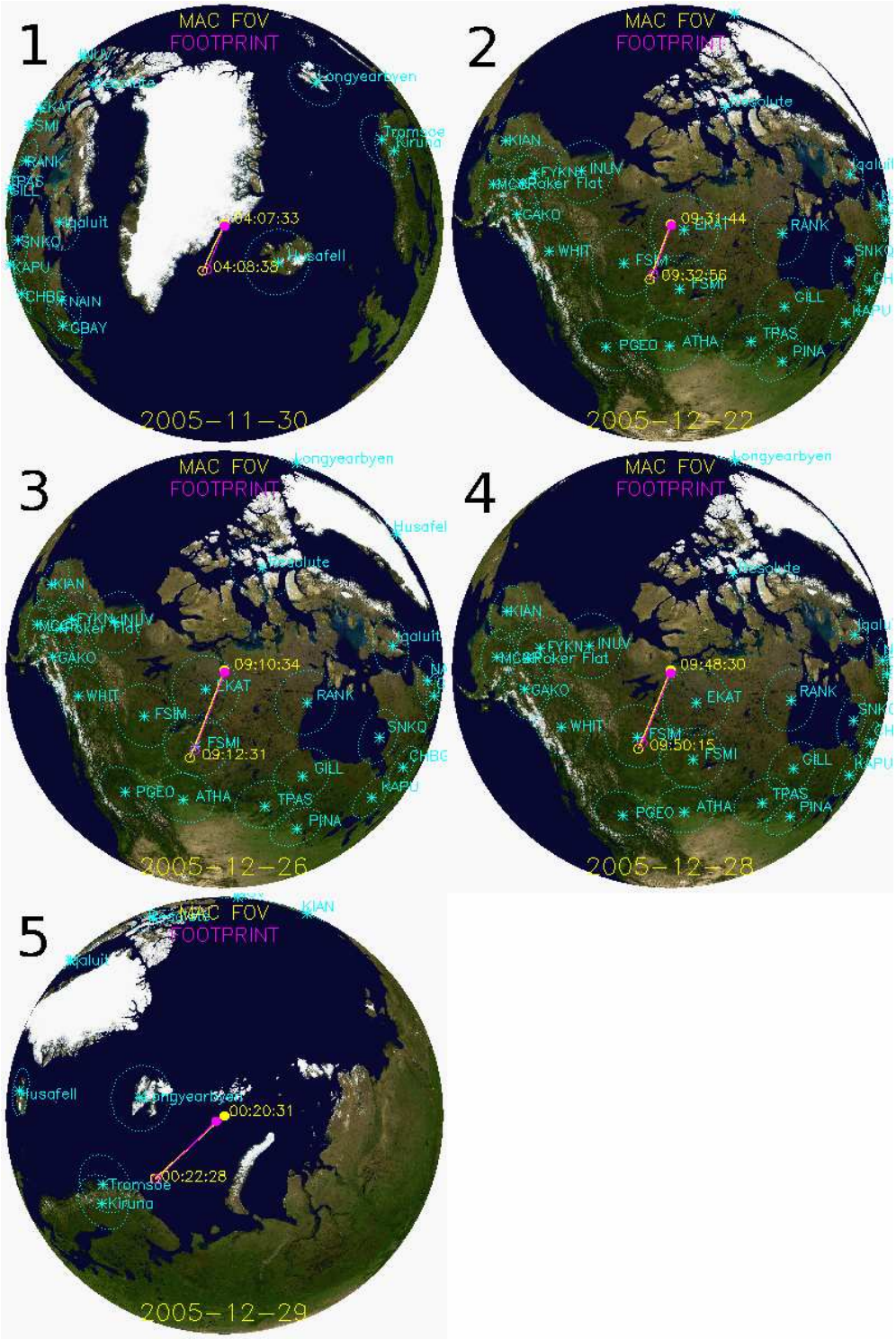

Figure 7.1: Global location of events 1–5. The yellow track shows the position in the centre of the MAC field of view, and the pink track shows the magnetic footprint of the ESA detector. Light blue points mark the locations of various ground-based auroral observatories. Images provided by T. Sakanoi through the ISAS/JAXA Data Archives and Transmission System (DARTS) at `http://www.darts.isas.ac.jp/stp/reimei/`.

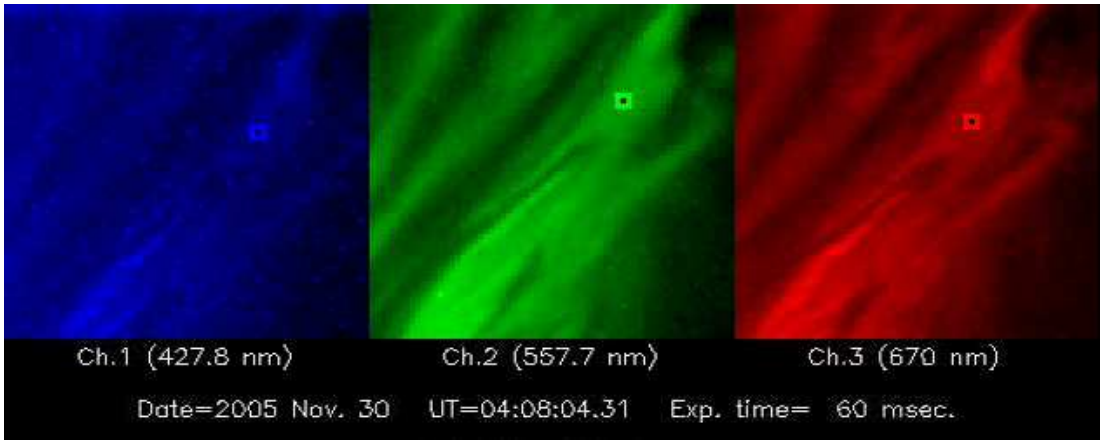

Figure 7.2: Example MAC images from the first event.

parallel structure on smaller scales. The trailing band (crossed second) is brighter than the first. The satellite footprint enters this second band at 04:08:03 UT. A set of example MAC images from 04:08:04 UT when the satellite footprint crossed the second band is shown in figure 7.2. The aurora moves towards the top of the image as the satellite flies over. The square marker in each image shows the location of the footprint. The ESA electron spectra and MAC brightnesses at the satellite footprint for the first event are shown in the top and bottom panels of figure 7.3 respectively. The satellite footprint position within the MAC images is found using a geomagnetic field model. It should be noted that a high voltage step between sets of measurements causes successive energy bins of the ESA detector to overlap in energy range, leading to some artifacts in the ESA plots. This is especially apparent when the mean differential flux is lower in the 8.74 keV bin than in the 8.82 keV bin, due to the energy range of the 8.82 keV bin being entirely contained within the range of the 8.74 keV bin, particularly in events 3 and 5 presented later in section 7.3.

The Southampton Ionospheric Model (described in chapter 4) has been used in this work. The model can successfully simulate the height profile and height-integrated brightnesses of 670.0 nm and 427.8 nm emissions for an arbitrary energy spectrum of precipitating electrons, for example as measured by ESA. The MAC filter transmission curves are specifically taken into account, so modelled and measured brightnesses can be directly compared. Figure 7.4 shows the modelled height-integrated brightnesses of 670.0 nm and 427.8 nm emissions for a 1 mW/m^2 mono-energetic electron spectra of varying peak energy. This shows that both emissions have little dependence on electron energy above about 1 keV.

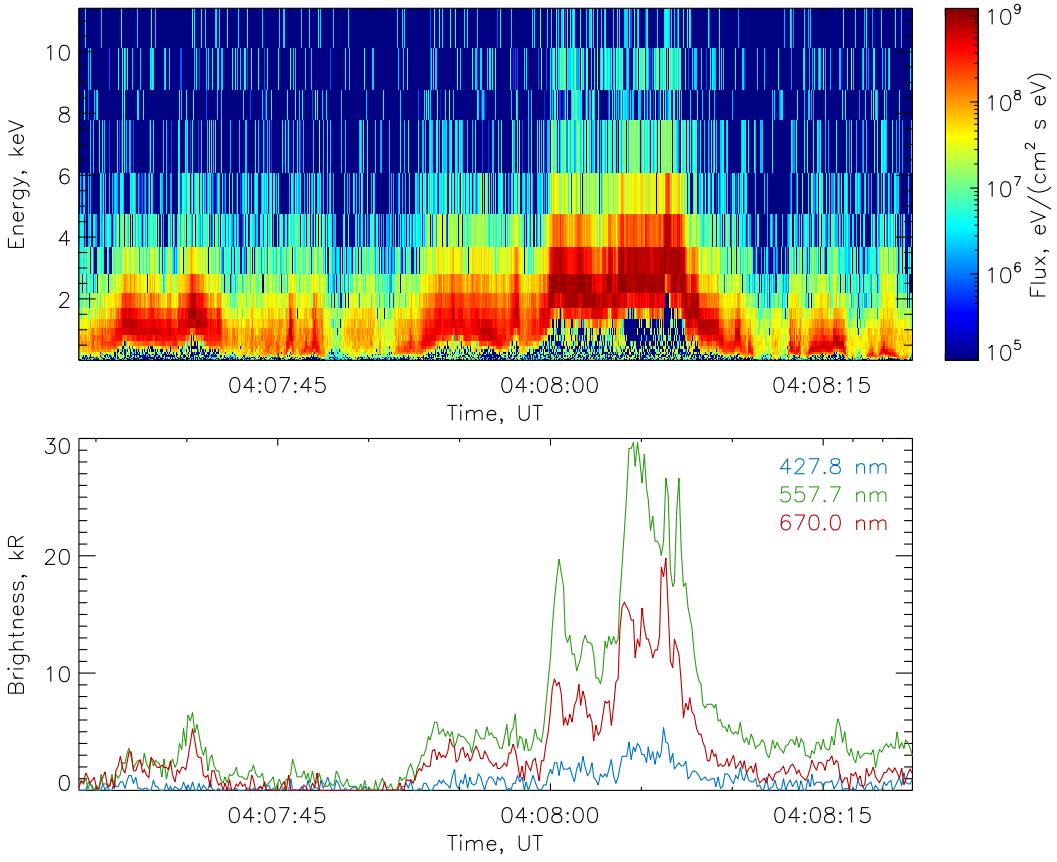

Figure 7.3: Electron spectra measured by ESA (top panel) and auroral brightnesses measured simultaneously by MAC (bottom panel) during event 1.

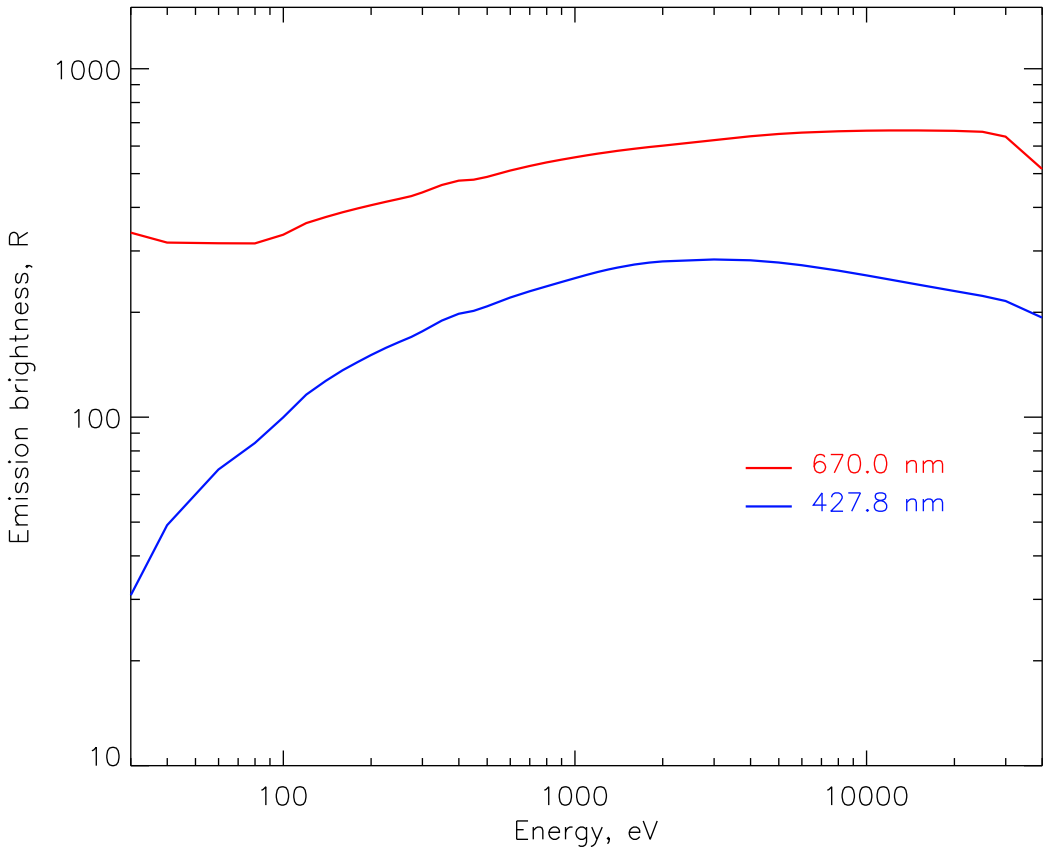

Figure 7.4: The dependence of emission brightness on electron precipitation energy, modelled under conditions during event 1.

The 557.7 nm emission is difficult to model due to a complicated energy transfer process between nitrogen and oxygen, and therefore has not been used in this work. MAC measures brighter emission in 670.0 nm compared to 427.8 nm, partly due to a wider 670.0 nm filter transmission. This study therefore concentrates on 670.0 nm observations to benefit from a better signal-to-noise ratio.

The top panel of figure 7.5 shows the 670.0 nm emission brightness measured by MAC in the footprint position together with the same emission modelled using the ESA electron spectra (black line). Individual MAC data are shown as pluses, while the same data interpolated onto the finer ESA time grid are shown as a solid blue line. The trends in modelled and measured data agree closely when there is negligible electron flux above the 12 keV cut-off of the ESA detector. Note that the scales for the model data (left axis) and measured data (right axis) are different. The middle panel shows the same interpolated MAC and modelled data plotted against each other. The colour of each point corresponds to the time

of measurement, following the colour scale shown on the abscissa of the bottom panel. A set of coefficients relating measured brightness to modelled brightness is obtained by performing a least-squares fit to these data. Assuming ESA gives accurate values of the precipitating electron flux, these coefficients provide an estimate of the background measured by the MAC camera and can be used to calibrate MAC data. ESA does not give accurate values of the precipitating electron flux when there are electrons with energies above 12 keV, and therefore data from this period are ignored in the fitting process (points shown in grey). The times of this period are estimated by noting when brightnesses measured by MAC are exceptionally high compared to modelled brightnesses and when ESA shows evidence of electron spectra continuing to high-energies. The fit is shown as a straight line in the middle panel of figure 7.5, with the gradient and ordinate offset also stated in the panel. The offset corresponds to the background due to non-auroral sources such as the moon and airglow, whereas the larger-than-unity gradient corresponds to reflected auroral emission.

The process is repeated for each MAC pixel within a distance of 2 pixels from the estimated footprint position, and the pixel which leads to the highest correlation coefficient between measured and modelled emission brightnesses is identified. This pixel is then used as the footprint position when calibrating the MAC data and producing the results shown in this chapter. This step is necessary as the geomagnetic field model does not always produce an accurate footprint position. Note that the footprint position is defined with a constant offset from the time-varying footprint pixel estimated by the geomagnetic field model, so inaccuracies in the field model can still produce artifacts in the data. However, the offset pixel will on average be a better estimate of the footprint position than the pixel suggested by the geomagnetic field model alone.

In order to obtain estimates of the total electron flux from calibrated MAC data it is necessary to know the brightness produced per unit electron flux, or excitation efficiency, β. This has a slight dependence on electron precipitation energy, as shown in figure 7.4. It is also dependent on the concentration of N_2 (for 670.0 nm), which in turn is dependent on time of day, location, and geophysical activity, and is therefore different for each event. The Southampton Ionospheric Model used here employs the MSISE-90 model (*Hedin*, 1991) to provide concentrations of the major neutral species. To calculate β the modelled emission brightness (black line in top panel of figure 7.5) is divided by the total input electron flux at each time step. Values where the total electron flux is negligible

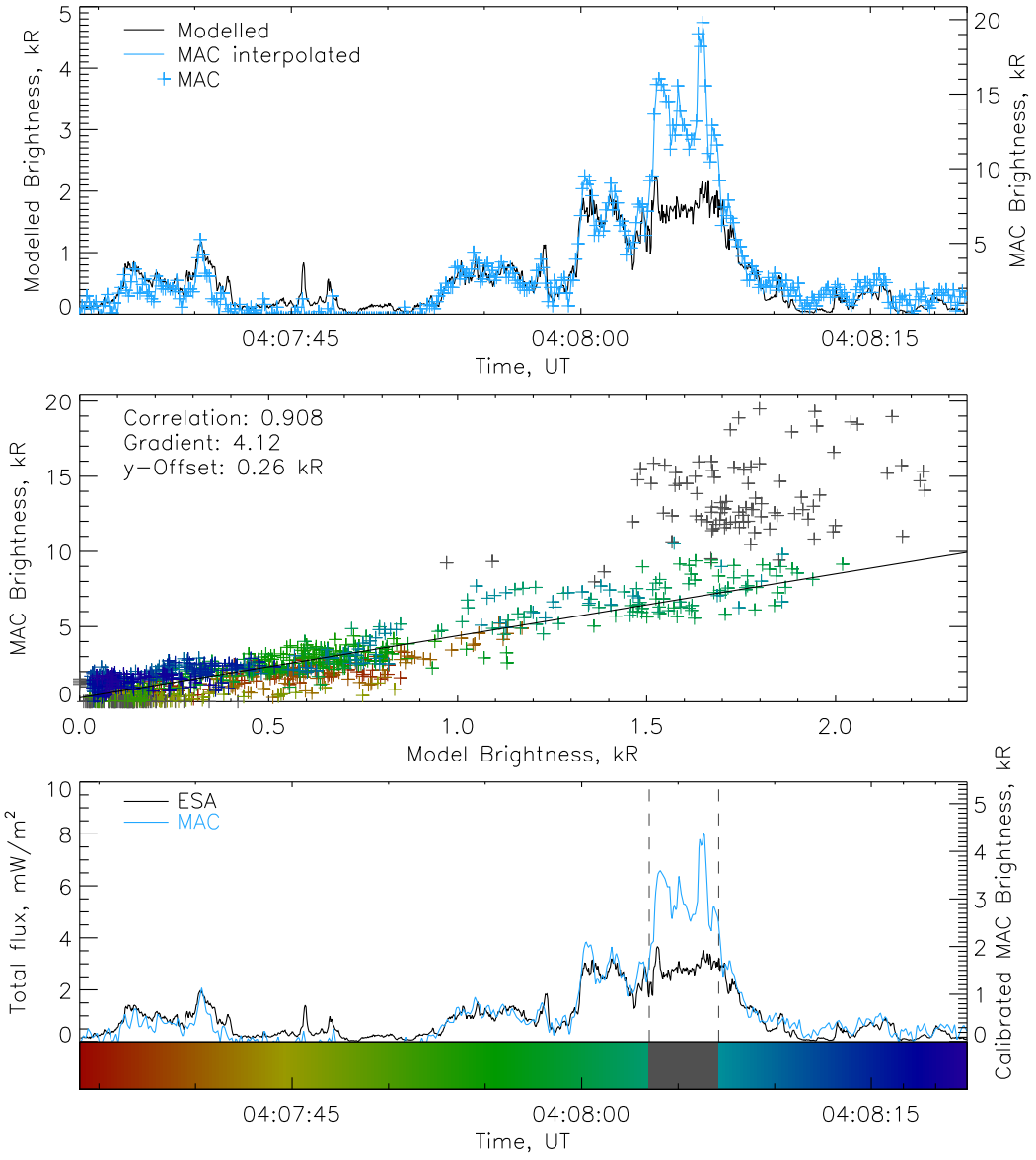

Figure 7.5: Modelled and measured 670.0 nm emission brightness on a line plot (top panel) and scatter plot (middle panel), and total electron fluxes (bottom panel), for event 1.

Event	β (673.0 nm), Rm^2/mW
1	580
2	617
3	607
4	612
5	643

Table 7.2: Brightness per unit electron flux for each event.

are discarded before the mean is calculated. This mean is used as the value of β, and is given in table 7.2 for each event. The calibrated MAC data are divided by β to give total electron flux.

The total electron flux as measured by ESA (black line) and derived from calibrated MAC data (blue line) is shown in the bottom panel of figure 7.5. At most times the two measurements of flux agree closely, suggesting the majority of the electron precipitation was at energies below 12 keV and so was completely measured by ESA. However, during the time period 04:08:03–04:08:07 UT MAC recorded substantially greater brightness than at any other time during the rest of the event. This period corresponds to a bright structure seen within the main auroral arc. ESA did not record significantly more flux at this time than during the immediately preceding period, suggesting the bright structure was a result of high-energy electron precipitation at energies above 12 keV. The electron spectra recorded by ESA (top panel of figure 7.3) does not show much electron flux above about 6 keV, indicating that either the electron distribution has a long tail extending to high energies or that a separate accelerated electron population was precipitating exclusively at energies above 12 keV.

7.3 Other events

For much of event 2 it is clear that the electron precipitation was very high energy. The event has been analysed in exactly the same way as event 1. The electron spectra measured by ESA are shown in the top panel of figure 7.6, and the measured and modelled auroral brightness is shown on a scatter plot in the middle panel of the same figure, coloured according to the scale on the abscissa of the bottom panel. The bottom panel shows the ESA-measured total electron flux, together with the total electron flux obtained from calibrated MAC data. As with event 1, the grey portion of the colour scale corresponds to the time period

excluded from the fitting process. During the first second of the event (starting at 09:31:45 UT) the satellite footprint passed over the highly dynamic leading edge of the arc system, which exhibited a wide spread of electron energies and rapidly changing spatial structure. This was followed by a period of less intense diffuse aurora before the footprint passed over a region of very bright aurora from 09:31:51 UT until 09:31:56 UT. The total electron flux measured by ESA decreased following the initial dynamic leading edge and stayed low even when the auroral brightness increased substantially. After passing the main arc Reimei flew over a smaller, less bright arc, at about 09:32:12 UT. ESA measured more electron flux over this arc than the brighter main arc. By constraining the fit to exclude the high-energy main arc while including the second arc MAC could be calibrated. It is clear that ESA greatly underestimated the total electron flux, which was very large across the main arc. The electron precipitation in the main arc was predominantly at energies greater than 12 keV.

Event 3 consists of a Reimei pass over a well-defined but internally structured and dynamic arc, and is presented in figure 7.7, in the same format as figure 7.6. During event 3, except for a small anomaly at about 09:10:59 UT, the total electron flux measured by ESA closely matches that derived from the calibrated MAC data with a very high correlation coefficient between modelled and measured brightness, suggesting there was negligible electron flux above 12 keV. The anomaly is sufficiently minor that it has not been excluded from the fitting process. The anomalous peak seen in MAC data at 09:10:59 UT corresponds to the bright trailing edge of the arc, but it is unclear why a corresponding feature is not seen in ESA data.

In event 4 Reimei crossed three distinct auroral structures. The first structure (at 09:48:40 UT) was not straight and was rapidly growing and moving as the satellite footprint passed over. The second and third structures (crossed at 09:48:52 UT and 09:49:04 UT respectively) were both quiet arcs with little structure, although the second was considerably brighter and narrower than the third. The results of applying the technique to this event (shown in figure 7.8) suggest there was negligible electron precipitation above 12 keV. As in event 3 the ESA-measured and MAC-derived total electron fluxes agree closely except for a single anomaly, in this case at 09:48:42 UT. At this time the satellite footprint was leaving the first, rapidly changing, auroral structure. The anomaly could be due to high-energy electrons on the edge of the structure, or it could be caused by insufficient spatial resolution and small errors in the magnetic footprint cal-

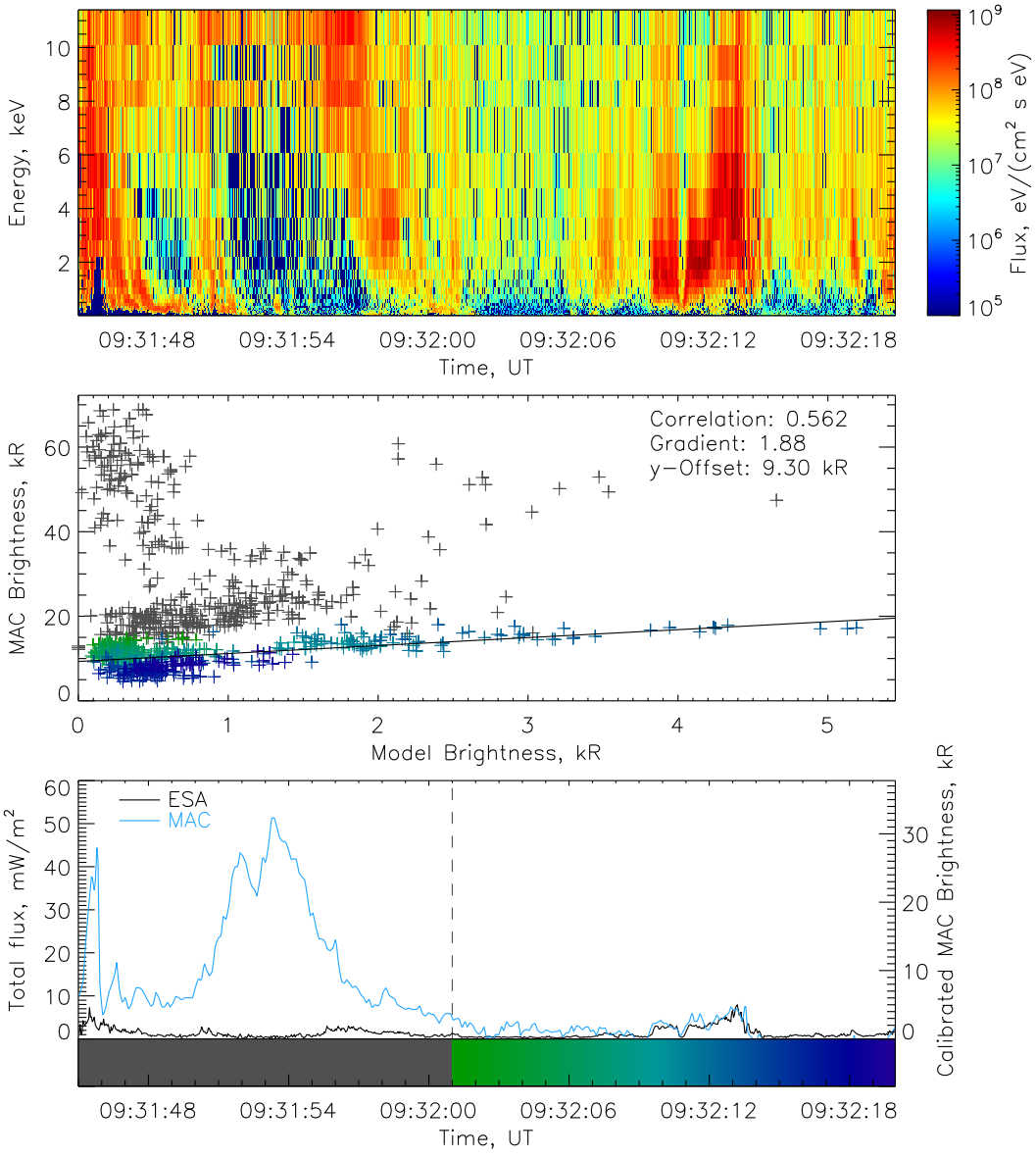

Figure 7.6: Electron spectra (top panel), modelled and measured 670.0 nm emission brightness (middle panel) and total electron flux (bottom panel) during event 2.

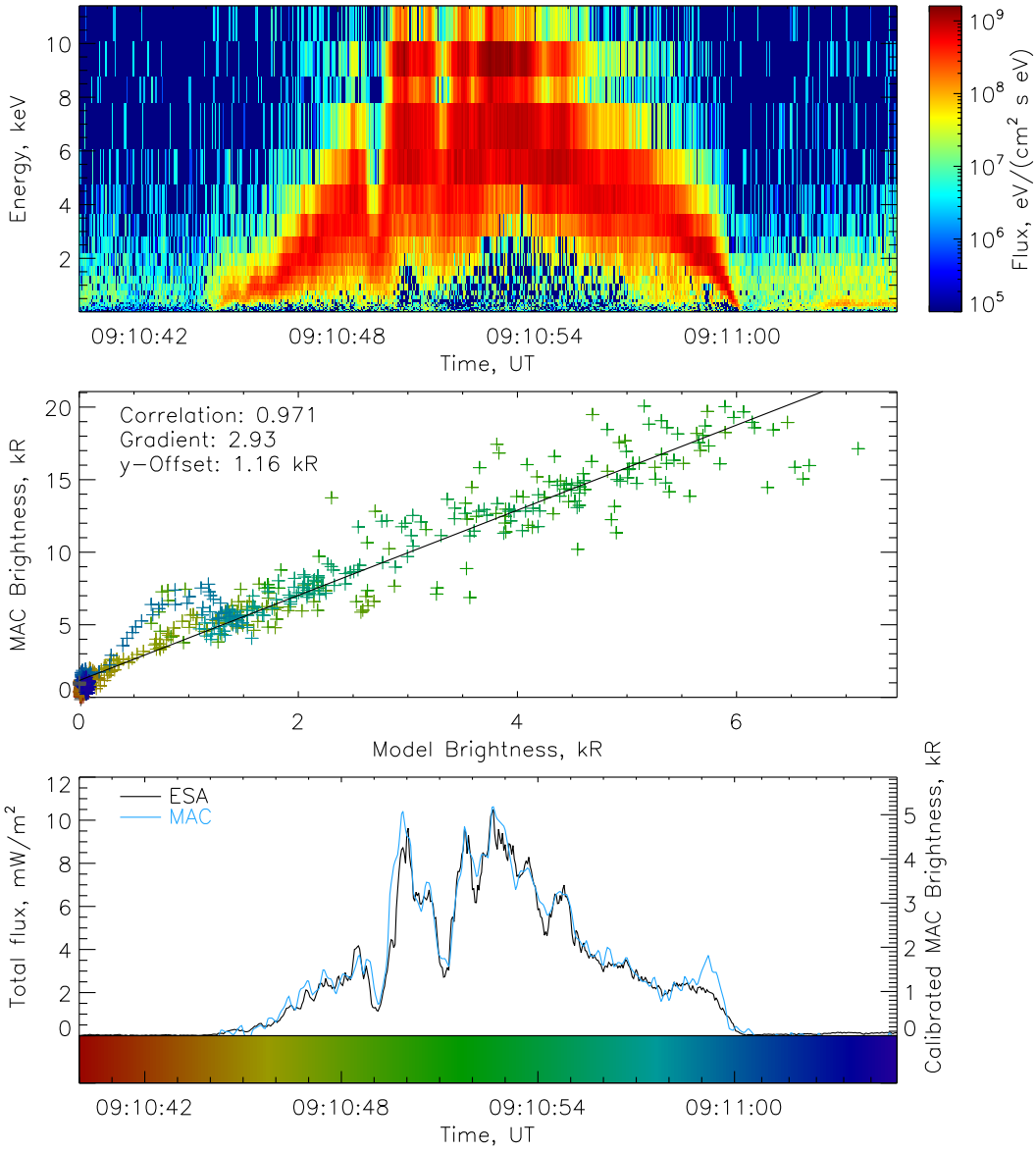

Figure 7.7: Event 3, layout as figure 7.6.

culation leading to the MAC and ESA data not being spatially coincident. This would not be apparent when passing over the two quiet arcs at 09:48:52 UT and 09:49:05 UT.

In event 5 (shown in figure 7.9) Reimei made a double crossing of a bright arc. The satellite passed over the centre of the same arc twice due to a bend in the arc and a shallow angle between the arc and the satellite path. The arc exhibited some internal dynamic structure and flows but overall was relatively steady. There is some evidence of a small number of high-energy electrons across the centre of the arc, especially during the main crossing between 00:21:56 UT–00:22:06 UT where the MAC-derived flux is slightly higher than the ESA-measured flux. Precipitating electrons are measured up to the 12 keV cut-off of the ESA detector, and it is reasonable to believe the electron energy profile extends beyond this cut-off. By excluding data from the centre of the arc a better fit between measured and modelled emission brightnesses is obtained. MAC appears to measure the second crossing of the arc (00:22:17 UT) ∼0.5s earlier than ESA, despite the previous crossing being measured roughly simultaneously by both instruments. This is probably caused by inaccuracies in the geomagnetic field model used to calculate the footprint position.

7.4 Discussion

As well as providing information on high-energy electrons not directly measured by ESA, applying the technique to each of the five events provides intensity calibration of the MAC data. The gradient of the fit shown in the middle panels of figures 7.5–7.9 is related to the albedo of the Earth beneath the aurora. For events 1 and 5 the gradient is slightly above 4, whereas it is significantly lower for the other 3 events. This can be explained by the difference in location of the events (see figure 7.1 for exact locations). Events 1 and 5 took place over the Arctic Ocean in the European sector, where the albedo will be high due to sea ice, possibly with snow cover. Events 2–4 took place over mainland Canada, where the albedo is much lower due to vegetation. However, ground albedo cannot alone explain the high gradients of the fits, as gradients significantly larger than 2 have been found.

The main reason for the high gradients is that the third MAC channel measures significant auroral "contamination" resulting from auroral emission other

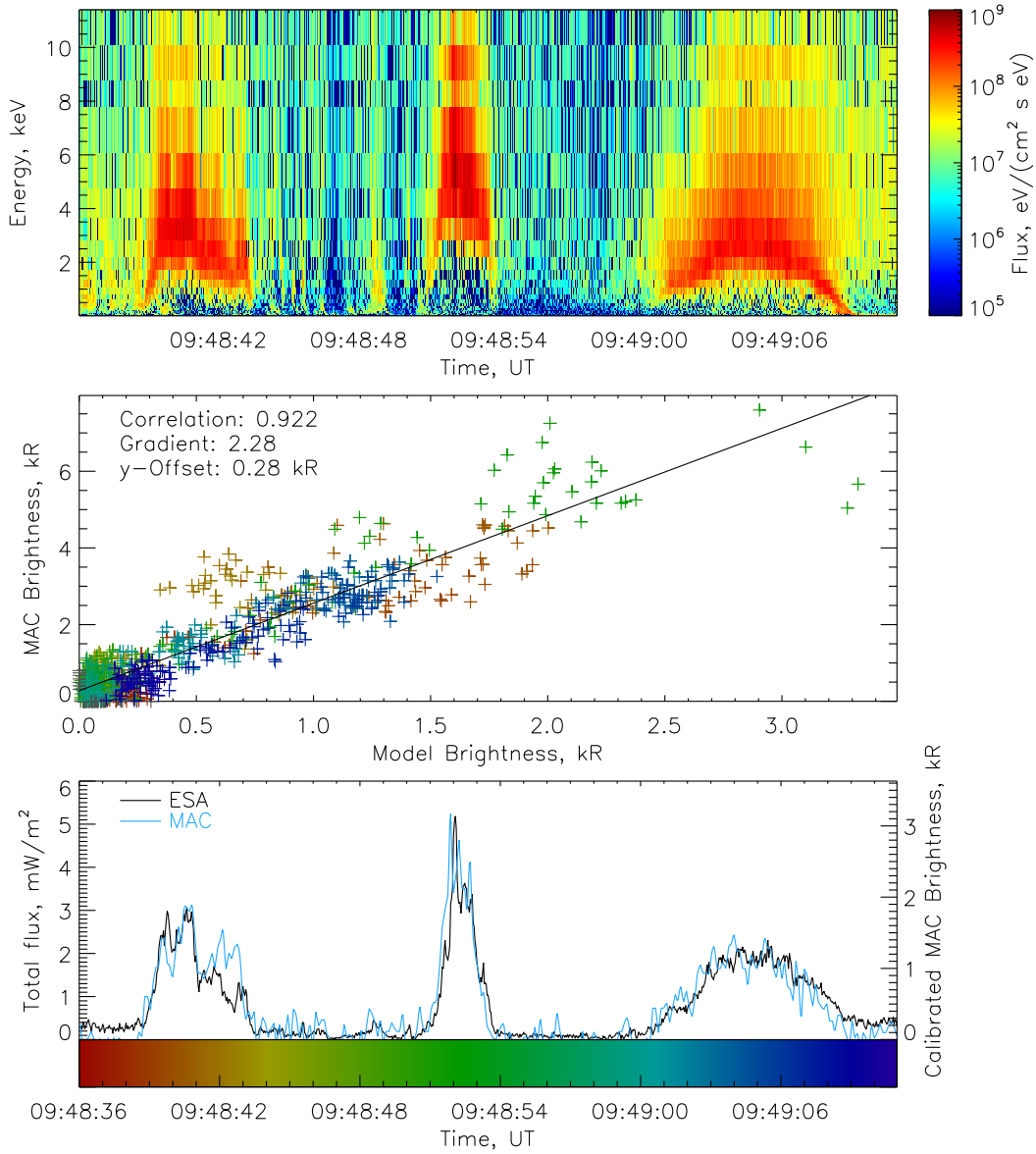

Figure 7.8: Event 4, layout as figure 7.6.

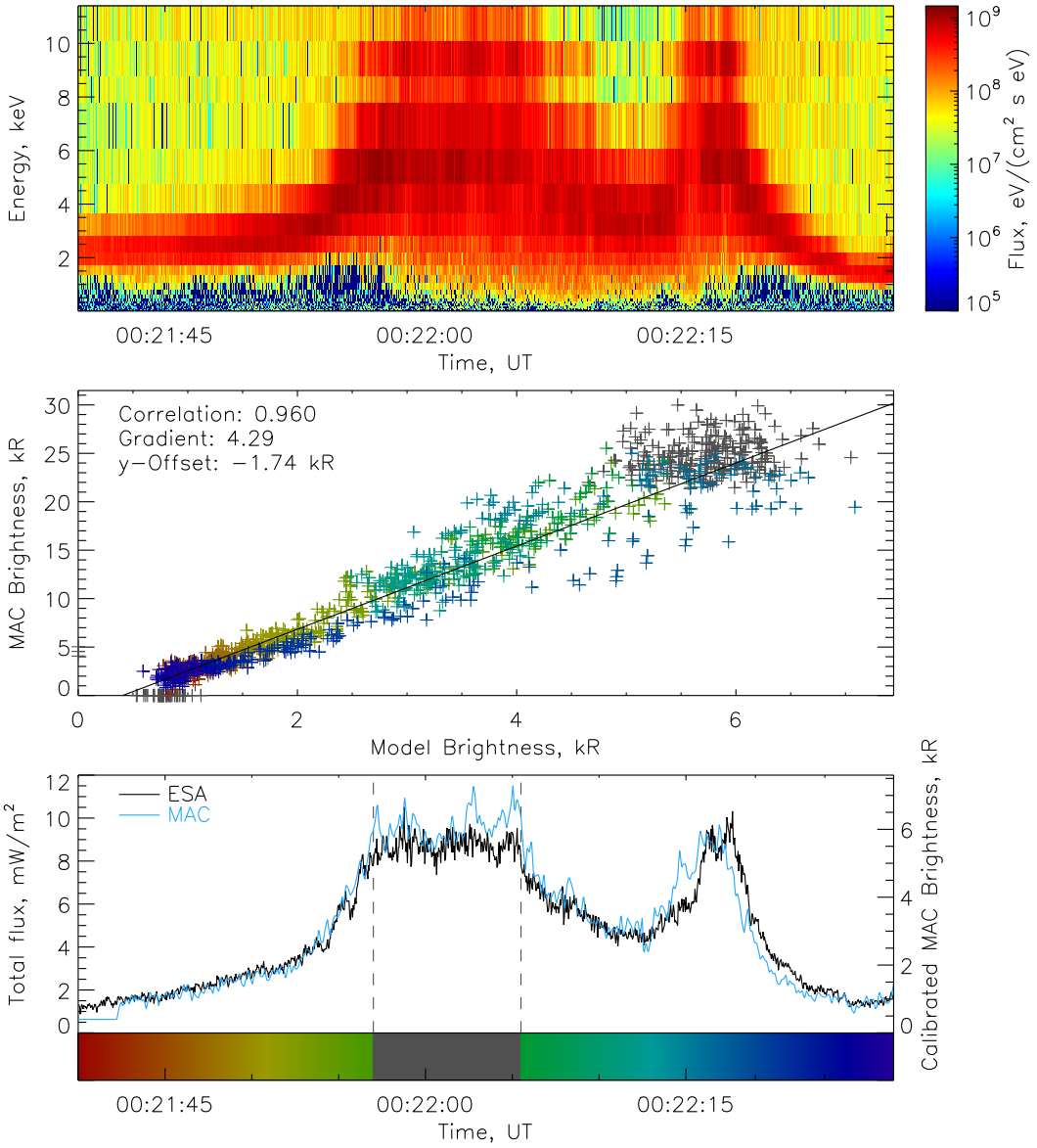

Figure 7.9: Event 5, layout as figure 7.6.

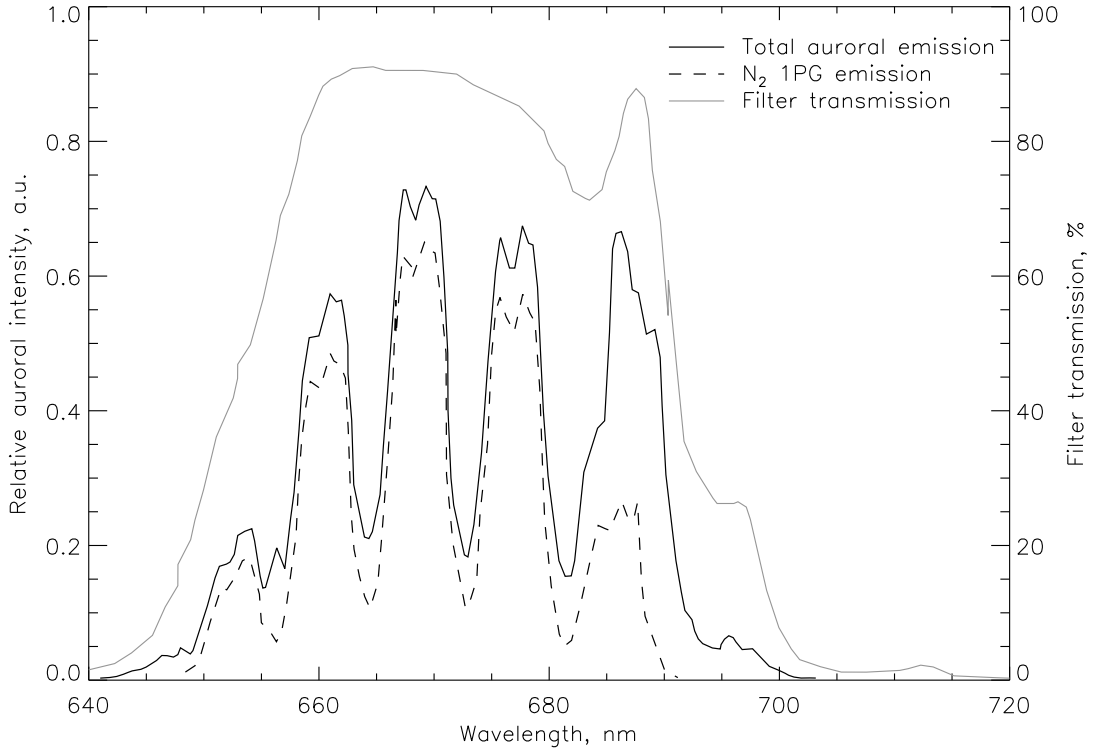

Figure 7.10: Proportion of the total auroral intensity measured by MAC coming from the N_2 1PG band.

than that in the N_2 1PG band. These emissions are not included in the ionospheric modelling, and therefore the calibrated MAC data are a measure of only the N_2 1PG emission brightness. The main source of contamination is N_2^+ Meinel band emission, but other N_2 and Oxygen emissions are also present in the wavelength range of the MAC filter (*Gattinger and Vallance Jones*, 1974). Figure 7.10 shows the total auroral intensity and intensity of the N_2 1PG band (both taken from fig. 4 of *Gattinger and Vallance Jones* (1974)) convolved with the instrument filter transmission curve, which is also shown for reference. Most contamination lies between 680.0 nm and 700.0 nm in the region of N_2^+ M (3,0). By integrating under the convolved emission spectra it is estimated that 65% of the total auroral brightness measured in the third MAC channel comes from the 5 N_2 1PG bands modelled in this work.

The technique was applied to data from the first MAC channel (427.8 nm) in order to compare the gradients of the fits for the two different cameras and further understand the reasons for the high gradients. As mentioned previously the measurements made in 427.8 nm are more noisy than in 670.0 nm, and only

2 of the 5 events produce good fits with high correlation coefficients. These are events 3 and 5, with fit gradients of 1.59 and 2.37 respectively compared with 2.93 and 4.29 when using the 670.0 nm observations. After taking into account contamination the "effective" gradients for 670.0 nm are 1.90 and 2.79; about 18% higher than the gradients for 427.8 nm. This is within the error of the pre-flight calibration of the MAC instrument and evolution in instrument characteristics since launch (estimated at up to 15%, T. Sakanoi, private communication), combined with uncertainty in the emission brightnesses produced by the ionospheric model. The good agreement between fits with 427.8 nm data and 670.0 nm data suggests a factor independent of the MAC measurements is responsible for producing fit gradients larger than 2. This is most likely an underestimation of electron fluxes in the higher energy bins of the ESA detector, particularly above 500 eV, due to difficulties in determining the quantum efficiency of the ESA detector (K. Asamura, private communication). In this technique the uncertainty in the quantum efficiency of ESA will be preserved in the uncertainty in total electron flux estimated from the calibrated MAC data. It is possible emission brightnesses produced by the ionospheric model have also been significantly underestimated, but since the model has been independently validated with other instruments including ASK (e.g. *Ashrafi et al.*, 2009; *Lanchester et al.*, 2009) this seems less likely to be a significant factor. One of the main sources of error in the model is the neutral concentration profiles taken from the MSISE-90 model. However, this mainly affects emissions which are significantly dependent on the atomic oxygen concentration, rather than on the concentration of molecular nitrogen, as the oxygen concentration is more variable than the molecular nitrogen concentration (e.g. *Christensen et al.*, 1997). Based on an estimated fresh snow albedo of 0.9 the results suggest the total electron flux produced by the technique is underestimated by up to 35%. This underestimation will in part be due to a small number of high-energy electrons being present at times when it is assumed ESA is measuring the complete electron spectrum (i.e. coloured points in figures 7.5-7.9).

The measured electron spectra used as input to the ion-chemistry model cover pitch angles between 0° and 60°. This range is much larger than the size of the loss cone, and so ESA may measure some electron flux which does not precipitate down to auroral altitudes. However, the approximation that the entire measured electron spectrum is field-aligned acts to reduce the gradients of the fits, and therefore the results suggest there is little electron flux measured at pitch angles

outside the loss cone. Also, electrons with large pitch angles are likely to be reflected at altitudes above the low orbit of Reimei.

The variation in abscissa offset of the fits closely matches changes in lunar phase. Event 1 has a low offset of 0.26 kR, and occurred one day before a new moon. During this event the moon was on the opposite side of the planet to Reimei. Event 2 occurred one day before the following last quarter moon, and subsequently the moon contributed lots of light to the MAC background, raising the abscissa offset of the fit to 9.30 kR. The last 3 events took place in the space of 4 days close to the end of the lunar cycle. The abscissa offset decreased over these three events as the lunar illumination decreased and the moon moved further from the Reimei observation location. Event 5 has a negative abscissa offset of -1.74 kR, which could be caused by several things. The ESA spectra for event 5 shows a fairly high background flux of electrons over almost the entire energy range of the detector, which may be anomalous, leading to over-estimated model emission brightnesses. It is also possible the negative fit offset is a result of an over-estimate of the "dark current" present in the MAC measurements.

Although the application of the technique has been successfully demonstrated on several very different events, it is not possible to analyse all MAC and ESA data in this way. The satellite must be flying in Mode-S so that the ESA and MAC measurements are spatially coincident and MAC observes a height-integrated auroral brightness on a single field line. As Reimei orbits the Earth the satellite footprint moves across the MAC field of view. While *Frey et al.* (2010) applied an early version of the technique presented in this paper to observations in which the satellite footprint was outside of the MAC field of view, this led to timing discrepancies. The technique is better applied to events in which the footprint is constantly contained within the MAC field of view. In addition to this constraint, for a successful application of the technique at least part of the aurora must have no electrons at energies above the cut-off of the ESA detector.

While less accurate than the analysis shown in this work, it is possible to apply a simplified variant of the technique to obtain similar results without the use of an ionospheric model. In this case the "modelled brightness" can be estimated by multiplying the total flux measured by ESA by an estimate of the excitation efficiency, β. For the 427.8 nm emission *Steele and McEwen* (1990) measured an excitation efficiency of 290 $\pm$ 80 $\mathrm{Rm}^2/\mathrm{mW}$. Values obtained using the ionospheric model for the five events in this work are comparable to this, with a mean of 265 $\mathrm{Rm}^2/\mathrm{mW}$. The excitation efficiency for the 670.0 nm emission

is more complicated as most instruments will not observe the same vibrational transitions within the wide N_2 1PG band, so it will usually be specific to the observing instrument. For the Reimei observations the mean value of β obtained using the ionospheric model for the five events studied here is 612 $\mathrm{Rm}^2/\mathrm{mW}$ (see table 7.2). This value of β applies to only the N_2 1PG emission, and therefore the calibrated MAC data produced by using the simplified technique with this value will be a measure of the N_2 1PG brightness only, with contamination removed. This is consistent with the complete technique using the full ionospheric model.

7.5 Summary

A powerful technique for intercalibrating optical and particle measurements made by instruments on board the Reimei satellite has been described and validated with several examples. The technique demonstrates that additional information can be gained by closely combining data from the two instruments, allowing improved analyses of auroral events to be performed. It removes many sources of background and contaminating emission from the MAC optical measurements, allowing estimates of the total precipitating electron flux from the calibrated data, as well as estimates of the high-energy electron flux above the cut-off energy of the ESA detector. A simplified version of the technique can be performed without the use of an ionospheric model by using estimates of the emission excitation efficiencies obtained in this work.

The technique has many possible applications. One example is in the study of pulsating aurora, which is often caused by electrons at energies above that measured by the ESA detector. By applying this technique it would be possible to estimate the electron flux responsible for the pulsating aurora even though the flux is not directly measured by ESA. Another possible application is in the calibration of MAC observations containing black aurora, leading to comparisons between measured electron fluxes and optical emissions within and outside the black regions. In this case care must be taken to exclude "black" data from the fitting process performed as part of the technique.

Chapter 8

Conclusions

The results from analysis presented in chapters 5 and 6 support the theory that flickering aurora is caused by EMIC waves and that the wave parallel phase velocity is the primary factor limiting electron acceleration, with small-scale flickering structure generated by interference between multiple EMIC waves. This is important information for the understanding of electron acceleration in the ionosphere and magnetosphere in general, as a significant fraction of primary auroral electrons are thought to be accelerated by Alfvén waves, inputting a significant amount of energy to the ionosphere. Understanding the role of wave-particle interactions in the natural ionospheric plasma will lead to improved understanding of similar processes in other natural plasmas both within and outside the Solar System, as well as in man-made plasma.

Chapter 6 presented the first reported detailed analysis of simultaneous multi-spectral optical observations of flickering aurora, and also the first reported analysis of flickering auroral chirps, while chapter 5 presented observations of very small structures in flickering aurora. These observations were made possible by the high-resolution (in time and space), simultaneous multi-spectral capabilities of the state-of-the-art ASK instrument. As more multi-spectral optical instruments with highly-sensitive EMCCD detectors are being deployed around the polar regions similar observations are likely to be made and reported in the near future. It is important to study flickering aurora and FABs using a wide variety of different types of observations, both ground-based and space-based. Optical instruments provide the most obvious type of ground-based observation, although ISR can also provide useful information (*Grydeland et al.*, 2008). Wave and particle measurements are the most common types of space-based observation,

although the Reimei satellite has shown that high-quality optical observations of the aurora can also be made from space. Unfortunately the time resolution of the MAC instrument onboard Reimei is not sufficient for the study of flickering aurora.

Chapter 7 presented a novel technique for intercalibrating simultaneous optical and particle measurements made by instruments on board the Reimei satellite using the Southampton Ionospheric Model. The technique will be of benefit to many auroral studies using Reimei data, both in the calibration of the MAC instrument and in the estimation of high-energy electron fluxes.

The work presented in this thesis highlights the considerable benefit of combining observations with detailed ionospheric modelling. The Southampton Ionospheric Model has been used in two distinct ways in this work: for modelling the dependence of auroral emission brightnesses on electron precipitation energy (mainly chapter 6) and for modelling specific auroral events (chapter 7). Both uses allow additional information to be obtained from observations, allowing conclusions to be made which would not be possible without the use of the model.

8.1 Future work

This section gives some suggestions for the continuation of the studies presented in this thesis.

There are many ways to continue the study of flickering aurora with ASK. Although new or undiscovered observations of flickering aurora in ASK data will undoubtedly assist in this research, there is much useful analysis which is yet to be performed on the data used here. Some ideas include:

1. Variations in the energy spectra of flickering aurora spatially across the ASK camera images should be investigated, in a combined spatial and spectral study. This will assist in further, more detailed interpretation of the spatial patterns seen in the ASK1 camera. If flickering aurora is analysed on the edge of the ASK camera field of view (away from the magnetic zenith) perspective effects must be considered when estimating electron precipitation energies. Emissions observed with the ASK1 camera usually come from lower altitudes than the 777.4 nm emission observed with ASK3, so the same pixel in both cameras does not correspond to the same magnetic field line. B. Gustavsson is currently developing a tool to “de-perspective”

ASK images and produce accurate energy-flux maps of the aurora using the Southampton Ionospheric Model.

2. An investigation into the phase difference between simultaneous flickering patches and phase variations across spatial structures in flickering aurora could lead to a better understanding of the mechanism producing the observed structure. Observations could be compared with results from a model of interfering waves similar to those used by *Sakanoi et al.* (2005) and *Gustavsson et al.* (2008).

3. So far only a small region of the ASK images (corresponding to the photometer field of view) has been searched for flickering chirps. However, since flickering structures can be seen right across the camera field of view (see figures 5.8–5.11) there may be chirps in regions of the image not yet examined for chirps. As for point 1 of this list, perspective effects must be considered when estimating electron precipitation energies in chirps away from the magnetic zenith.

4. A spatial analysis of the flickering aurora observed on 12 December 2006 has not yet been carried out, as this event had not been discovered when the spatial analysis presented in chapter 5 was carried out. It would be worth checking that the temporal correlation and lack of spatial correlation between flickering and non-flickering aurora found on 22 October 2006 also hold for the December event.

5. *Peticolas and Lummerzheim* (2000) used a time-dependent auroral electron transport model to simulate field-aligned bursts with an on-off electron intensity distribution. Similar work could be carried out using a modified version of the Southampton Ionospheric Model, for comparison with ASK results. Alternatively a model of EMIC wave propagation and electron acceleration in the auroral acceleration region, similar to that used by *Chen et al.* (2005), could be be developed to provide electron spectra as input to the Southampton Ionospheric Model. Comparison could then be made with ASK observations.

6. Using the ASK observations of the O^+ ^2P – ^2D transition at 732.0 nm (filter 4 in table 3.1) in combination with the other simultaneous ASK measurements it should be possible to obtain estimates of the O/N_2 concentration

ratio. This could then be used to correct MSISE-90 when modelling specific events with the Southampton Ion Chemistry Model, leading to improved estimates of the precipitating electron energy distribution.

Although scientific discoveries cannot be accurately predicted, some examples of work which could be done with further observations of flickering aurora include:

7. Although all ASK data presented in this thesis were acquired while the instrument was located close to Tromsø, ASK has mainly been located on Svalbard, where it is possible to observe dayside aurora. There may have been ASK observations of flickering events within dayside aurora, which could be compared with the nightside events studied in this work. Recently a potential flickering event was identified in observations made soon after 12 UT (∼9 MLT) on 11 January 2010 which could be suitable for this study. *Gustavsson et al.* (2008) presented observations of flickering in nightside aurora above Svalbard.

8. Finding more chirps in both ASK data and data from other instruments would help to confirm the conclusions drawn in chapter 6, and could assist in explaining the mechanisms producing the chirps.

9. It may be possible to identify flickering aurora at frequencies higher than 16 Hz in ASK photometer data, since the photometers run at much higher frequencies than the ASK cameras. There are very few observations of flickering aurora above the Nyquist frequency of typical video frame rates. *McHarg et al.* (1998) observed flickering aurora in the 20–60 Hz range, which could be attributed to He^+ EMIC waves, as opposed to "standard" flickering aurora from O^+ EMIC waves. They also observed broadband flickering across a large frequency range up to about 50 Hz, which they suggest could be a result of inhomogeneous energy density driven (IEDD) waves. However, very little is understood about this type of flickering aurora.

10. Since the ASK photometers were absolute intensity calibrated in late 2010, it should be possible to obtain better estimates of the precipitating electron energy spectrum by combining information from the cameras and photometers. The 470.9 nm emission measured by photometer 1 is relatively simple and can already be modelled by the Southampton Ionospheric Model. To model the 844.6 nm emission will require more work, as it is fed by cascading from a higher energy level, with a dependence on the optical thickness of

the medium (e.g. *Julienne and Davis*, 1976). A process to infer the electron energy spectrum from the brightnesses of multiple auroral emissions could be applied to the study of many auroral features besides flickering aurora.

11. A survey of FABs observed by space-based instruments (rockets and satellites) and flickering aurora observed using ground-based optical instruments should be made. If FABs are typically observed at higher frequencies than optical flickering aurora it would suggest that the EMIC waves producing the observed FABs are initiated at lower altitudes than those producing optical flickering aurora, as the ion cyclotron frequency is higher at lower altitudes. This would support the argument that FAB are more likely to be observed at energies below the inverted-V peak energy whereas optical flickering aurora is more likely to be observed at higher energies, when electrons are accelerated by the wave and then by the potential drop.

12. Modern satellite and rocket-based measurements of the electron energy spectrum at high energies above the inverted-V peak energy could confirm that flickering aurora and FABs are not limited to low energies, as is concluded in this thesis. Unfortunately designing and funding a rocket specifically for shooting into flickering aurora is impractical, as the chance of encountering flickering aurora at the correct location during a typical launch window of about 2 weeks is small. The chance of predicting flickering aurora far enough in advance to ensure the rocket flies through it is even smaller. Therefore satellite-based instruments may be more suited to this task.

The technique described in chapter 7 has many possible applications in auroral studies using Reimei observations. Some ideas include:

13. The study of pulsating aurora, which is often high energy (*Nishimura et al.*, 2010), above the detection limit of ESA. Using the technique the total electron flux producing the pulsating aurora could be determined.

14. A possible application of the technique is in the calibration of MAC observations containing black aurora (e.g. *Trondsen and Cogger*, 1997), leading to comparisons between measured electron fluxes and optical emissions within and outside the black regions. In this case care must be taken to exclude "black" data from the fitting process performed as part of the technique.

15. An evaluation of theories for the structure and formation of auroral arcs would benefit from accurate estimates of the total flux within an auroral arc, along with the flux and energy profile across the arc. The technique would help provide the flux measurements required.

Bibliography

Arnoldy, R. L., Rapid fluctuations of energetic auroral particles, *J. Geophys. Res.*, *75*(1), 228–232, 1970.

Arnoldy, R. L., K. A. Lynch, J. B. Austin, and P. M. Kintner, Energy and pitch angle-dispersed auroral electrons suggesting a time-variable, inverted-v potential structure, *J. Geophys. Res.*, *104*(A10), 22613–22621, doi: 10.1029/1999JA900219, 1999.

Asamura, K., D. Tsujita, H. Tanaka, Y. Saito, T. Mukai, and M. Hirahara, Auroral particle instrument onboard the INDEX satellite, *Adv. Space. Res.*, *32*(3), 375–378, doi:10.1016/S0273-1177(03)00275-8, 2003.

Ashrafi, M., B. S. Lanchester, D. Lummerzheim, N. Ivchenko, and O. Jokiaho, Modelling of N_2-1P emission rates in aurora using different cross sections for excitation, *Ann. Geophys.*, *27*, 2545–2553, 2009.

Bellan, P. M., and K. Stasiewicz, Fine-scale cavitation of ionospheric plasma caused by inertial Alfvén wave ponderomotive force, *Phys. Rev. Lett.*, *80*(16), 3523–3526, 1998.

Chaston, C. C., L. M. Peticolas, J. W. Bonnell, C. W. Carlson, R. E. Ergun, J. P. McFadden, and R. J. Strangeway, Width and brightness of auroral arcs driven by inertial Alfvén waves, *J. Geophys. Res.*, *108*(A2), 1091, doi: 10.1029/2001JA007537, 2003.

Chaston, C. C., C. W. Carlson, J. P. McFadden, R. E. Ergun, and R. J. Strangeway, How important are dispersive Alfvén waves for auroral particle acceleration?, *Geophys. Res. Lett.*, *34*, L07101, doi:10.1029/2006GL029144, 2007.

Chen, L.-J., C. A. Kletzing, S. Hu, and S. R. Bounds, Auroral electron dispersion

below inverted-v energies: Resonant deceleration and acceleration by Alfvén waves, *J. Geophys. Res.*, *110*, A10S13, doi:10.1029/2005JA011168, 2005.

Christensen, A. B., J. H. Hecht, R. L. Walterscheid, M. F. Larsen, and W. E. Sharp, Depletion of oxygen in aurora: Evidence for a local mechanism, *J. Geophys. Res.*, *102*(A10), 22273–22277, doi:10.1029/97JA01800, 1997.

Dahlgren, H., N. Ivchenko, J. Sullivan, B. S. Lanchester, G. Marklund, and D. Whiter, Morphology and dynamics of aurora at fine scale: first results from the ASK instrument, *Ann. Geophys.*, *26*, 1041–1048, 2008.

Dahlgren, H., N. Ivchenko, B. Lanchester, M. Ashrafi, D. Whiter, G. Marklund, and J. Sullivan, First direct optical observations of plasma flows using afterglow of O^+ in discrete aurora, *J. Atmos. Sol. Terr. Phys.*, *71*(2), 228–238, doi: 10.1016/j.jastp.2008.11.015, 2009.

Dahlgren, H., A. Aikio, K. Kaila, N. Ivchenko, B. Lanchester, D. Whiter, and G. Marklund, Simultaneous observations of small multi-scale structures in an auroral arc, *J. Atmos. Sol. Terr. Phys.*, *72*, 633–637, doi: 10.1016/j.jastp.2010.01.014, 2010.

Erlandson, R. E., and L. J. Zanetti, A statistical study of auroral electromagnetic ion cyclotron waves, *J. Geophys. Res.*, *103*(A3), 4627–4636, 1998.

Evans, D. S., A 10-cps periodicity in the precipitation of auroral-zone electrons, *J. Geophys. Res.*, *72*, 4281–4291, 1967.

Farley, T. D., Multiple-pulse incoherent-scatter correlation function measurements, *Radio Sci.*, *7*, 661–666, 1972.

Frey, H., O. Amm, C. Chaston, S. Fu, G. Haerendel, L. Juusola, T. Karlsson, B. Lanchester, R. Nakamura, N. Østgaard, T. Sakanoi, E. S'eran, D. Whiter, J. Weygand, K. Asamura, and M. Hirahara, Small and meso-scale properties of a substorm onset auroral arc, *J. Geophys. Res.*, *115*, A10209, doi: 10.1029/2010JA015537, 2010.

Gattinger, R. L., and A. Vallance Jones, Quantitative spectroscopy of the aurora. II. the spectrum of medium intensity aurora between 4500 and 8900 å, *Can. J. Phys.*, *52*, 2343–2356, 1974.

Grydeland, T., B. Gustavsson, L. Baddeley, J. Lunde, and E. M. Blixt, Conditional integration of incoherent scattering in relation to flickering aurora, *J. Geophys. Res.*, *113*, A08305, doi:10.1029/2008JA013039, 2008.

Gustavsson, B., J. Lunde, and E. M. Blixt, Optical observations of flickering aurora and its spatiotemporal characteristics, *J. Geophys. Res.*, *113*, A12317, doi:10.1029/2008JA013515, 2008.

Hedin, A. E., Extension of the MSIS thermosphere model into the middle and lower atmosphere, *J. Geophys. Res.*, *96*(A2), 1159–1172, doi: 10.1029/90JA02125, 1991.

Holmes, G. J., D. J. Knudsen, and T. S. Trondsen, Highly coherent and localized sub-structures within auroral flicker, *Canadian Undergraduate Physics Journal*, *4*(1), 7–12, 2005a.

Holmes, G. J., T. S. Trondsen, D. J. Knudsen, L. L. Cogger, N. Partamies, M. Syrjäsuo, and L. Sangalli, Fine structure within auroral flicker, presented as a poster at AGU Fall Meeting, San Francisco, Calif., 5–9 December, abstract SM51B-1304, 2005b.

Höök, J., Multispectral auroral imager and optical flow in aurora, MSc, Royal Institute of Technology (KTH), Stockholm, Sweden, 2006.

Itikawa, Y., Cross sections for electron collisions with nitrogen molecules, *J. Phys. Chem. Ref. Data*, *35*, 31–53, 2005.

Julienne, P. S., and J. Davis, Cascade and radiation trapping effects on atmospheric atomic oxygen emission excited by electron impact, *J. Geophys. Res.*, *81*(7), 1397–1403, 1976.

Kaila, K. U., Determination of the energy of auroral electrons by the measurements of the emission ratio and altitude of aurorae, *Planet. Space Sci.*, *37*(3), 341–349, 1989.

Kivelson, M. G., and C. T. Russell (Eds.), *Introduction to Space Physics*, Cambridge University Press, Cambridge, United Kingdom, 1995.

Kunitake, M., and T. Oguti, Spatial-temporal characteristics of flickering spots in flickering auroras, *J. Geomag. Geoelectr.*, *36*, 121–138, 1984.

Lanchester, B. S., M. H. Rees, D. Lummerzheim, A. Otto, K. J. F. Sedgemore-Schulthess, H. Zhu, and I. W. McCrea, Ohmic heating as evidence for strong field-aligned currents in filamentary aurora, *J. Geophys. Res.*, *106*(A2), 1785–1794, 2001.

Lanchester, B. S., M. Ashrafi, and N. Ivchenko, Simultaneous imaging of aurora on small scale in OI (777.4 nm) and $N_2$1P to estimate energy and flux of precipitation, *Ann. Geophys.*, *27*, 2881–2891, 2009.

Lehtinen, M. S., and I. Häggström, A new modulation principle for incoherent scatter measurements, *Radio Sci.*, *22*, 625–634, 1987.

Lehtinen, M. S., J. Markkanen, A. Väänänen, A. Huuskonen, B. Damtie, T. Nygrén, and J. Rakola, A new incoherent scatter technique in the EISCAT Svalbard Radar, *Radio Sci.*, *37*(4), 1050, doi:10.1029/2001RS002518, 2002.

Lummerzheim, D., and J. Lilensten, Electron transport and energy degradation in the ionosphere: evaluation of the numerical solution comparison with laboratory experiments and auroral observations, *Ann. Geophys.*, *12*, 1039–1051, 1994.

Lund, E. J., J. LaBelle, R. B. Torbert, K. Liou, W. Peria, C. A. Kletzing, M. C. Kelley, S. D. Baker, F. Primdahl, H. C. Stenbaek-Nielsen, A. Ranta, G. Haerendel, and H. U. Frey, Observation of electromagnetic oxygen cyclotron waves in a flickering aurora, *Geophys. Res. Lett.*, *22*(18), 2465–2468, doi:10.1029/95GL02409, 1995.

McFadden, J. P., C. W. Carlson, M. H. Boehm, and T. J. Hallinan, Field-aligned electron flux oscillations that produce flickering aurora, *J. Geophys. Res.*, *92*, 11133–11148, 1987.

McFadden, J. P., C. W. Carlson, and M. H. Boehm, Structure of an energetic narrow discrete arc, *J. Geophys. Res.*, *95*(A5), 6533–6547, 1990.

McFadden, J. P., C. W. Carlson, R. E. Ergun, C. C. Chaston, F. S. Mozer, M. Temerin, D. M. Klumpar, E. G. Shelley, W. K. Peterson, E. Moebius, L. Kistler, R. Elphic, R. Strangeway, C. Cattell, and R. Pfaff, Electron modulation and ion cyclotron waves observed by FAST, *Geophys. Res. Lett.*, *25*(12), 2045–2048, doi:10.1029/98GL00855, 1998.

McHarg, M. G., D. L. Hampton, and H. C. Stenbaek-Nielsen, Fast photometry of flickering in discrete auroral arcs, *Geophys. Res. Lett.*, *25*(14), 2637–2640, doi:10.1029/98GL01972, 1998.

Nishimura, Y., J. Bortnik, W. Li, R. M. Thorne, L. R. Lyons, V. Angelopoulos, S. B. Mende, J. W. Bonnell, O. L. Contel, C. Cully, R. Ergun, and U. Auster, Identifying the driver of pulsating aurora, *Science*, *330*(6000), 2010.

Obuchi, Y., T. Sakanoi, A. Yamazaki, T. Ino, S. Okano, Y. Kasaba, M. Hirahara, Y. Kanai, and N. Takeyama, Initial observations of auroras by the multi-spectral auroral camera on board the Reimei satellite, *Earth, Planets & Space*, *60*, 827–835, 2008.

Partamies, N., M. Syrjäsuo, E. Donovan, M. Connors, D. Charrois, D. Knudsen, and Z. Kryzanowsky, Observations of the auroral width spectrum at kilometre-scale size, *Ann. Geophys.*, *28*(3), 711–718, doi:10.5194/angeo-28-711-2010, 2010.

Paschmann, G., S. Haaland, and R. Treumann (Eds.), *Auroral Plasma Physics*, *Space Sciences Series of ISSI*, vol. 15, Kluwer Academic Publishers, Dordrecht, The Netherlands, 2003.

Peticolas, L., and D. Lummerzheim, Time-dependent transport of field-aligned bursts of electrons in flickering aurora, *J. Geophys. Res.*, *105*(A6), 12895–12906, doi:10.1029/1999JA000398, 2000.

Rees, M. H., *Physics and chemistry of the upper atmosphere*, Cambridge University Press, Cambridge, United Kingdom, 1989.

Saito, H., Y. Masumoto, T. Mizuno, A. Miura, M. Hashimoto, H. Ogawa, S. Tachikawa, T. Oshima, A. Choki, H. Fukuda, M. Hirahara, and S. Okano, INDEX: piggy-back satellite for aurora observation and technology demonstration, *Acta Astronautica*, *48*, 723–735, 2001.

Sakanoi, K., and H. Fukunishi, Temporal and spatial structures of flickering aurora derived from high-speed imaging photometer observations at Syowa station in the Antarctic, *J. Geophys. Res.*, *109*, A01221, doi:10.1029/2003JA010081, 2004.

Sakanoi, K., H. Fukunishi, and Y. Kasahara, A possible generation mechanism of temporal and spatial structures of flickering aurora, *J. Geophys. Res.*, *110*, A03206, doi:10.1029/2004JA010549, 2005.

Sakanoi, T., S. Okana, Y. Obuchi, T. Kobayashi, M. Ejiri, K. Asamura, and M. Hirahara, Development of the Multi-spectral Auroral Camera onboard the INDEX satellite, *Adv. Space. Res.*, *32*(3), doi:10.1016/S0273-1177(03)00273-4, 2003.

Sandahl, I., T. Sergienko, and U. Brändström, Fine structure of optical aurora, *J. Atmos. Sol. Terr. Phys.*, *70*(18), 2275–2292, doi:10.1016/j.jastp.2008.08.016, 2008.

Solomon, S. C., P. B. Hays, and V. J. Abreu, The auroral 6300 å emission: Observations and modeling, *J. Geophys. Res*, *93*(A9), 9867–9882, 1988.

Spiger, R. J., and H. R. Anderson, Fluctuations of precipitated electron intensity in flickering auroral arcs, *J. Geophys. Res.*, *90*, 6647–6651, 1985.

Stasiewicz, K., P. Bellan, C. Chaston, C. Kletzing, R. Lysak, J. Maggs, O. Pokhotelov, C. Seyler, P. Shukla, L. Stenflo, A. Streltsov, and J.-E. Wahlund, Small scale alfvénic structure in the aurora, *Space Sci. Rev.*, *92*, 423–533, 2000.

Steele, D. P., and D. J. McEwen, Electron auroral excitation efficiencies and intensity ratios, *J. Geophys. Res.*, *95*, 10321–10336, doi:10.1029/JA095iA07p10321, 1990.

Sulzer, M. P., A radar technique for high range resolution incoherent scatter autocorrelation function measurements utilizing the full average power of klystron radars, *Radio Sci.*, *21*, 1035–1040, 1986.

Temerin, M., J. McFadden, M. Boehm, C. W. Carlson, and W. Lotko, Production of flickering aurora and field-aligned electron flux by electromagnetic ion cyclotron waves, *J. Geophys. Res.*, *91*, 5769–5792, 1986.

Trondsen, T. S., and L. L. Cogger, High-resolution television observations of black aurora, *J. Geophys. Res.*, *102*(A1), 363–378, 1997.

Turunen, T., J. Silén, T. Nygrén, and L. Jalonen, Observations of a thin Es-layer by the EISCAT radar, *Planet. Space Sci.*, *33*, 1407–1416, 1985.

Whiter, D. K., B. S. Lanchester, B. Gustavsson, N. Ivchenko, J. M. Sullivan, and H. Dahlgren, Small-scale structures in flickering aurora, *Geophys. Res. Lett.*, *35*, L23103, doi:10.1029/2008GL036134, 2008.

Whiter, D. K., B. S. Lanchester, B. Gustavsson, N. Ivchenko, and H. Dahlgren, Using multispectral optical observations to identify the acceleration mechanism responsible for flickering aurora, *J. Geophys. Res.*, *115*, A12315, doi: 10.1029/2010JA015805, 2010.